A FLOOD RISK ASSESSMENT BASED ON DAM-BREAK FAILURE: CASE STUDY ON ONDOKUZ MAYIS DAM

A THESIS SUBMITTED TO
THE GRADUATE SCHOOL OF NATURAL AND APPLIED SCIENCES
OF
MIDDLE EAST TECHNICAL UNIVERSITY

BY

NAZLI PALAMUT KEMALOĞLU

IN PARTIAL FULFILLMENT OF THE REQUIREMENTS
FOR
THE DEGREE OF DOCTOR OF PHILOSOPHY
IN
CIVIL ENGINEERING

JANUARY 2025

Approval of the thesis:

A FLOOD RISK ASSESSMENT BASED ON DAM-BREAK FAILURE: CASE STUDY ON ONDOKUZ MAYIS DAM

submitted by **NAZLI PALAMUT KEMALOĞLU** in partial fulfillment of the requirements for the degree of **Doctor of Philosophy** i**n Civil Engineering, Middle East Technical University** by,

Prof. Dr. Naci Emre Altun
Dean, **Graduate School of Natural and Applied Sciences** _____

Prof. Dr. Erdem Canbay
Head of the Department, **Civil Engineering** _____

Prof. Dr. Zafer Bozkuş
Supervisor, **Civil Engineering, METU** _____

Examining Committee Members:

Prof. Dr. A. Melih Yanmaz
Civil Engineering, METU _____

Prof. Dr. Zafer Bozkuş
Civil Engineering, METU _____

Prof. Dr. A. Burcu Altan Sakarya
Civil Engineering, METU _____

Prof. Dr. Yakup Darama
Civil Engineering, Atılım University _____

Prof. Dr. Kerem Taştan
Civil Engineering, Gazi University _____

Date: 10.01.2025

I hereby declare that all information in this document has been obtained and presented in accordance with academic rules and ethical conduct. I also declare that, as required by these rules and conduct, I have fully cited and referenced all material and results that are not original to this work.

Name Last name : Nazlı Palamut Kemaloğlu

Signature :

ABSTRACT

A FLOOD RISK ASSESSMENT BASED ON DAM-BREAK FAILURE: CASE STUDY ON ONDOKUZ MAYIS DAM

Palamut Kemaloğlu, Nazlı
Master of Science, Civil Engineering
Supervisor : Prof. Dr. Zafer Bozkuş

January 2025, 167 pages

This study focuses on the flood risk assessment of a hypothetical two-dimensional failure of the Ondokuz Mayıs Dam, a clay core rockfill dam type located in Samsun, Turkey, with a height of 89.75 meters. The main objective is to evaluate flood risks under different dam failure scenarios and estimate the economic damages. The study compares the effects of model mesh sizes, breach parameter prediction equations, and hydraulic solution methods, including shallow water and diffusion wave approaches, on flood analysis results. To improve the accuracy and reliability of the analysis, all structures within the floodplain were modeled in 3D and integrated into the DEM model. The breach hydrographs were routed over the floodplain using HEC-RAS, and the results were visualized using ArcGIS software. Missing precipitation and flow data after 2010 were obtained from the DSI and used to recalculate dam operation studies and project flood discharges. The adequacy of the current spillway capacity was checked, dam slope safety factors under different loading conditions were determined, and the dam's safety against uplift effects, backward erosion piping risks, and seepage risks from the dam body and foundation were also evaluated. To assess the performance of the current design, the downstream slope's horizontal unit was incrementally increased from 2.0H:1.0V to

2.6H:1.0V at 0.1 intervals. Monte Carlo simulations (using Slide2 software) were used to calculate the probabilities of dam failure for each slope, and the long-term economic benefits and cost-benefit ratios of the modified slopes were analyzed to strengthen the design. Finally, flood damage maps for buildings, roads, and agricultural areas were created for the worst-case failure scenarios. Economic losses were similar in both scenarios, with the majority of losses involving buildings and infrastructure (roads).

Keywords: Dam breach, Two-dimensional flood modeling, HEC-RAS, Flood risk assessment, Monte-Carlo simulation

ÖZ

BARAJ YIKILMASI KAYNAKLI BİR TAŞKIN RİSKİ DEĞERLENDİRMESİ: ONDOKUZ MAYIS BARAJI ÖRNEĞİ

Palamut Kemaloğlu, Nazlı
Doktora, İnşaat Mühendisliği
Tez Yöneticisi: Prof. Dr. Zafer Bozkuş

Ocak 2025, 167 sayfa

Bu çalışma, Türkiye'nin Samsun ilinde bulunan, 89.75 metre yüksekliğinde bir kil çekirdekli kaya dolgu baraj tipindeki Ondokuz Mayıs Barajı'nın varsayımsal iki boyutlu yıkılma durumunun taşkın risk değerlendirmesine odaklanmaktadır. Ana hedef, farklı baraj yıkılma senaryolarında taşkın risklerini değerlendirmek ve ekonomik zararları tahmin etmektir. Çalışmada, model ağ yapıları, yıkılma parametresi tahmin denklemleri ve taşkın analiz sonuçları üzerinde etkili olan hidrolik çözüm yöntemlerinin (sığ su ve yayılmalı dalga yöntemleri dahil) karşılaştırılması yapılmıştır. Analizin doğruluğunu ve güvenilirliğini artırmak amacıyla, taşkın alanındaki tüm yapılar üç boyutlu olarak modellenmiş ve DEM modeline entegre edilmiştir. Gedik hidrografları, HEC-RAS kullanılarak taşkın alanında ötelenmiş ve sonuçlar ArcGIS yazılımı ile görselleştirilmiştir. 2010 yılı sonrası eksik olan yağış ve debi verileri DSİ'den temin edilerek baraj işletme çalışması ve proje taşkın debileri yeniden hesaplanmıştır. Mevcut dolusavak kapasitesinin yeterliliği kontrol edilmiş, farklı yükleme koşulları altında baraj şev güvenlik faktörleri bulunmuş, barajın kaldırma etkisine karşı güvenliği, geriye doğru

erozyon kaynaklı borulanma riski ve baraj gövdesinden ve temelden sızma riskleri de kontrol edilmiştir. Mevcut tasarımın performansını değerlendirmek için, mansap şevinin yatay birimi 2.0Y:1.0D'den 2.6Y:1.0D'ye kadar 0.1 aralıklarla artırıldı. Her şev için baraj yıkılma olasılığını hesaplamak amacıyla Monte Carlo simülasyonları (Slide2 yazılımı kullanılarak) kullanıldı ve tasarımı güçlendirmek için değiştirilen şevlerin uzun vadeli ekonomik faydaları ve maliyet-fayda oranları analiz edildi. Son olarak en kötü yıkılma senaryolarında binalar, yollar ve tarım alanları için taşkın zarar haritaları oluşturulmuştur. Ekonomik kayıplar her iki senaryoda benzer olup, kayıpların çoğunu binalar ve altyapı (yollar) oluşturmaktadır.

Anahtar Kelimeler: Baraj yıkılması, İki boyutlu taşkın modelleme, HEC-RAS, Taşkın risk değerlendirme, Monte Carlo simülasyonu

I dedicate this thesis to my beloved family.

ACKNOWLEDGMENTS

First and foremost, I would like to express my heartfelt gratitude to my advisor, **Prof. Dr. Zafer Bozkuş**, for his invaluable guidance, continuous encouragement, and profound knowledge throughout my research and the preparation of this dissertation. His thoughtful mentorship and insightful feedback have been instrumental in overcoming challenges and shaping this study. Despite his busy schedule, his unwavering support and accessibility have inspired me greatly and made this journey more meaningful.

I am especially indebted to **Prof. Dr. Melih Yanmaz**, whose contributions were pivotal in shaping the direction and structure of this thesis. His detailed guidance and suggestions ensured its quality and depth at each research stage. His dedicated time and effort in reviewing my work and providing constructive feedback were invaluable.

I would also like to extend my sincere gratitude to **Prof. Dr. Yakup Darama**, whose expertise, constructive criticism, and support have enriched the scope and depth of this research. His thoughtful insights were crucial in enhancing the quality of this dissertation.

I am also deeply thankful to **Prof. Dr. Kemal Önder Çetin** for the valuable time he dedicated to me during my visit and his insightful advice. His extensive knowledge and experience have enriched my research and elevated it to a higher level.

I am profoundly grateful to my dear husband, **Zülfikar Erkay Kemaloğlu**, for his technical support, unwavering emotional encouragement and for creating a peaceful and supportive home environment throughout this journey. His understanding and patience have been a source of great strength. My heartfelt thanks also go to my son, **Mustafa Aras Kemaloğlu**, for his patience and understanding as I worked through this process.

Lastly, I would like to express my deep gratitude to my mother, **Engin Palamut**, for her endless love, unwavering belief in me, and constant support throughout my life. Her encouragement has been a driving force behind my accomplishments.

I would also like to thank the academic and administrative staff of the Civil Engineering Department at METU for providing a nurturing and inspiring environment that made this journey memorable.

TABLE OF CONTENTS

LIST OF TABLES

LIST OF FIGURES

LIST OF ABBREVIATIONS

AFAD	Disaster and Emergency Management Authority
AHP	Analytic Hierarchy Process
ArcGIS	Aeronautical Reconnaissance Coverage Geographic Information System
ArcScene	ArcGIS 3D Visualization Tool
ASDSO	Association of State Dam Safety Officials
CORINE	Coordination of Information on the Environment
CSB	Turkey's Ministry of Environment, Urbanization and Climate Change
COE	Corps of Engineers
DFIC	Dam Failure and Incidents Committee
DEM	Digital Elevation Model
DEMs	Digital Elevation Models
DWE	Diffusion Wave Equation
DTM	Digital Terrain Model
FEMA	Federal Emergency Management Agency, US
FLO-2D	Flood Simulation Model-Two-Dimensional Model
GIS	Geographic Information System
HAZUS-MH	Hazards U.S. Multi-Hazard
HEC-HMS	Hydrologic Engineering Center – Hydrologic Modeling System
HEC-RAS 1D	HEC-RAS One-Dimensional Model
HEC-RAS 2D	HEC-RAS Two-Dimensional Model
ICOLD	International Commission on Large Dams
IDW	Inverse Distance Weighting

JRC	Joint Research Center
LEM	Limit Equilibrium Method
MCS	Monte Carlo Simulation
NWS	National Weather Service
PMF	Probable Maximum Flood
PGA	The Peak Ground Acceleration
RMSE	Root Mean Square Error
SEEP/W	Seepage Analysis in Two-Dimensional Saturated-Unsaturated Flow
SRF	Strength Reduction Factor
STD	Standard Deviation
TURKSTAT	Turkish Statistical Institute
TRCOLD	Turkish National Committee on Large Dams
DSI	State Hydraulic Works, Turkey
UCS	Unconfined Compressive Strength
USACE	United States Army Corps of Engineers, US
US	United States
1D	One Dimensional
2D	Two Dimensional
3D	Three Dimensional
TRY	Turkish Lira

LIST OF SYMBOLS

A	Area of the building	m^2
W	Average breach width	m
BF	Structure unit price	TRY
C	Courant number	-
C_b	Coefficient dependent on reservoir size	-
c_f	Bottom friction coefficient	-
D	A non-dimensional empirical constant that depends upon the geometry and bottom/wall surface	-
FS	The safety factor	-
f	Coriolis parameter	
g	Gravitational acceleration value	m/s^2
H	Water surface elevation	m
H:V	Horizontal/Vertical ratio	-
H_b	Breach depth	m
HD	Height of dam	m
hh:mm:ss	Hour:minutes	hr:min:sec
h_w	Depth of water above the bottom of the breach	m
i	Hydraulic gradient	-
i_c	Critical Gradient	-
K_o	Constant number (1.3 for overtopping failures and 1.0 for piping)	-
k_x	Permeability	m/s
L	Length of the flow path	m
Max	Maximum value	-

P_f	Probability of failure	-
Q_p	Maximum discharge	m^3/s
Q_{PMF}	Discharge at probable maximum flood	m^3/s
R	Hydraulic radius	m
R^2	Coefficient of determination	-
S	The side slope of the breach	-
T_f	Full breach development time	sec
T_p	Time to reach peak discharge	sec
u	Velocity components in x direction	m/s
U	Uplifting force caused by seepage	N
V_{PMF}	Volume at probable maximum flood	m^3
V_{er}	The volume of material eroded from the dam embankment	m^3
V_o	The volume of water released	m^3
V_{out}	The volume of water that passes through the breach	m^3
V_w	Reservoir volume at the start of dam failure	m^3
v	Velocity components in y direction	m/s
W'	Submerged weight of soil	N
W	Average breach width	m
W_b	Breach bottom width	m
γ_s	Unit weight of soil particles	N/m^3
γ_w	Unit weight of water	N/m^3
Δh	Hydraulic head	m
ΔQ	Discharge difference	m^3/s

CHAPTER 1

INTRODUCTION

This chapter presents the study's background, defines the problem statement, highlights the significance of the research, and outlines its scope and objectives.

1.1 Importance of Study

Dams are critical infrastructures that provide flood control, water supply, power generation, agricultural support, and recreational benefits. However, a dam failure can result in catastrophic flooding, causing widespread property damage and losses of human lives in downstream regions. This prompts several critical inquiries: How many homes and businesses would be affected by such an event, and how many people could be displaced? Would the remaining water resources suffice for domestic use, agricultural irrigation, livestock needs, and firefighting? In areas dependent on hydropower, how would a temporary shutdown of industries reliant on this energy source impact local employment and livelihoods? Furthermore, what disruptions would occur to transportation infrastructure, such as roads, railways, and waterways? Finally, the loss of a reservoir could lead to significant economic consequences, affecting both local industries and recreational activities that depend on the water supply. A flood risk assessment study can answer some of these questions satisfactorily, helping us better understand the potential impacts of a dam failure.

1.2 Historical Dams' Failures

The International Commission on Large Dams (ICOLD) has investigated numerous dam breaches and accidents since the 1970s, and China began collecting systematic data on dam breaches in the 1980s (Li et al., 2024).

According to the International Commission on Large Dams (ICOLD) database, as of 2024, there are over 62,000 dams worldwide and thousands of kilometers of dikes constructed for flood control, irrigation, hydropower, water supply, and recreation purposes. However, maximum flow rates within the life span of dams and dikes introduced to increase due to climate change. Many dams and dikes now face the risk of overtopping during severe flooding events, which can lead to significant loss of life and economic damage. The severity of these impacts depends on factors such as water depth, velocity, warning time, and population density (Zagonjolli, 2007). Given these challenges, implementing comprehensive flood risk assessments is essential for enhancing preparedness, safeguarding communities, and minimizing potential economic losses.

In a global context, according to the database compiled by Bernard-Garcia & Mahdi (2022) from Polytechnique Montreal, 3861 cases of historical dam failures worldwide were documented, of which 105 were rockfill types. This demonstrates the worldwide scale of dam failures and the continuous need for improved prediction and prevention strategies.

According to the guidelines created by the Association of State Dam Safety Officials (ASDSO) Dam Failure and Incidents Committee (DFIC), damages from selected dam failures include the failure of the Buffalo Creek Dam (13.41 m) in West Virginia in 1972, which resulted in 131 fatalities and $19 million in damages; the failure of the Teton Dam (92.96 m) in Idaho in 1976, causing 11 deaths, $300 million in damages, and the destruction of 3,000 homes; the failure of the New Orleans levees in 2005, leading to approximately 1,200 fatalities and $20 to $28 billion in damages, with 100,000 houses damaged or destroyed; and the failure of the Kaloko Dam

(15.24 m) in Hawaii in 2006, which resulted in 7 fatalities and the destruction of several houses and roads, totaling about $9 million in damages (ASDSO, 2021), (Graham, 1999).

According to Table 1.1, prepared by ICOLD, the ratio of rockfill dam failures is 1.39%, primarily due to the high number of incidents involving rockfill dams. Below, various historical dam failure events and their associated failure times are presented, illustrating the rapid occurrence of these failures and highlighting the inherent vulnerabilities of embankment dams.

Table 1.1 Dam failures according to their type (ICOLD, 2019)

Dam type	**Existing dams**	**Failed**	**Ratio (%)**
VA - Arch	890	6	0.67
CB - Buttress	340	8	2.35
MV - Multi-Arch	105	4	3.81
PG - Gravity	5571	46	0.83
ER - Rockfill	2378	33	1.39
TE - Earthfill	21977	209	0.95
BM - Barrage	224	0	0
XX - Unknown	715	5	0.70

Figure 1.1 presents some observed failures obtained from ICOLD (2019) regarding the number of occurrences and failure modes for rockfill and earthfill dams. The bar chart illustrates the failure modes of embankment dams, comparing rockfill and earthfill types. It highlights three main failure causes: internal erosion, overtopping, and structural failure. Earthfill dams (represented by orange bars) experience significantly more failures across all categories than rockfill dams (blue bars).

Among earthfill dams, internal erosion is the most frequent cause, closely followed by overtopping. In contrast, rockfill dams show fewer failures overall, with overtopping being the most common issue. Structural failure is the least frequent for both types.

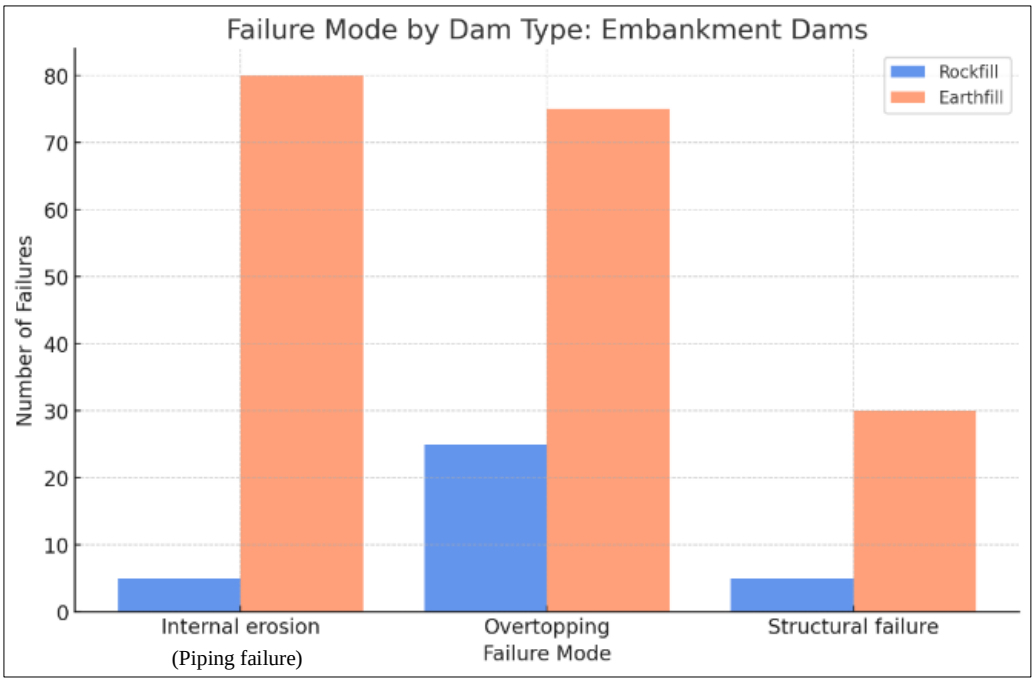

Figure 1.1 Comparison of frequency of failure modes for rockfill and earthfill dams (adapted from ICOLD (2019) with modifications).

This section discusses significant dam failure incidents and their respective times of occurrence. The dam analyzed in this thesis is a clay-cored rockfill dam, which is representative of the types studied for failure mechanisms in embankment dams. While this type of construction is effective under certain conditions, it is susceptible to specific failure mechanisms, making it a valuable case for evaluating structural integrity and failure risks.

The Taum Sauk Dam in the US experienced a catastrophic failure on December 14, 2005, when overtopping led to rapid embankment erosion, culminating in a breach that emptied the reservoir within approximately 25 minutes (Charles et al., 2011).

The Tous Dam in Spain, a 70-meter-high rockfill structure, failed on October 20, 1982, as intense rainfall triggered overtopping. The breach resulted in extensive downstream damage, necessitating the evacuation of nearly 100,000 people (Kumar & Sharma, 1992).

In 2005, Pakistan's Shakidor Dam, a rockfill embankment, failed due to overtopping following extreme rainfall. This incident caused significant downstream flooding, underscoring the risks of undersized spillways in rockfill dams (Charles et al., 2011).

The Castlewood Dam in the US, failed on August 3, 1933, when an intense thunderstorm caused overtopping. The breach formed within 30 minutes, releasing a massive flood that devastated downstream areas and highlighted the critical need for well-designed spillways in rockfill dams (Charles et al., 2011).

The Frias Dam, a 15-meter-high structure in Argentina, suffered a breach in 1970 due to overtopping during a flood, which rapidly eroded the embankment within 15 minutes. This tragic event led to over 42 fatalities, underscoring the severe risks associated with inadequate spillway capacity (Charles et al., 2011).

California’s Hell Hole Dam, completed in 1966, experienced a major failure shortly after construction due to overtopping from an unprecedented storm. The breach, forming within 45 minutes, emphasized the importance of designing spillway capacities capable of handling rare but extreme flood events (Kumar & Sharma, 1992), (Froehlich, 2016).

Finally, California’s Lower Otay Dam failed on January 27, 1916, due to extreme flooding caused by heavy rainfall. The breach took 60 minutes to form, resulting in extensive downstream flooding and leading to significant damage and loss of life (Bernard-Garcia & Mahdi, 2022).

1.3 Problem Statement and Research Objectives

The review of existing literature on dam breach analyses and risk assessments reveals several challenges and gaps. The limited attention given to uncertainty and sensitivity analysis in dam breach scenarios is a significant concern. Critical parameters, such as breach width and the time to develop a full breach (t_f), have not been comprehensively studied. This lack of in-depth analysis complicates accurate flood propagation and timing predictions, both of which are crucial for practical risk assessment.

Additionally, many studies fail to adequately consider the influence of topographical data and mesh size on flood modeling accuracy. The resolution of digital elevation models (DEMs) and mesh sensitivity in 2D simulations can significantly impact the results, particularly regarding flood extent and water depth predictions. The lack of comprehensive analysis of the effects of different DEM resolutions represents a significant gap in the current research.

A further limitation is the scarcity of comparative studies between dynamic wave and diffusion wave models, commonly used for simulating flood propagation during dam breach events. The precision of these models in capturing the complex behavior of water movement remains uncertain, especially in large-scale simulations, potentially leading to inaccuracies in flood predictions.

Moreover, the literature demonstrates insufficient attention to identifying populations at risk in the event of dam failure. Methods for estimating affected populations and optimizing evacuation strategies are often underdeveloped, which limits the effectiveness of disaster management and risk mitigation efforts in downstream areas.

Finally, the number and scope of flood risk assessments based on dam breach scenarios in Turkey are limited. Most studies utilize one-dimensional (1D) models, which may not fully capture the complexities of flood propagation and inundation. Particularly for hazard assessment studies, two-dimensional (2D) models are more

effective in representing flow over a floodplain, whereas one-dimensional models adequately capture flow processes within channels (Falter et al., 2013). In this context, the absence of two-dimensional (2D) modeling hampers accurate risk assessment and the implementation of effective flood prevention measures.

This study has two main objectives. The first is to analyze various possible failure scenarios of the Samsun Ondokuz Mayıs Dam, including conducting two-dimensional simulations to determine which scenarios result in the highest peak flood discharge and the shortest time to reach the downstream area. The second objective is to calculate the economic damage caused by flooding in the downstream region, comparing the damages across different scenarios.

Various factors influence the consequences of dam failure, such as breach parameters, the mesh structure of the numerical model, the level of detail in the digital elevation model, numerical solution methods used for hydraulics, and breach prediction techniques. The present study thoroughly examines the impact of these factors on the failure outcomes and the contribution of the numerical solution methods used.

CHAPTER 2

LITERATURE REVIEW

This thesis builds upon the earlier work of Ashraf (2021), presenting comprehensive approaches to key issues that influenced the results of the Ondokuz Mayıs Dam breach analysis. Ashraf conducted a dam-break analysis for the Ondokuz Mayıs, İhsaniye, and Avcıdere Dams using the full momentum HEC-RAS and dynamic wave FLO-2D models. The study included an accurate assessment of elevation data by comparing records from the Land Registry (Tapu Kadastro) and DSI. This led to developing a new Digital Elevation Model (DEM) that was later employed in flood modeling. Additionally, model calibration for the Ondokuz Mayıs Dam was performed by adjusting roughness values through the trial-and-error method.

Ashraf (2021) analyzed the effects of different grid resolutions on flood modeling results in his thesis using HEC-RAS and FLO-2D models. Simulations with grid sizes of 5 m, 10 m, 25 m, and 50 m have shown that finer grids have provided more accurate and consistent flow depth predictions. However, as the grid size has increased, model accuracy has decreased, and error rates have grown. At the same time, larger grid sizes have significantly reduced simulation time, highlighting the trade-off between computational efficiency and prediction accuracy. This emphasizes the need to balance model precision with computational cost.

Ünal (2019) conducted dam-break analyses of the Berdan Dam using HEC-RAS to identify potential flood risk areas and develop emergency action plans. The simulations were performed for piping and overtopping scenarios, and inundation maps were generated to represent flood depth, velocity, water surface elevation, and flood arrival time.

Karakaya (2005) conducted numerical dam-break analyses of the Kirazlıköprü Dam under various hydraulic scenarios. The numerical model was implemented using

FLDWAV, developed by the National Weather Service (NWS) in the United States, to investigate the potential adverse effects of dam failure on the downstream region.

Morris (2013) emphasized that understanding, predicting, and preventing the breach process is a top priority for dam owners and flood risk managers, as breach prediction plays a critical role in flood risk assessment. However, Morris (2005) noted that the accuracy of predicting only the peak value of the flood hydrograph was generally within ±30 to 40% of observed values. On the other hand, estimating breach formation time and dimensions was even more uncertain. In his study, Morris provides new insights and improved methods for predicting the initiation and progression of breaches in earthen dams or flood embankments.

In the study conducted by Alppay (2019), the primary objective was to identify high-risk areas downstream of the Kirazdere (Yuvacık) Dam in case of a potential dam failure. The simulations were performed using HEC-RAS software, where appropriate dam breach parameters were selected for the scenario. The analysis focused on dam-break flooding in the study area, generating flood wave propagation maps, including depth, velocity, and inundation maps. The dam-break flood wave path, hydrographs, and high-risk zones downstream of the Kirazdere Dam were also identified.

Ekmekcioğlu (2022) conducted comprehensive flood risk analyses across all districts of Istanbul, using various multi-criteria decision-making methods such as the fuzzy analytic hierarchy process (AHP), DEMATEL (Decision-Making Trial and Evaluation Laboratory), and VIKOR (VIseKriterijumska Optimizacija i Kompromisno Resenje). These methods helped identify hazard-related factors like stormwater pipe networks and imperviousness and vulnerability factors such as population density and income levels. In addition to creating flood risk mapping, advanced strategies were developed to reduce the flood risk in risky areas. (Ekmekcioğlu, 2022)

Spor (2023) conducted a study to identify flood-prone areas along the Dinsiz Stream within the Sakarya Sub-Basin, specifically assessing flood damage in the Hendek 2nd Organized Industrial Zone. Two-dimensional hydraulic models were employed to facilitate this investigation. The study involved utilizing the HEC-HMS software to convert rainfall data into flow rates, essential for generating flood hydrographs. Subsequently, the HEC-RAS program produced flood propagation maps for various return periods (Q_{50}, Q_{100}, Q_{200}, and Q_{500}). Furthermore, a comprehensive approach to damage assessment was adopted, incorporating methodologies such as HAZUS-MH alongside traditional damage estimation techniques. The findings culminated in developing detailed flood risk maps, emphasizing vulnerable regions and the potential impacts of flooding, thus contributing valuable insights for flood risk management strategies. (Spor, 2023)

Çalamak (2016) assessed the flood-induced overtopping reliability of the Tanyeri Dam using probabilistic methods. In this context, flood hydrographs and pre-flood reservoir water levels were randomly generated through Monte Carlo simulation, and the probability of exceeding the dam crest was analyzed. The study considered scenarios where the spillway and the bottom outlet were not operational. The results showed no risk of overtopping during floods with a 10,000-year return period even when the spillway is operational. Additionally, it was determined that the maximum reservoir water level reached during the flood directly depends on the pre-flood water level.

Kocaman (2019) conducted dam-break analyses of the Kartalkaya Dam using roughness data derived from the European Environment Agency-prepared CORINE map. Simulations were performed with HEC-RAS and FLO-2D software, and the results for flow depth and velocity downstream of the Kartalkaya Dam were compared.

Apel et al. (2009) utilized 1D/2D and detailed 2D hydraulic modeling techniques to simulate the August 2002 flood in Eilenburg, East Germany. They estimated damage and associated economic losses for residential buildings at micro and meso scales.

The analysis demonstrated that the combination of the 1D/2D model and the mesoscale damage model provided the best balance between data requirements, simulation effort, and acceptable accuracy of the results.

Beden and Ulke (2021) studied the economic impacts of flooding by comparing different flood damage estimation methodologies across various flood events. They utilized 1D/2D coupled hydrodynamic modeling with MIKE FLOOD software to simulate scenarios in the Ceviz Stream basin of the Ünye district.

The study by Coşkun and Yanmaz (2001) is a pioneering effort in Turkey to develop a water depth-damage ratio curve, featuring a case study on the hydrological design of a bridge in the Vakfıkebir district of Trabzon, which frequently experiences flooding. Based on the maximum water depths calculated for different recurrence intervals in the valley, a detailed hydro-economic analysis has been conducted on the potential physical damages caused by floodwaters and their costs. The flood risk map of the area has been prepared, and the relationship between costs and recurrence periods has been assessed. This comprehensive evaluation has determined how resilient the bridge and surrounding structures are against flood risks and how economically they can be protected.

Alonso et al. (2008) studied the diffusive wave approximation (DWE) and demonstrated that this method provides a suitable model for low-velocity water flows. Their research showed that the DWE yields accurate results in flow conditions dominated by gravitational forces and shear stress. Additionally, the study clarified the influence of water surface slopes on flow dynamics. The findings indicate that the method is physically consistent for modeling low to moderate-velocity flows but is limited to scenarios where topographic effects are neglected.

Şahin (2016) studied the effect of different mesh sizes on flood modeling results using FLO-2D software. The study found that changes in mesh size did not significantly affect the total inundation area, though some differences appeared with the smallest mesh sizes. Computational time remained stable up to a certain threshold but increased noticeably with smaller mesh sizes. It was observed that finer meshes

captured local depth variations more accurately, especially under different hydrographs and flow scenarios. The study suggests balancing model accuracy and computational cost, recommending medium-sized meshes (30-50 m) as the optimal choice for large-scale flood models. (Şahin, 2016)

Najar and Gül (2022) applied five breach prediction methods using a 2D HEC-RAS model to simulate flood hydrographs for a hypothetical breach of the Ürkmez Dam, which presents high downstream risk. Sensitivity analysis on reservoir levels revealed that Froehlich provided the most reliable breach predictions. Results showed that breach formation time significantly impacted peak discharge and time to peak, while side slope had minimal influence. The study offers guidance on key parameters to reduce uncertainty in dam-breach modeling.

Yılmaz et al. (2023) analyzed flood hazards due to overtopping and piping failures at Dalaman Akköprü Dam using a 2D hydraulic model. The study compared shallow water equations and diffusive wave equations, highlighting differences in flow depth, velocity, and hazard levels. Results showed that most settlements in the basin faced a high risk of structural damage, emphasizing the necessity of early warning systems and evacuation plans.

Marangoz et al. (2024) investigated the impact of dam breach parameters such as breach side slope, final bottom width, final bottom elevation, weir coefficient, breach formation time, and initial elevation of reservoirs on breach peak flow and time to reach the peak. The findings indicated that the initial water elevation, final bottom elevation, and breach development time significantly affected both the peak flow of the breach and the time taken to reach that peak. In contrast, the breach side slope did not substantially affect the time to peak and had only a minimal influence on the peak discharge.

Turkel et al. (2024) conducted a probabilistic analysis of potential dam failure scenarios at Kanlikoy Dam, integrating hydrologic and hydraulic modeling techniques. The study employed HEC-HMS and 2D HEC-RAS models to simulate flood hydrographs and inundation maps for different failure mechanisms, including

piping, extreme rainfall events with a 100-year return period, and probable maximum precipitation (PMP). Additionally, Monte Carlo simulations using McBreach software produced hydrographs for exceedance probabilities of 90%, 50%, 10%, and 1%. The results demonstrated that these failure scenarios pose significant risks to downstream agricultural and residential areas, with the potential for substantial structural damage and infrastructure loss.

As can be seen from the mentioned studies, research in Turkey has primarily focused on dam break analyses using various software, and the results have been evaluated. However, no comprehensive study has been found that examines the combined effects of breach parameters, numerical model grid structures, breach prediction techniques, and numerical solution methods on flooding caused by dam failure. Furthermore, the literature has not extensively explored flood risk assessment studies involving dam break flows. To address this gap, a comprehensive research effort has been undertaken.

2.1 Primary Causes Leading to Dam Failure

Embankment dams encounter several problems in terms of dam safety. The dam embankment slopes must be adequately stable to withstand all foreseeable loading conditions. (ICOLD, 2013)

Stability problems on embankment dam bodies have various causes: Ensuring a dam's stability requires that all structural components remain balanced under load. The risk of sliding or collapse can increase when the dam embankment and foundation encounter unexpected conditions, such as heavy rainfall or excessive water pressure. Stability analyses evaluate whether the embankment materials can maintain balance under load and pressure. If stability cannot be ensured, serious failures may occur, such as deformation, sliding, or even structural collapse of the dam embankment.

Uncertainty in soil strength parameters: Accurately determining the strength properties of soil material is essential for dam safety. Stability-critical parameters, such as the strength and deformation characteristics of rock or fill materials, are identified through laboratory or field tests. Inaccurate measurements of these parameters or using soil with insufficient strength can reduce the shear resistance of the dam embankment, thereby increasing the risk of failure.

Effects of water pressure and saturation on material strength: Exposure to water pressure can affect the durability of the dam embankment. Increased water saturation can weaken the material and potentially lead to sliding.

Inadequate spillway capacity and flood passage: The ability of a dam to withstand flood loads during heavy rainfall or flood events depends on the adequacy of the spillways. If the spillway capacity cannot accommodate maximum flood levels, serious consequences may occur, such as water overtopping the dam embankment. In this case, the excessive water load can damage the dam embankment and create flood loads that threaten the dam's stability. Proper determination of spillway capacity is essential to minimize flood risks.

Effects of dynamic loads (seismic loads): Dynamic loads such as earthquakes can significantly impact the dam embankment and foundation, compromising stability. The dam's behavior during an earthquake is estimated through dynamic analysis of the embankment, and the resulting deformation values are checked to see if they remain within allowable limits.

Seepage analyses: Water seepage within the dam embankment and foundation can lead to erosion, especially in sandy and fine-grained soils, reducing stability. Seepage analysis aims to assess the dam's capacity to control water leakage. If the seepage rate is high, it can lead to erosion and piping formation, compromising the dam's durability.

Backward erosion piping and piping erosion risk: Backward erosion piping refers to the process where seepage gradually carries fine-grained soils, creating pipe-like

voids. This process can undermine the dam's foundation, significantly weakening the stability of the embankment. Piping events, especially in fill or sandy soil, are common mechanisms that often lead to dam failures.

The factor of safety against heaving: Heave is the upward movement of soil caused by uplifted water pressure. When this pressure exceeds the weight of the soil, heaving occurs, leading to instabilities in the dam embankment. Heave analysis aims to assess the soil’s safety against water pressure; if water pressure increases, displacement or sliding may occur in the dam embankment.

CHAPTER 3

STUDY AREA AND METHODOLOGY

3.1 Methodology of the study

This section summarizes the overall stages in the study methodology conducted on the Ondokuz Mayıs Dam. This methodology effectively integrates flood modeling, risk assessment, and economic analysis to evaluate dam stability and failure risks. Initially, data were collected, and the likelihood of the dam's potential failure was thoroughly investigated. Subsequently, the impact of key failure issues in dam break analysis on the outflow hydrograph was thoroughly explored. Dam break flood simulations were conducted for the developed scenarios, particularly identifying the potential flood damages and economic losses in the downstream residential areas under the most critical piping and overtopping scenarios. The conclusions section extensively discussed the findings, and significant insights were derived. Figure 3.1 illustrates the step-by-step methodology employed in the study of the Ondokuz Mayıs Dam.

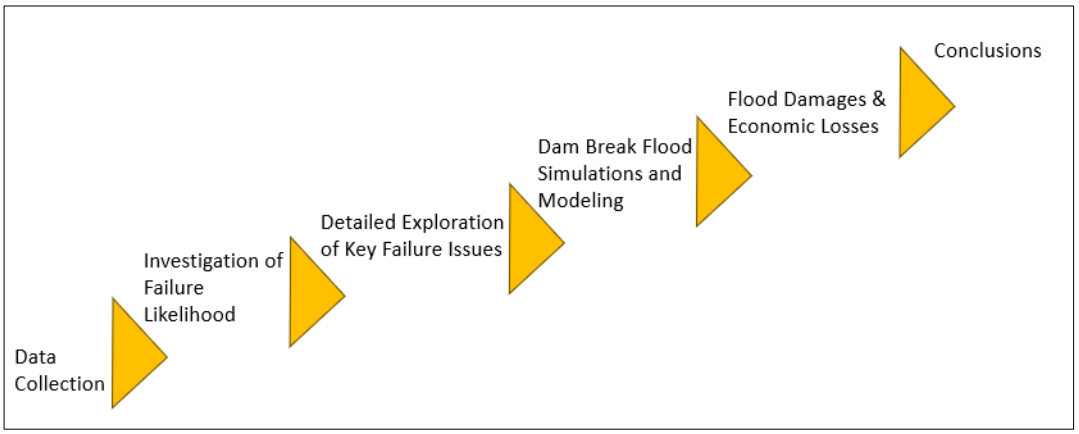

Figure 3.1 Schematic representation of the research methodology steps for the Ondokuz Mayıs Dam study

3.2 Location of the study area

In this study, the Samsun Ondokuz Mayıs Dam (Figure 3.2) was selected because the dam's downstream area has a potential flood risk zone and there is an absence of existing data on the site. Ondokuz Mayıs Dam, constructed in 2017 with a height of 89.75 m and a crest length of 507.10 m for the purpose of irrigation, is a clay core rockfill dam featuring an uncontrolled overflow spillway. The dam's upstream and downstream slopes are designed with a 2.0H:1.0V ratio. (State Hydraulic Works, 2013) The cross-section of Ondokuz Mayıs Dam is presented in Figure 3.2.

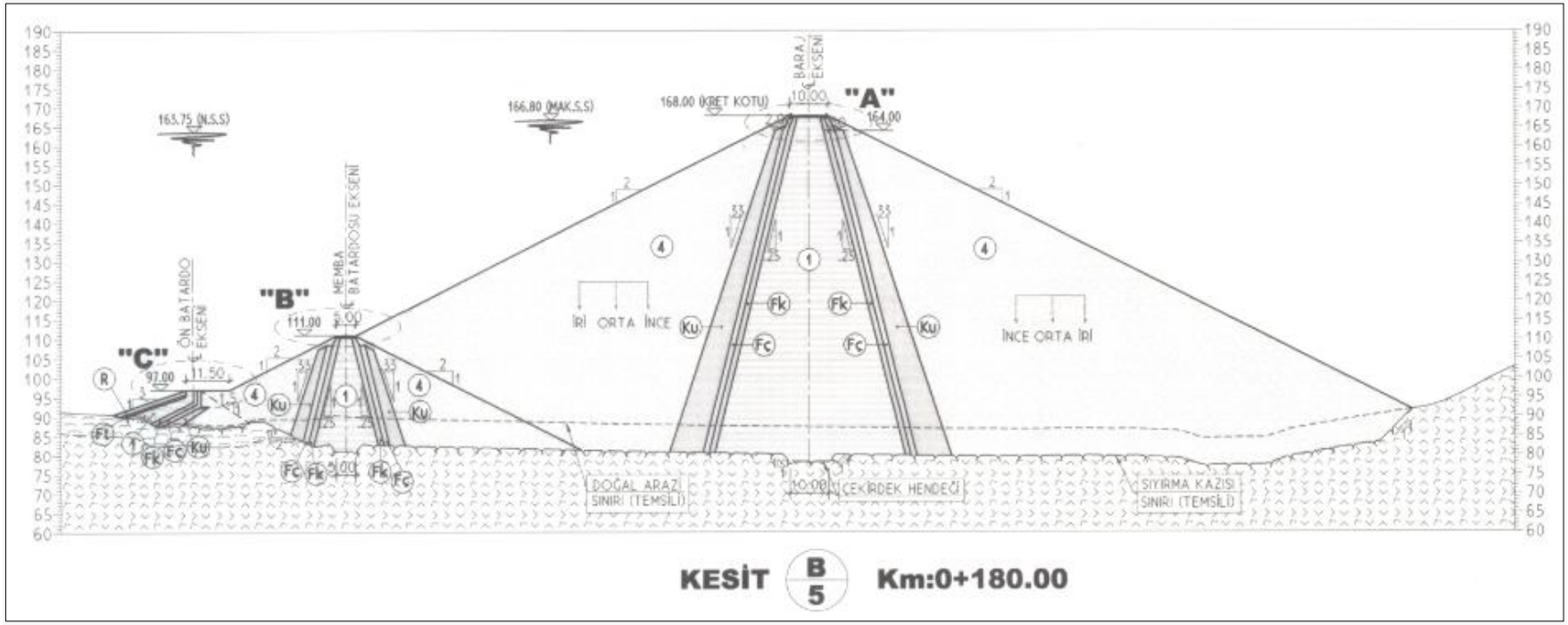

Figure 3.2 Cross-section of Ondokuz Mayıs Dam (DSI, 2013)

The primary function of Ondokuz Mayıs Dam is to provide water for both municipal and agricultural needs. Municipal water will be supplied to Ondokuz Mayıs District, Bafra District, and four towns in the Bafra Plain. 7,555 ha area is planned for irrigation using a pressurized system. The population of Ondokuz Mayıs District is 25,893 (2019). The dam's key characteristics are listed in Table 3.1. (Ashraf, 2021)

Table 3.1 Ondokuz Mayıs Dam characteristics

Ondokuz Mayıs Dam Body properties	
Type	Clay core rockfill dam
Crest elevation (m)	168.00
Height from thalweg (m)	80.75
Height from foundation (m)	89.75
Crest length (m)	507.10
Crest width (m)	10.00
Total body fill volume (m^3)	3,888,527
Ondokuz Mayıs Dam reservoir properties	
Minimum water level (m)	106.30
Normal water level (m)	163.75
Maximum water level (m)	166.80
Normal reservoir volume (hm^3)	59.27
Maximum reservoir volume hm^3)	65.93

The basin's catchment area is 133.50 km^2. The project area's only stream is the Engiz Stream. Located on the right bank of Kızılırmak, Engiz Stream was formed by the merger of Erikli and Kösedik streams originating from Kocadağ (Ashraf, 2021). It travels approximately 32 km and flows into the Black Sea from Ondokuz Mayıs district. The Ondokuz Mayıs Dam is in a topographically diverse area characterized by hilly terrain with steep slopes. In contrast, the lower portion of the basin is located in flat plains, exhibiting a gentle slope.

Figure 3.3 shows the area location map while Figure 3.4 shows the drone view of the dam. The upstream face of the dam is shown in Figure 3.5.

Figure 3.3 Project area location map (DSI, 2013)

Figure 3.4 The drone view showing the reservoir and the body of Samsun Ondokuz Mayıs Dam

Figure 3.5 The upstream face of the Ondokuz Mayıs Dam (2023)

According to the latest earthquake hazard map prepared by AFAD (Disaster and Emergency Management Authority of Turkey), the Ondokuz Mayıs district of Samsun is in the 1st-region earthquake zone (low acceleration), Figure 3.6.

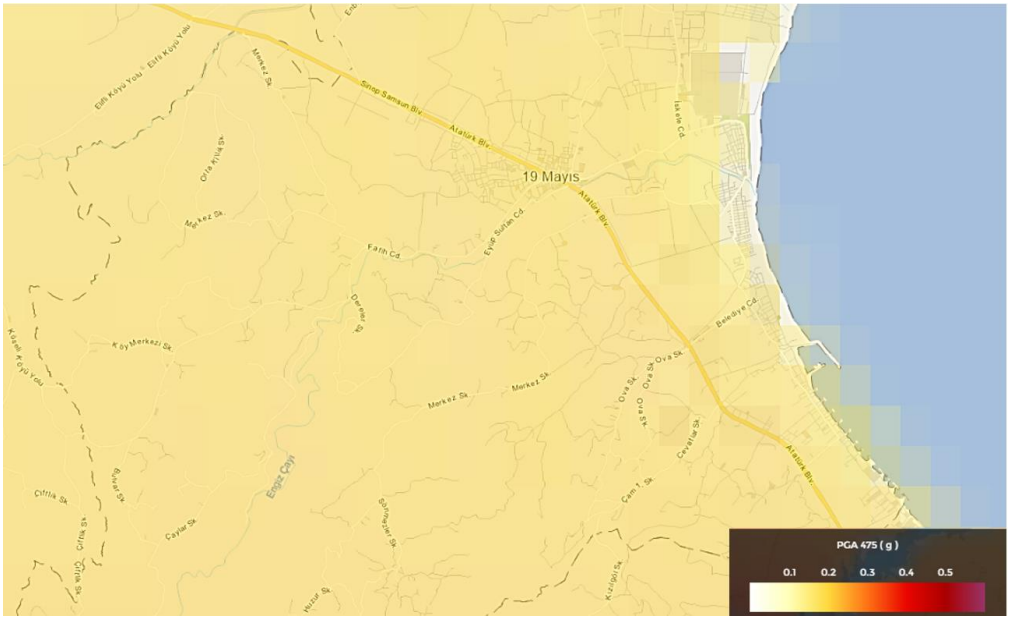

Figure 3.6 Samsun seismic hazard map prepared by AFAD

According to the Turkey Earthquake Zones Map prepared by the General Directorate of Disaster Affairs of the Ministry of Public Works and Settlement in 1996, the project area is also located on the border of the 3rd-degree Earthquake Zone (low acceleration), Figure 3.7.

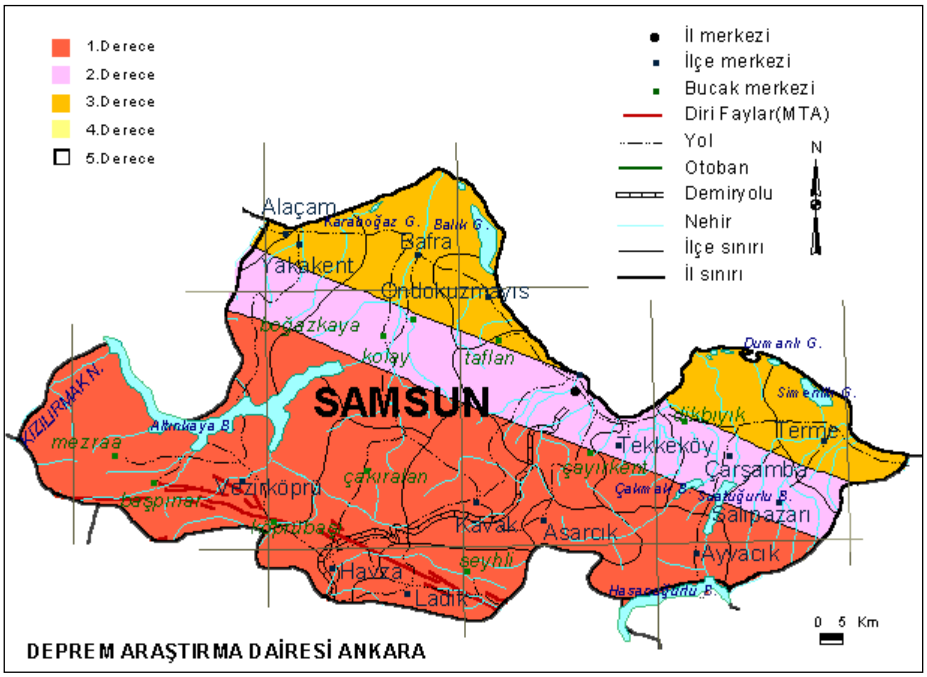

Figure 3.7 Samsun seismic hazard map prepared by the Earthquake Research Department of the Disaster Affairs General Directorate in 1996

On the other hand, examining the disaster risk map shows that the coastal areas of Samsun have a high risk of landslides and flooding, Figure 3.8. In June 2023, the city experienced severe flooding due to intense rainfall, transforming streets into torrents and significantly damaging properties, particularly within the Atakum District (Daily Sabah, 2024). According to information from local news sources, precautionary measures were implemented at the Ondokuz Mayıs Dam, releasing water from the dam's spillway in response to excessive rainfall and rising water levels. Residents in the downstream areas were notified to ensure their safety. Such interventions are crucial for maintaining the dam's integrity and mitigating flood

risks in the region, highlighting the importance of proactive flood management strategies. (Kanal 362, 2024)

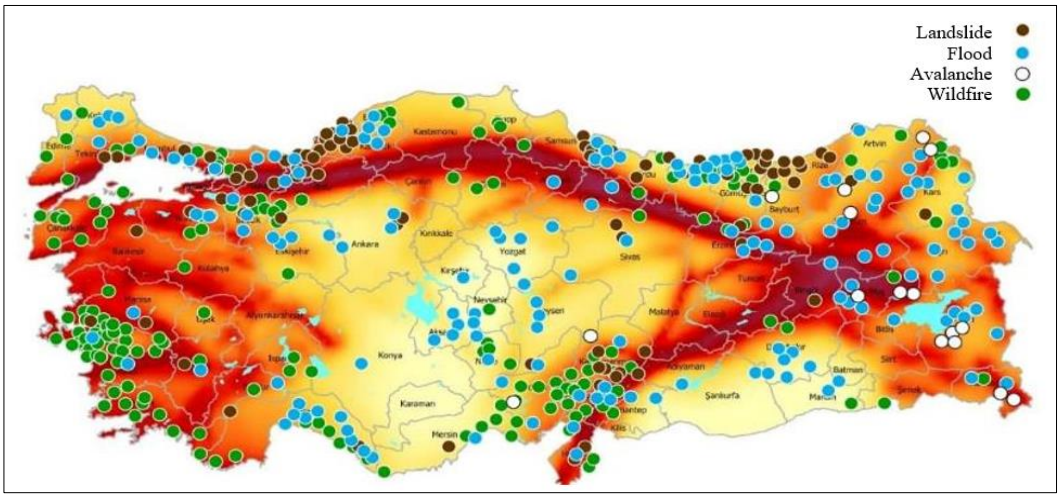

Figure 3.8 AFAD's disaster risk map of Turkey

3.3 Data Collected for This Study

The digital elevation model (DEM) used in this study incorporates calibrated roughness values derived from Ashraf (2021), as shown in, Figure 3.9. In Ashraf (2021), the DEM was validated using elevation data obtained from the General Directorate of Land Registry and Cadastre and the State Hydraulic Works (DSI). Within the scope of his thesis, Engiz Creek was divided into two sections: Reach 1 and Reach 2, and Manning roughness values for these areas were calibrated based on flow data from a gauging station located along the river. Additionally, land use data sourced from Google Earth was employed to assign Manning values according to various land uses, as suggested by Chow (1959).

Building upon the calibrated model and validated DEM used in Ashraf (2021), the present study has further integrated buildings into the map to improve the accuracy of the analysis. This incorporation, alongside the topographical model employed by Ashraf (2021), improves the analytical precision of the flood assessments. By including architectural features, the modeling process accounts for the impact of

built-up areas on flood dynamics, ensuring a more comprehensive understanding of flood behavior in the studied regions.

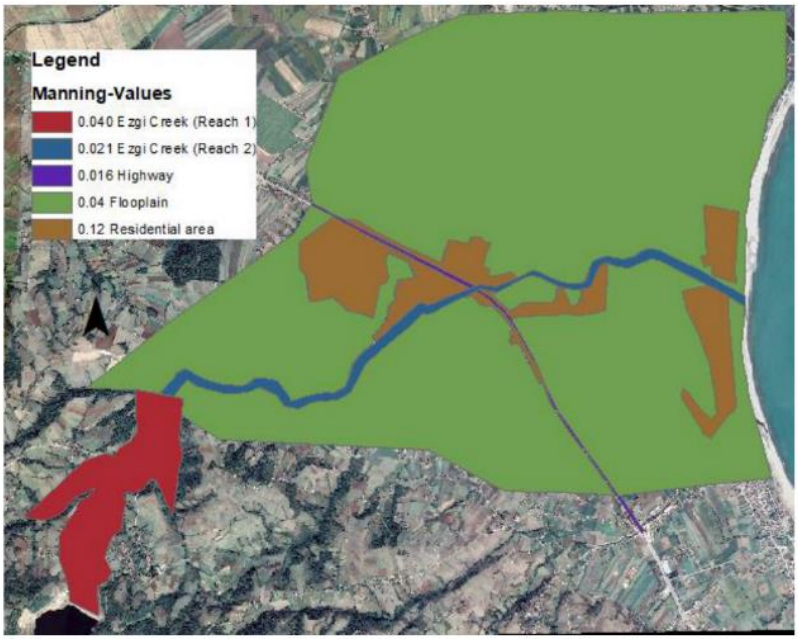

Figure 3.9 Ondokuz Mayıs Dam downstream land use shapefile (Ashraf, 2021)

3.3.1 The Hydrologic Data

The project design floods for the Ondokuz Mayıs Dam were taken from an approved planning report by DSI (2011), based on outdated data. To rectify this, updated maximum precipitation data from the Engiz DSI Station and flow measurement records from the active gauging station D15A026 monitoring Engiz Creek were utilized to revise the design flood, probable maximum flood, and other different flood return periods. Additionally, the reservoir operation study has been updated based on current data, and it identified specific seasons when water levels in the reservoir have risen, indicating potential overtopping risks.

3.3.2 Digitizing the Structures

The area's flood risk severely threatens both land parcels and buildings. Building locations were identified using remote sensing data. For this purpose, Google Maps was used to digitize each building in the region. The most recent images, from March 2024, were used as the basis for the analysis, Figure 3.10.

Figure 3.10 Google image of the Samsun Ondokuz Mayıs District.

The representation of resistance caused by buildings or other structures in flood modeling in urban environments is recognized as a crucial parameter. (Bellos & Tsakiris, 2015). Based on current scholarly literature (e.g., Bellos, 2012), the methods for simulating water flow between structures involve various representations. These include excluding solid structures depending on the numerical method or scheme used, the localized elevation increases of these structures, which converts a Digital Terrain Model (DTM) to a Digital Elevation Model (DEM), and the localized increase in roughness within the solid areas. According to Bellos (2012), the primary determinant in flood modeling within urban settings is accurately representing the resistance created by houses or other objects in the model. This increase can be achieved by raising the Manning coefficient or by incorporating additional friction terms into the momentum equations. (Schubert & Sanders, 2012)

Within the scope of this thesis, buildings in floodplains are represented by solid regions that have been extruded to the height of the corresponding number of floors by region. Figure 3.11 shows some photographs taken during the field visit from the town center. The stories of buildings are determined according to the floor density in each neighborhood due to the field study in the Ondokuz Mayıs District, Figure 3.12

Figure 3.11 A photo from a site inspection of Ondokuz Mayıs District

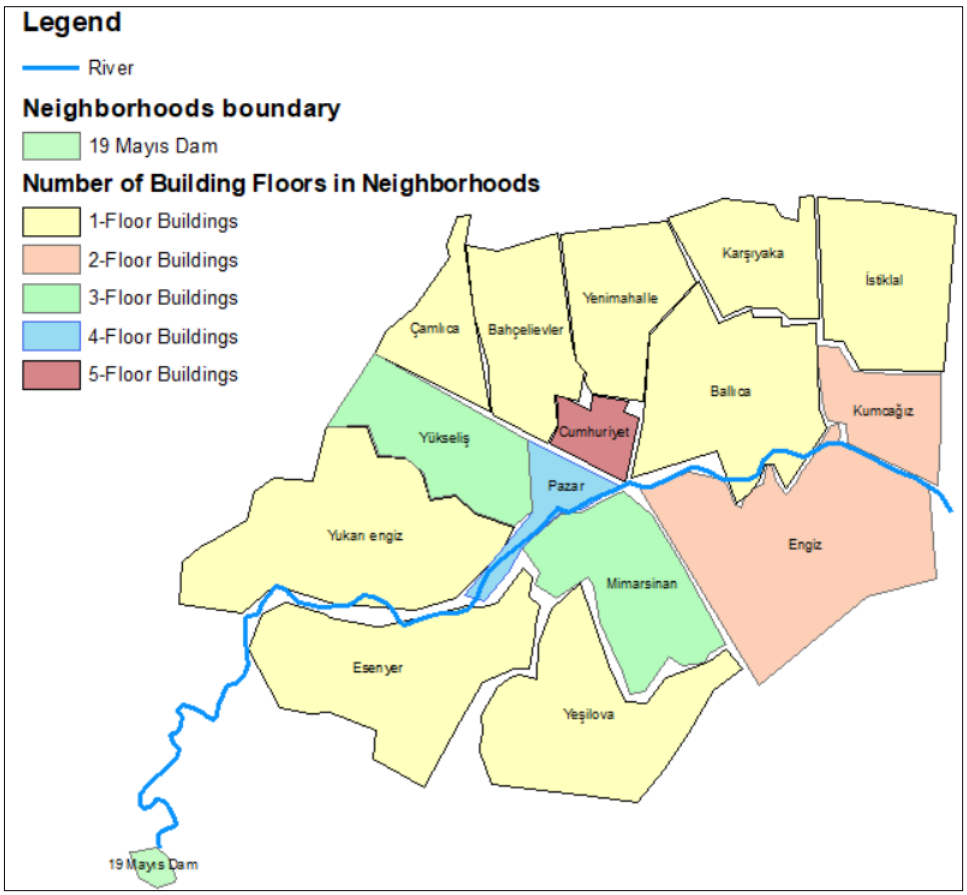

Figure 3.12 The distribution of floor densities in each neighborhood, as obtained from a field survey

3.3.3 Determination of Number of the Stories for Buildings

During the visit to the Ondokuz Mayıs Dam and its district in Samsun, a study was conducted to determine the number of floors of buildings across all neighborhoods in the district. For instance, observations indicated that three-floor buildings were predominant in the Yükseliş neighborhood, while single-floor buildings were more prevalent in the İstiklal neighborhood. Below are sample photographs taken from the neighborhoods during the site visit.

The areas shown in Figure 3.13 include a) Yukarı Engiz District b) Esenyer District c) Bahçelievler District d) Ballıca District e) Çamlıca District f) Yeşilova District g)

Cumhuriyet District h) İstiklal District i) Engiz District j) Karşıyaka District k) Kumcağız District l) Mimarsinan District m) Pazar District n) Yükseliş District o) Yenimahalle District

Figure 3.13 Example of categorization of house types in the Ondokuz Mayıs flood areas

Figure 3.13 (continued)

Figure 3.13 (continued)

The CORINE land use map was also used during the determination process. Figure 3.14 shows the Corine land use map of the Ondokuz Mayıs region. Corine land use data were used to verify the findings from the site visit. For example, during the site visit, the İstiklal Neighborhood was identified as predominantly consisting of single-floor buildings, corresponding to the Corine code 212 for mixed crops. On the other hand, the Cumhuriyet Neighborhood, where five-floor buildings were assumed, corresponds to the Corine code 112 for discontinuous urban fabric.

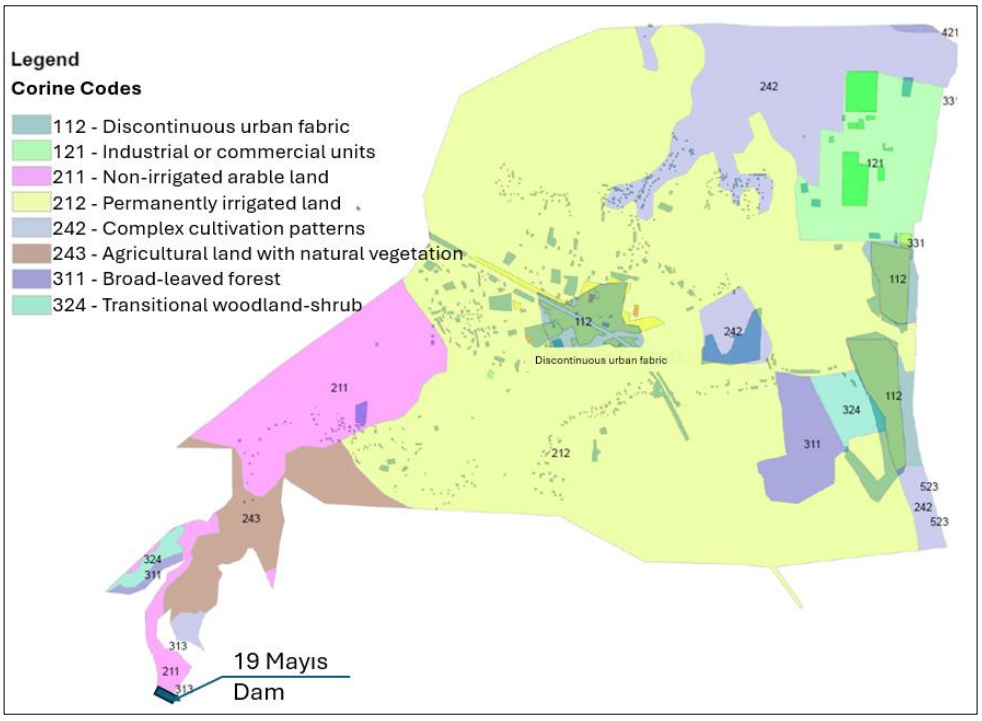

Figure 3.14 Corine land use map of Ondokuz Mayıs region

Incorporating building groups into the Digital Elevation Model aims to better simulate flooding in the area by including a simplified representation of the city's configuration. In the past, experimental studies have been conducted to assess the impact of structures on flooding. The results of these studies are mutually supportive, highlighting the significance of accurately representing buildings, (Mustafa and Szydłowski, 2021), (Marangoz and Anilan, 2022), (Bellos and Tsakiris, 2015), (Haltas et al., 2016), (Beretta et al., 2018), (Brown et al., 2007), (Guinot, 2012) , (Ramirez et al., 2016), (Bellos, 2012).

A new raster has been compiled alongside the existing Digital Elevation Model (DEM), which incorporates the building heights, to create a DEM that includes the building heights. Figure 3.15 provides a schematic representation of how these two raster maps match. In the model where building heights are defined, 2,720 polygons have been created to represent the buildings. The polygons have been extruded based on the number of floors, and the average number of floors for the entire map is approximately two.

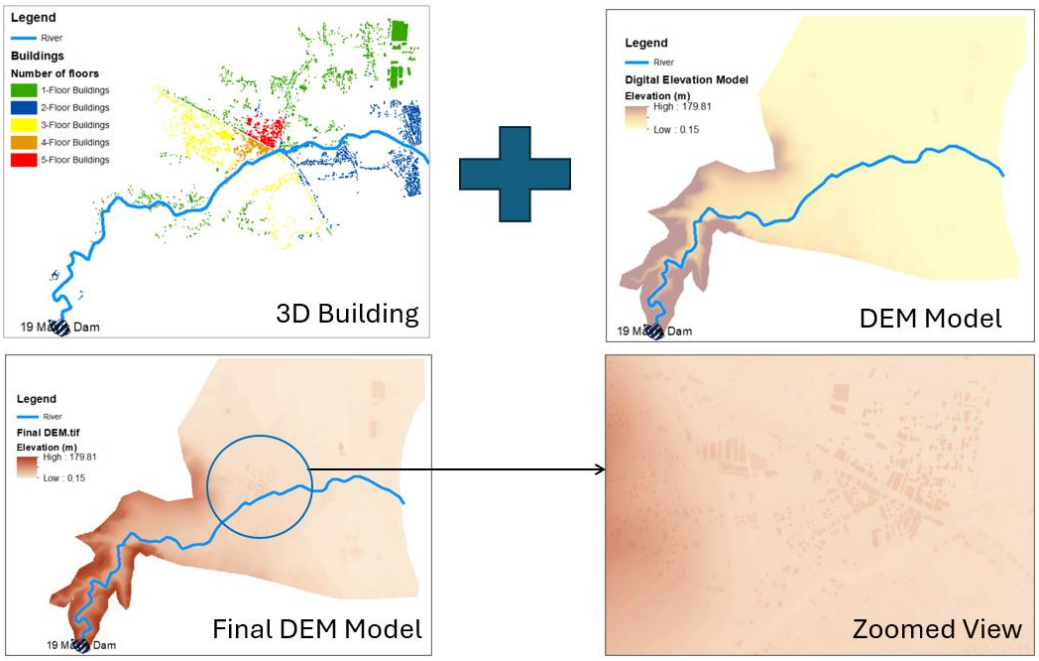

Figure 3.15 A schematic representation illustrating a new DEM that integrates building data.

Figure 3.16 below presents 3D images of the study area with 3D buildings produced using ArcScene software.

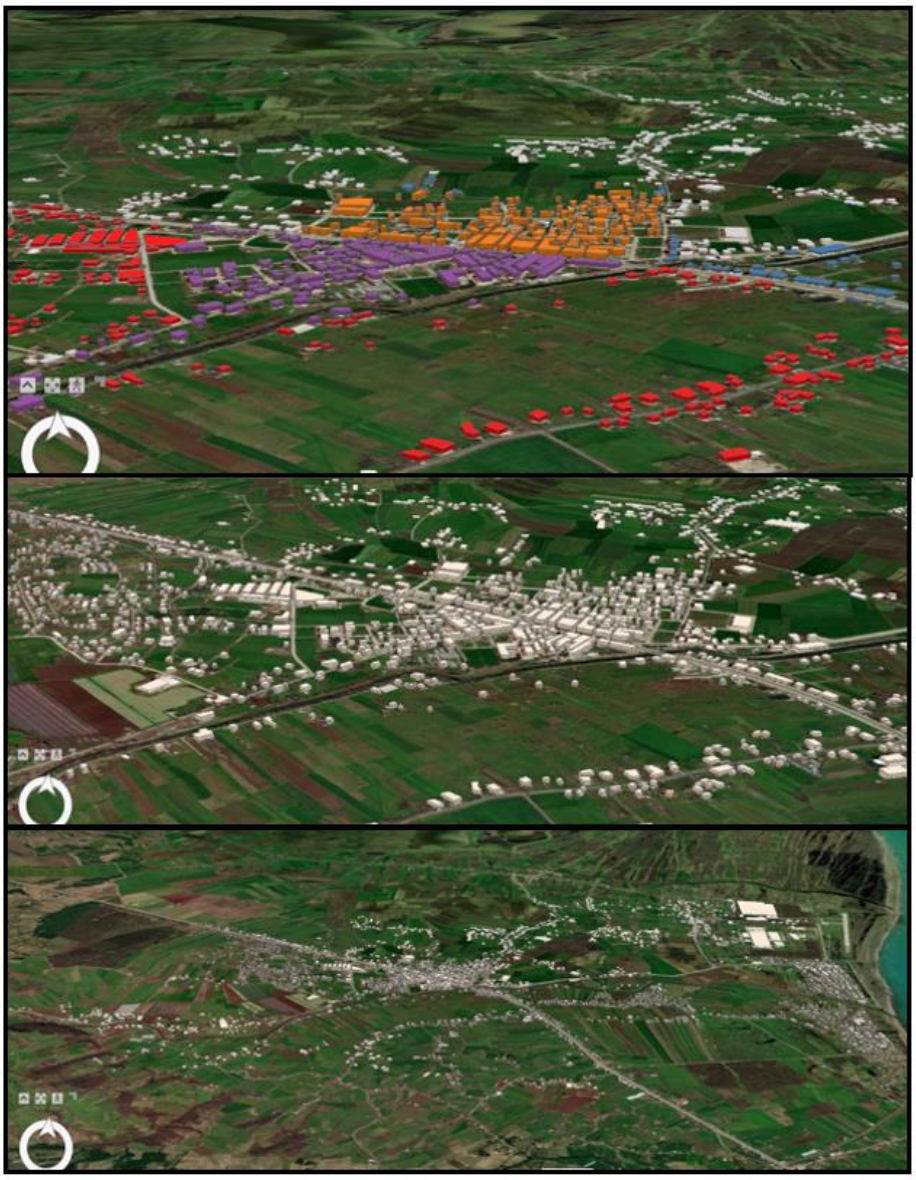

Figure 3.16 3D images of the study area with 3D buildings produced via ArcScene

3.3.4 Structure Unit Price

Building unit costs were obtained from the document titled "2024 Mimarlık Ve Mühendislik Hizmet Bedellerinin Hesabında Kullanılacak 2024 Yılı Yapı Yaklaşık

Birim Maliyetleri Hakkında Tebliğ" published by Turkey's Ministry of Environment and Urbanization (CSB).

Figure 3.17 shows the assigned floor numbers for the buildings located within the boundaries of the neighborhoods in the Ondokuz Mayıs District of Samsun.

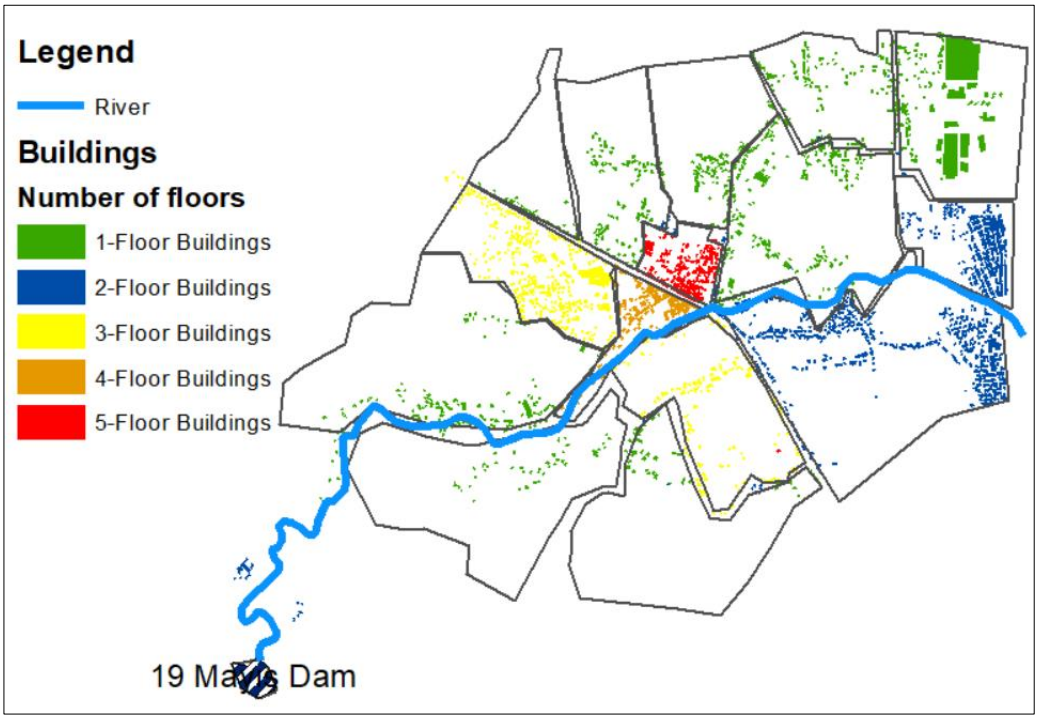

Figure 3.17 Building floor distribution visual prepared via ArcGIS (Esri, 2019, Version 10.7)

The intended use of buildings represented by 2,720 polygons marked in ArcGIS Software (Esri, 2019, Version 10.7) has been recorded in the database with an additional field. The main types of buildings entered into the database include places of worship, schools, hospitals, polyclinics, marketplaces, football fields, administrative buildings, university campuses, aquaparks, and integrated industrial structures, each with different unit costs. On the other hand, the unit costs for residential buildings vary depending on the building type or number of floors. For example, apartment-type residences less than 30.5 meters in height fall into Class IV, Group A buildings. In comparison, residences with a height of less than 21.5

meters fall into Class III and Group B buildings, and residences up to three floors (including three floors) fall into Class III and Group A buildings, as shown in Table 3.2.

After entering the relevant unit cost values (TRY/m²) for each non-residential and residential building type, the polygon areas of the buildings were calculated via ArcGIS software. In a later Section 5.3, the economic losses for each building type will be calculated separately according to the flood damage percentage for each building.

Table 3.2 Building approximate unit costs in 2024 (published by Turkey's Ministry of Environment and Urbanization.)

Structure Type	**Classification Based on Architectural Services**	**Unit Price (TRY/m²)**
Single-floor industrial buildings	Class II Buildings, Group C	7750
Sports facilities	Class III Buildings, Group A	12250
Garages	Class III Buildings, Group A	12250
Neighborhood markets	Class III Buildings, Group A	12250
Residential buildings (up to 3 stories)	Class III Buildings, Group A	14400
Gas stations	Class III Buildings, Group A	12250
Industrial facilities (workshops, manufacturing workshops)	Class III Buildings, Group A	12250
District municipality buildings	Class IV Buildings, Group B	17400
Stadium	Class IV Buildings, Group B	17400
Residential buildings (height less than 21.5 m)	Class III Buildings, Group B	14400
School	Class III Buildings, Group A	15300
Mosque	Class IV Buildings, Group A	15300
University Campus	Class V Buildings, Group A	21300
Hospital	Class IV Buildings, Group B	22250

3.3.5 Digitizing the Road Plans

The road network in the Ondokuz Mayıs district was downloaded from satellite, Figure 3.18. The length of the roads was calculated using ArcGIS software. The road concept is based on the idea that a small water depth does not cause any damage in the short term; prolonged water retention causes more damage.

Figure 3.18 Road plan extracted from satellite imagery of the Ondokuz Mayıs District.

As shown in Table 3.3, approximate bills of quantities have been calculated using unit prices obtained from the CSB. All roads are assumed to be 7 meters wide and have a bituminous surface paved road. In a later Section 5.2.2, for each dam-break scenario, the flood damage percentage for roads will be calculated, and the corresponding economic cost will be determined based on this damage rate.

Table 3.3 Approximate bill of quantities of roads prepared by the General Directorate of Highways

No	Work Item	Unit	Quantity	Unit Price (2024)	Total (TRY)
Kgm/6405	5 cm Compacted Thickness Asphalt Concrete Wearing Course (Crushed and Screened Quarry Stone) (Type-1)	m²	1887672.4	89.5	168946680.2
Kgm/6306	6 cm Compacted Thickness Asphalt Concrete Binder Course (Crushed and Screened Quarry Stone)	m²	1925425.85	105.06	202285240.1
Kgm/6308	8 cm Compacted Thickness Asphalt Concrete Hot Base Course (Crushed and Screened Quarry Stone) Type-A	m²	2026511.11	139.02	281725574.6
Kgm/6100/3	Plant-Mix Base Course Construction (Crushed and Screened Quarry Stone)	ton	731877.56	416.13	304556208.3
Kgm/6000	Subbase Construction with Crushed and Screened Material from Quarry Stone	m³	331691.01	378.99	125707575.2
Öbf-(Tupraş)	Bituminous Material Entering Construction - Batman Refinery	ton	47164.76	16623.1	368086540.8
07.006/K	Transport of Construction Materials Other Than Excavation - Over 10,000 m (Bitumen Transport) (450 km) Kırıkkale (333 km)	ton	47164.76	425.43	20065069.08
07.005/K	Transport of Construction Materials Other Than Excavation - Up to 10,000 m (Crushed Stone) (5100 m)	m³	331691.01	91	30183881.75
07.005/K	Transport of Construction Materials Other Than Excavation - Up to 10,000 m (Plant-Mix) (5100 m)	m³	684955.42	91	62330942.81

3.3.6 Digitizing the Agricultural Areas

The information about the agricultural areas within the Ondokuz Mayıs district was obtained from the Ondokuz Mayıs Planning Report and digitized as shown below in Figure 3.19.

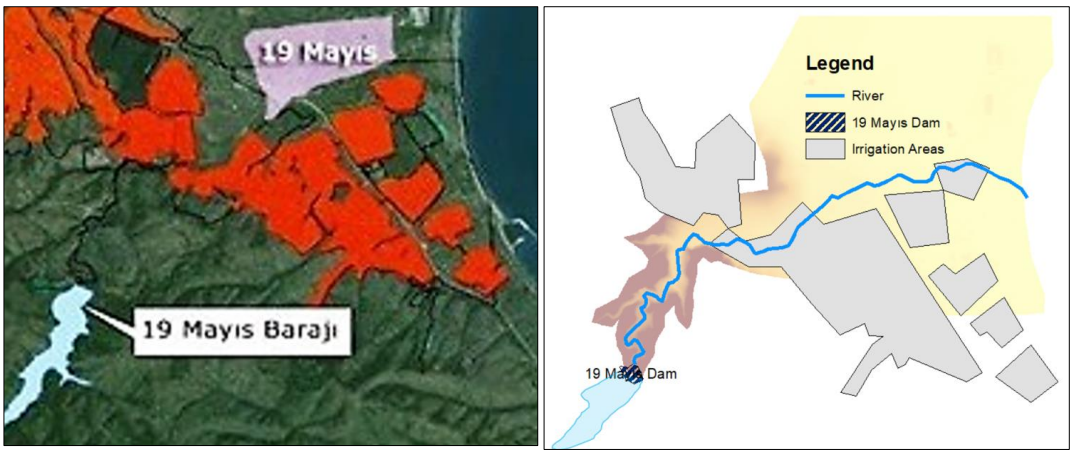

Figure 3.19 Agricultural areas in Ondokuz Mayıs District

In the Ondokuz Mayıs District, various crops are cultivated, including rice, hazelnuts, vegetables such as (peppers, tomatoes, eggplants, cucumbers, and beans), watermelon, and other fruits. The latest published unit prices for these products were obtained from the Turkish Grain Board, which is affiliated with the Ministry of Agriculture and Forestry, Table 3.4. Crop patterns and yields were sourced from Section 8: Agricultural Economy of the Ondokuz Mayıs Dam Planning Report.

Table 3.4 Yields and income of crops cultivated in the Ondokuz Mayıs District (unit price obtained from TURKSTAT website)

Crop Pattern	Crop Planting Rate (%)	Crop Yield (kg/da)	2023 Unit Price (TRY/kg)	Crop Yield (kg/m2)	TRY/m²	TRY/m²(%)
Wheat	7	500	7.64	0.50	3.82	0.27
Cow vetches (seed)	7	500	14.01	0.50	7.01	0.49
Maize	14	600	5.52	0.60	3.31	0.46
Sunflower	14	500	30.18	0.50	15.09	2.11
Fruits	25	2000	18.64	2.00	37.28	9.32
Rice	9	800	17.84	0.80	14.27	1.28
Vegetables1	7	3500	13.26	3.50	46.41	3.25
Pepper(red)	7	3250	17.25	3.25	56.06	3.92
Alfalfa (green)	10	1250	2.78	1.25	3.48	0.35
Sum	**100.00**					

The average Unit Price for 2023 is 21.46 TRY. Using the price deflator, the average price for 2024 has been adjusted to 23.15 TRY

CHAPTER 4

ASSESSMENT OF FAILURE LIKELIHOODS

This chapter rigorously evaluates the failure likelihoods of the Ondokuz Mayıs Dam through a comprehensive series of hydrological and geotechnical assessments. Firstly, it updates essential hydrological data to reassess the dam's capacity for flood control, reflecting recent flow and rainfall pattern changes. Subsequently, it explores potential geotechnical failures, such as backward erosion piping and heaves, alongside calculating the dam's safety factor. Finally, in the last part of this chapter, various slope configurations are adjusted to analyze the failure probabilities and associated costs, aiming to achieve a relatively safer and more economical design while assessing the cost-benefit ratio.

4.1 Updating Flood Discharges with Current Flow Data to Assess the Dam's Flood Control Capacity

The current spillway capacity has been evaluated to determine whether it can pass the probable maximum design flood (Q_{PMF}) derived from updated data, Figure 4.1. As mentioned in Section 3.3, the current flow measurement record is based on outdated data, so updated records of active gauging station D15A026 monitoring Engiz Creek were utilized to revise the design flood for the years 2010~2021. Flood discharges were calculated using methods recognized as valid by the State Hydraulic Works (DSI), including the Synthetic Method, Mockus Method, Point Flood Frequency Analysis, and Regional Flood Frequency Analysis, Figure 4.1 These methods provided a statistically grounded and comprehensive estimation of flood discharges.

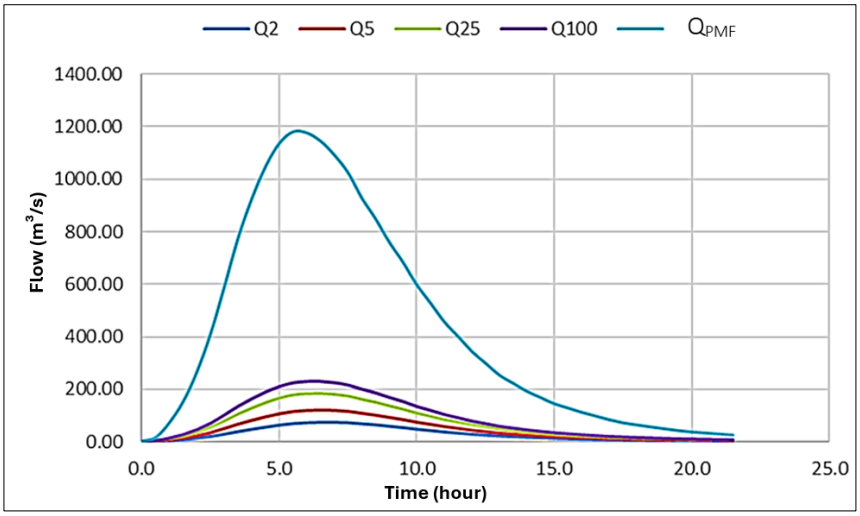

Figure 4.1. Updated flow hydrographs with different flood frequencies

The updated Q_{PMF} flood hydrograph has been routed through the spillway, and it has been observed that the spillway capacity is sufficient to pass the probable maximum flood. The difference between the inflow hydrograph and the outflow hydrograph illustrates the volume of water stored in the reservoir and how it is released over time. As depicted in Figure 4.2, during the probable maximum flood (PMF), the maximum storage volume, $V_{storage}$, was determined to be 6.07 hm³.

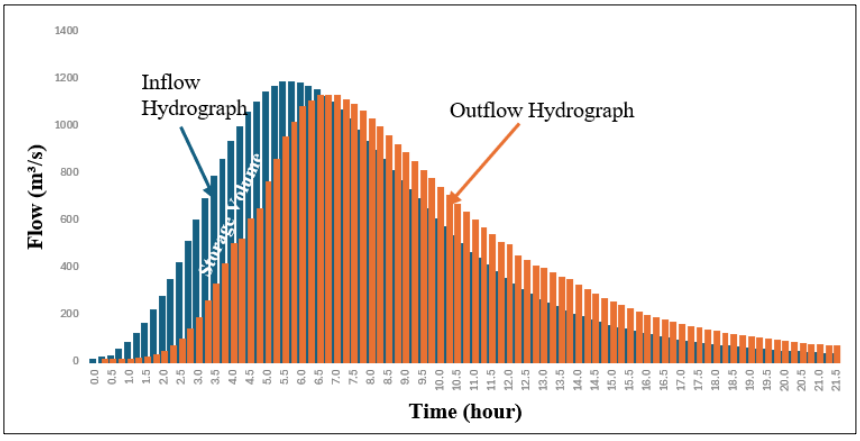

Figure 4.2 Comparison of spillway inflow and outflow hydrographs

4.2 Updating the Dam Operation Study Based on Current Rainfall Data

As mentioned in Section 3.3, due to Engiz DSI Station's outdated maximum precipitation data, missing data from 2010 to 2015 were obtained from the State Hydraulic Works (DSI) / Observations Department of the Directorate of Survey, Planning, and Allocations to revise the dam's reservoir operation study. This study identified specific seasons when water levels in the reservoir have risen, indicating potential overtopping risks.

As will be discussed extensively in later sections, the dam's crest elevation is 168.00 m, the maximum water level is 166.80 m, and the spillway crest elevation is 163.75 m. After the missing flow values were completed, the reservoir operation study was updated, and the reservoir water levels were recalculated monthly. The minimum freeboard is calculated as 3.04 m.

Based on the updated precipitation data, the normal water surface elevation in the reservoir is projected to be 164.96 meters, according to the latest reservoir operation calculations. At this elevation, the water volume in the reservoir is calculated to be 62.09 hm^3. The volume of the probable maximum flood (PMF) hydrograph is estimated to be 33.64 hm^3, Figure 4.1. During a PMF event, the maximum storage volume is calculated as 6.07 hm^3, Figure 4.2.

In case the PMF occurs when the reservoir is at the normal water surface of 164.96 meters, its total volume would reach 68.16 hm^3. This increase in volume would elevate the reservoir to 167.50 meters, as indicated by the elevation-volume-area curve. The insufficient remaining freeboard could potentially lead to an overtopping scenario at this elevation. Furthermore, with the expected changes in climate leading to more frequent high-intensity floods, overtopping in the future will become inevitable.

It should be noted that since changes cannot be made to the current operating conditions of the dam, the existing elevation levels and flood hydrographs from the approved report were used in the dam failure scenarios discussed in Chapter 5.

4.3 Investigation of the Possibility of Backward Erosion Piping Failure

The safety factor (FS) for backward erosion piping assesses whether the hydraulic pressure within the soil is sufficient to displace particles and initiate piping. This factor is calculated by comparing the critical hydraulic gradient with the existing one.

Steps for Calculating the Factor of Safety (FS) for Backward Erosion Piping:

Step 1: Calculate the Critical Gradient (i_c): The critical hydraulic gradient (i_c) is the minimum gradient that can cause particle displacement in the soil. It depends on soil properties and can be expressed by Equation (4.1), (Terzaghi and Peck, 1967).

$$i_c = \frac{\gamma_s - \gamma_w}{\gamma_w} \tag{4.1}$$

Where:

γ_s: Unit weight of soil particles (23 kN/m³ for bedrock taken from the Ondokuz Mayıs Dam body analysis report)

γ_w: Unit weight of water. (9.81 kN/m³)

i_c = 1.344

Step 2: Calculating the Existing Hydraulic Gradient (i) (Griffiths and Fenton, 1997): The existing gradient represents the slope of groundwater pressure within the soil and can be calculated as in Equation (4.2), (Terzaghi and Peck, 1967).

$$i = \frac{\Delta h}{L} \tag{4.2}$$

Where:

Δh: Difference in water level (hydraulic head) between the upstream and downstream,

L: Length of the flow path.

The existing hydraulic gradient (*i*) was calculated as 0.10 using advanced modeling techniques with the Slide2 Software (Rocscience, 2022). This calculation was based on the seepage analysis module of Slide 2, incorporating input parameters such as soil permeability (*k*), boundary conditions, and groundwater levels. The hydraulic gradient is derived by calculating the ratio of the hydraulic head difference to the flow path length. (Garai, 2016) In Slide 2, flow paths are delineated based on the geometry and material properties of the soil layers (such as soil type, porosity, density, and particularly soil permeability), allowing the software to determine the length of these paths accurately. Figure 4.3 illustrates the computational process, visually representing the flow paths and their respective lengths. The software allows a detailed factor of safety analysis by integrating these seepage effects into geotechnical stability assessments, thereby enhancing the accuracy and reliability of the results.

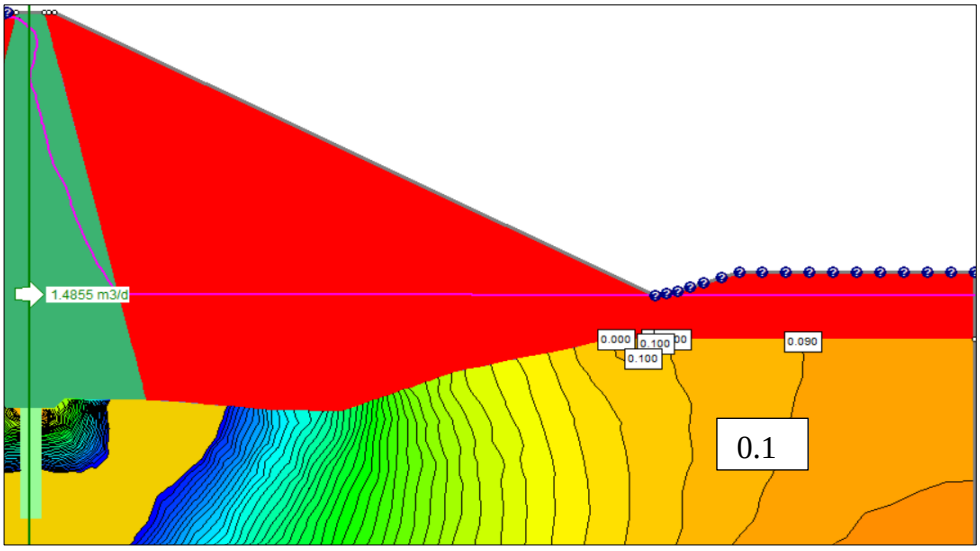

Figure 4.3 Calculation of existing hydraulic gradient (*i*) via Slide2 Software (Rocscience, 2022)

Step 3: Calculating the Factor of Safety (FS): The factor of safety is calculated as the ratio of the critical gradient to the existing gradient as in Equation (4.3), (Terzaghi & Peck, 1967).

$$FS = \frac{i_c}{i} \tag{4.3}$$

Investigators have recommended ranges for the factor of safety for escape gradient from 1.5 and 15, USACE EM 1110-2-1901 (US Army Corps of Engineers, 1986)

$$FS = \frac{1.344}{0.1} = 13.44 > 1.5$$

This indicates that the foundation is considered safe against backward erosion piping.

4.4 Calculation of Factor of Safety Against Heave Failure

Heave piping is a process in which water creates a backward flow within the soil. The pressure gradient transports soil particles to the surface, resulting in soil loss and reduced stability, especially in near-surface areas.

Steps for Calculating the Factor of Safety (FS) for Heave:

Step 1: Determination of the Upward Water Pressure (U) and Effective Stress

The Sigma/W module of Geostudio Software (Seequent, 2022) was used to determine the effective stress and pore water pressure beneath the dam, as illustrated in Figure 4.4 and Figure 4.5 The analysis was conducted using a finite element method (FEM) approach, incorporating input parameters such as soil properties (cohesion, friction angle, and permeability), groundwater conditions, and applied boundary constraints. Effective stress (σ') values were computed based on Terzaghi's principle, $(\sigma' = \sigma - u)$, where σ represents the total stress acting on the soil, and u denotes the pore water pressure. In this approach, total stress is influenced by the weight of overlying soil layers, while pore water pressure results from groundwater flow and saturation conditions. (Bowles, 1997)

Boundary conditions were defined based on the hydraulic state of the dam during operation. The upstream water level was set to the normal reservoir level at 163.75

m, representing steady-state conditions. The downstream boundary was defined to allow for free drainage, simulating natural seepage conditions. These boundary conditions influenced pore water pressure distribution within the dam body and its foundation, directly affecting the effective stress values.

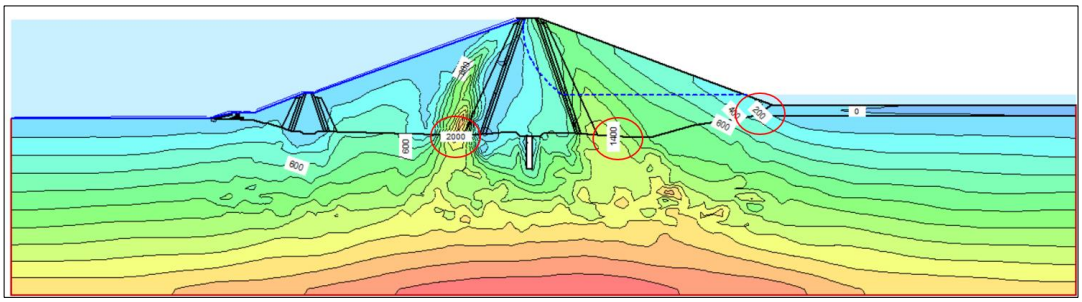

Figure 4.4 Effective stress distribution via Geostudio software

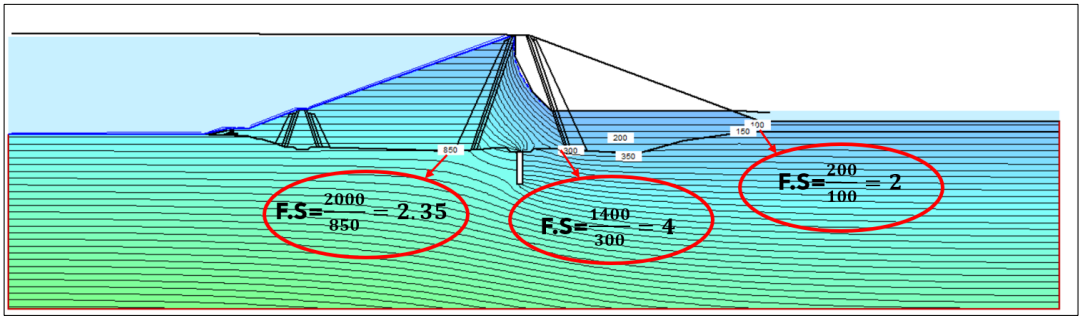

Figure 4.5 Pore water pressure distribution via Geostudio Software

Step 2: Calculation of Factor of Safety

The factor of safety against heaving can be given by (Das, 2010) as:

$$FS = \frac{W'}{U} \tag{4.4}$$

where *FS*=factor of safety

W'= submerged weight of soil, *U*=uplifting force caused by seepage.

F.S was suggested at least 1.5 (Budhu, 2015)

The factor of safety results show that the downward force is greater than the uplift force, so the dam body is safe and at least twice as strong.

4.4.1 Seepage Analysis of Ondokuz Mayıs Dam

Seepage analysis examines water flow within the dam body and foundation to assess potential seepage and erosion risks. This analysis helps identify areas where water needs to be controlled to ensure the long-term stability and safety of the dam. Additionally, seepage analysis enables the calculation of parameters such as the path and velocity of water flow through the soil, allowing the evaluation of the dam's factor of safety against seepage.

The seepage analysis of the Ondokuz Mayıs Dam was conducted using the Slide2 software, Figure 4.6. The seepage analysis of the maximum cross-section of the Ondokuz Mayıs Dam is illustrated with the permeability values of the materials used in the dam body obtained from the dam body analysis report approved by the Hydraulic State Work (DSI, 2013). Permeability values of dam materials are given in Table 4.1 below.

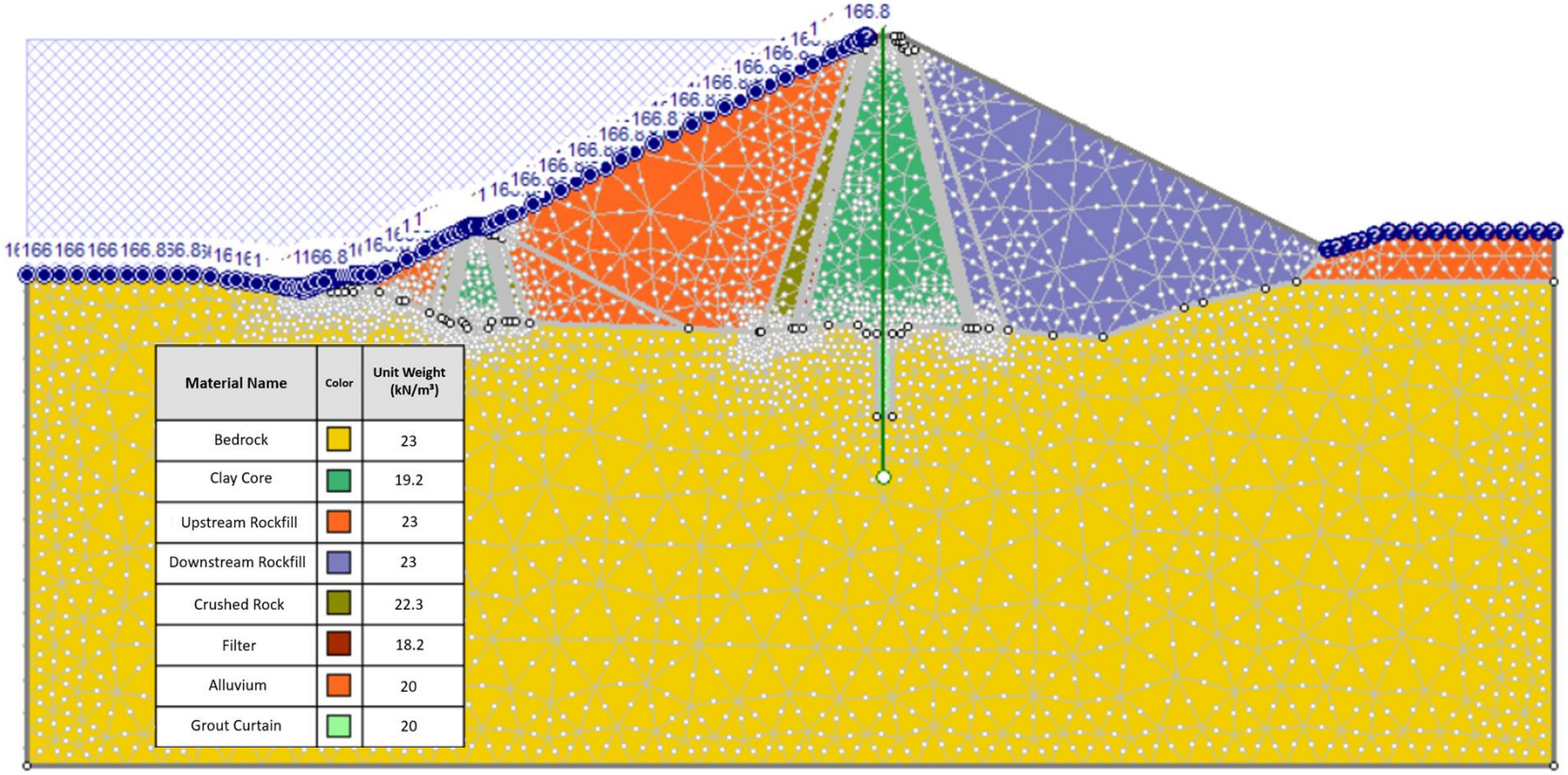

Figure 4.6 Slide2 Software (Rocscience, 2022) seepage analysis model screen

Table 4.1 Permeability parameters of seepage analysis (DSI, 2013)

Materials	**Permeability (k_x)**
Impervious Clay Core	k=1x10^{-8} m/s
Upstream Rockfill	k=1x10^{-2} m/s
Downstream Rockfill	k=1x10^{-3} m/s
Filter Zones	k=1x10^{-2} m/s
Foundation	k=1x10^{-6} m/s
Grout Curtain	k=1x10^{-10} m/s

Figure 4.7 shows the phreatic line within the clay core and the amount of seepage from the foundation due to the analysis conducted using Slide2 Software. The obtained seepage value was compared with the limits in the literature to assess the dam's safety.

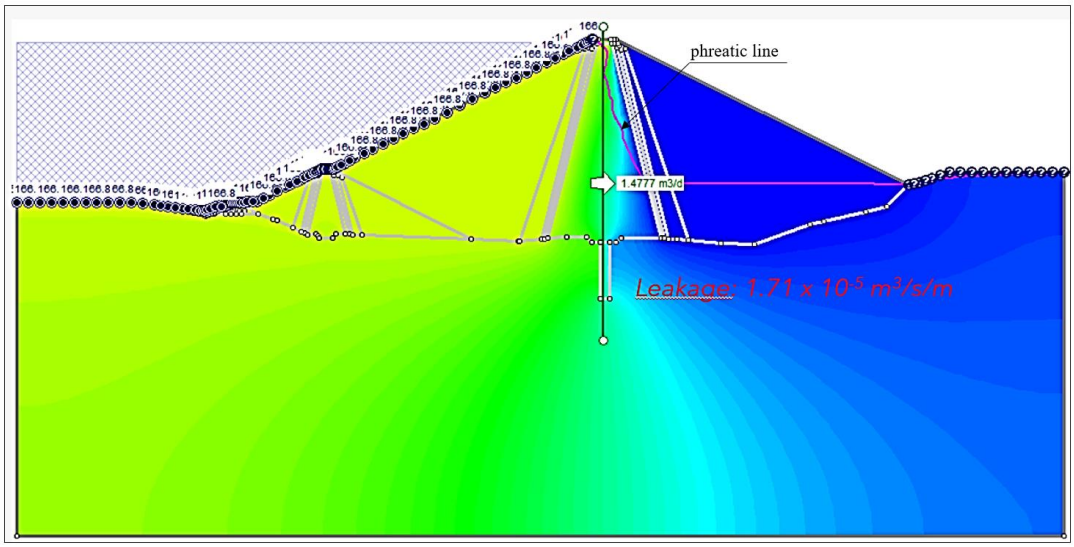

Figure 4.7 Results of seepage analysis of Ondokuz Mayıs Dam via Slide2 Software (Rocscience, 2022)

According to Soedibyo (1993), the maximum allowable seepage discharge, typically applied to earthfill dams (also known as embankment dams), is between 2% and 5% of the inflow. The annual average inflow at the Ondokuz Mayıs Dam site is 66.64

hm^3/year (2.14 m^3/s). Therefore, the maximum allowable discharge for the Ondokuz Mayıs Dam is 0.0428 m^3/s. Based on seepage analysis conducted using Slide2 Software, the highest seepage discharge is 1.71×10^{-5} $m^3/s/m$. This value is well below the maximum allowable discharge, indicating that the Ondokuz Mayıs Dam is safe from leakage hazards due to seepage.

4.5 Slope Stability Analysis of Ondokuz Mayıs Dam

An embankment dam requires a stable slope to prevent slope failure or landslides. Evaluating the safety factor under various conditions—such as during construction, at the end of construction, during operational cases, and in flood scenarios—is essential to assess potential slope instabilities. If the factor of safety against slope stability ($FS \leq 1.0$), the slope is considered unstable. Although many naturally stable slopes have safety factors below 1.0, due to the uncertainty in soil strength parameters and the exclusion of three-dimensional effects in the analysis, a slope is deemed safe and stable if it satisfies the minimum safety factor specified by some design guide.

The load conditions and safety factors included in the calculation for the slope stability analyses are specified below in Table 4.2. These safety factors were considered in the Ondokuz Mayıs Dam slope stability analysis results.

Table 4.2 Loading conditions and safety factors (DSI, 2014)

Condition	Safety Factor	Loading Condition
End of Construction	1.3	Unusual
End of Construction (OBE)	> 1.0	Extreme
Operational	1.5	Normal
Operational with Earthquake (OBE)	1.2	Unusual
Operational with Earthquake (MCE)	> 1.0	Extreme
Sudden Drawdown	1.2	Unusual

According to the dam body calculation report for the Ondokuz Mayıs Dam, the peak ground acceleration (PGA) with a 2,475-year return period and a 2% probability of exceedance over 50 years is 0.23g. For embankment dams, 50% of this PGA value has been applied. Typically, a reduction factor between 0.4 and 0.6 is used to adjust the PGA for embankment dams. This reduction factor accounts for damping effects in the analysis, providing a reasonable estimate of earthquake-induced forces, (Cetin, 2014).

The slope stability analysis of the Ondokuz Mayıs Dam was conducted using Slide2 Software (Rocscience, 2022). The strength parameters, including cohesion and internal friction angle, for the fill material were obtained from the Ondokuz Mayıs Dam Body Analysis Report and shown in Figure 4.8, (DSI, 2013).

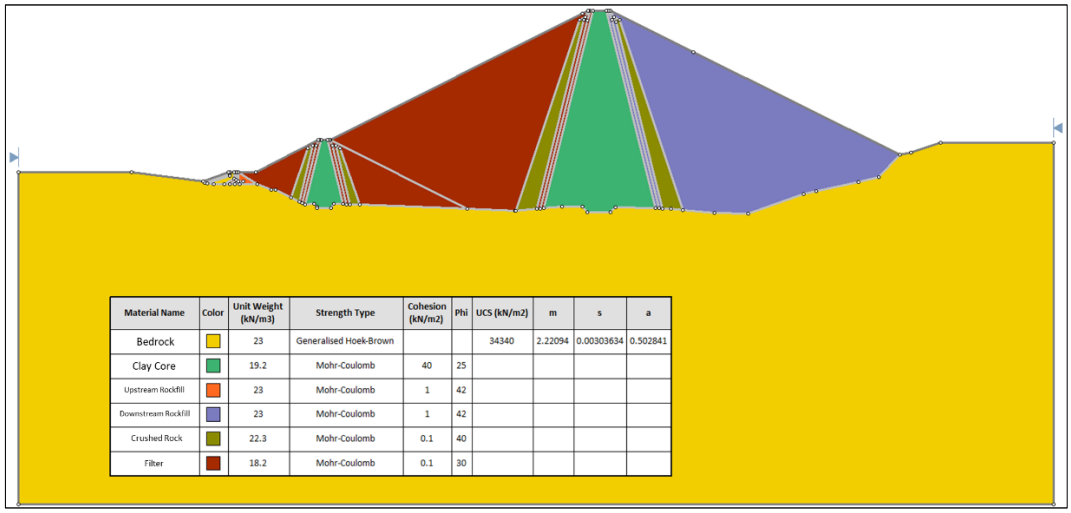

Figure 4.8 Geotechnical parameters of Ondokuz Mayıs Dam

In the dam body stability analysis report of the Ondokuz Mayıs Dam, the Mohr-Coulomb material model was selected as the material model for the fill materials, and for the foundation rock, the Generalized Hoek-Brown material model, a more general method used for evaluating the shear strength of rock masses, was applied.

Table 4.3 presents the Mohr-Coulomb parameters of the embankment fill materials under operational conditions, which are essential for evaluating the shear strength and stability of the dam body during its normal operating case.

Table 4.3 Mohr-Coloumb parameters of embankment fill materials for operational conditions (DSI, 2013).

Material	**γ (kN/m^3)**	**ϕ (degree)**	**C (cohesion) (kPa)**
Impervious clay core (1)	19.2	25	40
Rockfill Transition Zone(Ku)	22.3	40	-
Filter (Gravel, Sand)	18.2	30	-

Table 4.4 shows the Hoek-Brown parameters of the bedrock, which are used to assess the foundation rock's shear strength and ensure the dam's stability under different loading conditions.

Table 4.4 Hoek Brown parameters of bedrock (DSI, 2013)

Material	**γ (kN/m^3)**	**UCS (kN/m^2)**	***m***	***s***	***a***
Bedrock	23	34340	2.2094	0.00303634	0.502841

In the Hoek-Brown failure criterion (Hoek and Brown, 1980), the parameters ***m***, ***s***, and ***a*** are defined as follows: ***m*** is the material constant representing the rock mass's general strength. It accounts for the rock's overall strength properties and failure behavior, especially in the context of intact rock strength. ***s*** is related to the rock's shear strength. It plays a role in describing the rock’s resistance to shear stress and is essential for modeling the fracture and failure tendencies of the rock. ***a*** is the constant and represents the rock mass's behavior under compressive stresses. It is a critical parameter for understanding how the rock will fracture and deform under compression, (Hoek & Brown, 1980).

4.5.1 Limit Equilibrium Method

The Limit Equilibrium Method (LEM) is widely used for slope stability analysis. This method compares driving and resisting forces to evaluate whether a soil mass is in equilibrium concerning a potential slip surface. LEM is particularly effective for assessing the stability of large-scale engineering structures, such as dams and embankments.

Slide2 software offers multiple algorithms for Limit Equilibrium Method (LEM) analysis, including Bishop's Simplified, Janbu, Spencer, and Morgenstern-Price methods. In this study, the Morgenstern-Price approach was chosen because it can provide reliable results for slip surfaces of any shape and satisfy all equilibrium conditions, (Fell et al., 2005).

The Factor of Safety (*FS*) is the resisting and driving forces ratio, as shown in Equation (4.5). This equation is used to assess the stability of a slope, with a value greater than 1.0 indicating stability under the given conditions.

$$Factor\ of\ Safety = \frac{Resisting\ Forces}{Driving\ Forces} \tag{4.5}$$

The required safety factor and the minimum safety factor obtained for the dam's upstream and downstream slopes under different loading conditions as a result of the slope stability analysis are provided below in Table 4.5.

Table 4.5 The calculated safety factor of slope stability analysis of Ondokuz Mayıs Dam

Condition	Slope Face	Calculated Safety Factor	Required Safety Factor	Loading Condition
End of Construction	Upstream	1.792	1.3	Unusual
	Downstream	1.533		
End of Construction with Earthquake (OBE)	Upstream	1.591	> 1.0	Extreme
	Downstream	1.359		
Operational	Upstream	1.792	1.5	Normal
	Downstream	1.537		
Operational with Earthquake (OBE)	Upstream	1.463	1.2	Unusual
	Downstream	1.359		
Operational with Earthquake (MCE)	Upstream	1.176	> 1.0	Extreme
	Downstream	1.163		
Sudden Drawdown	Upstream	1.616	1.2	Unusual

The slope stability analysis results for upstream and downstream slopes in each loading condition are provided in Appendix C.

The analyses show that the most critical condition occurs on the downstream slope during the operational earthquake scenario, and the safety factor on the most critical slip surface is FS = 1.163 > 1.00, indicating that the slope is stable, Figure 4.9.

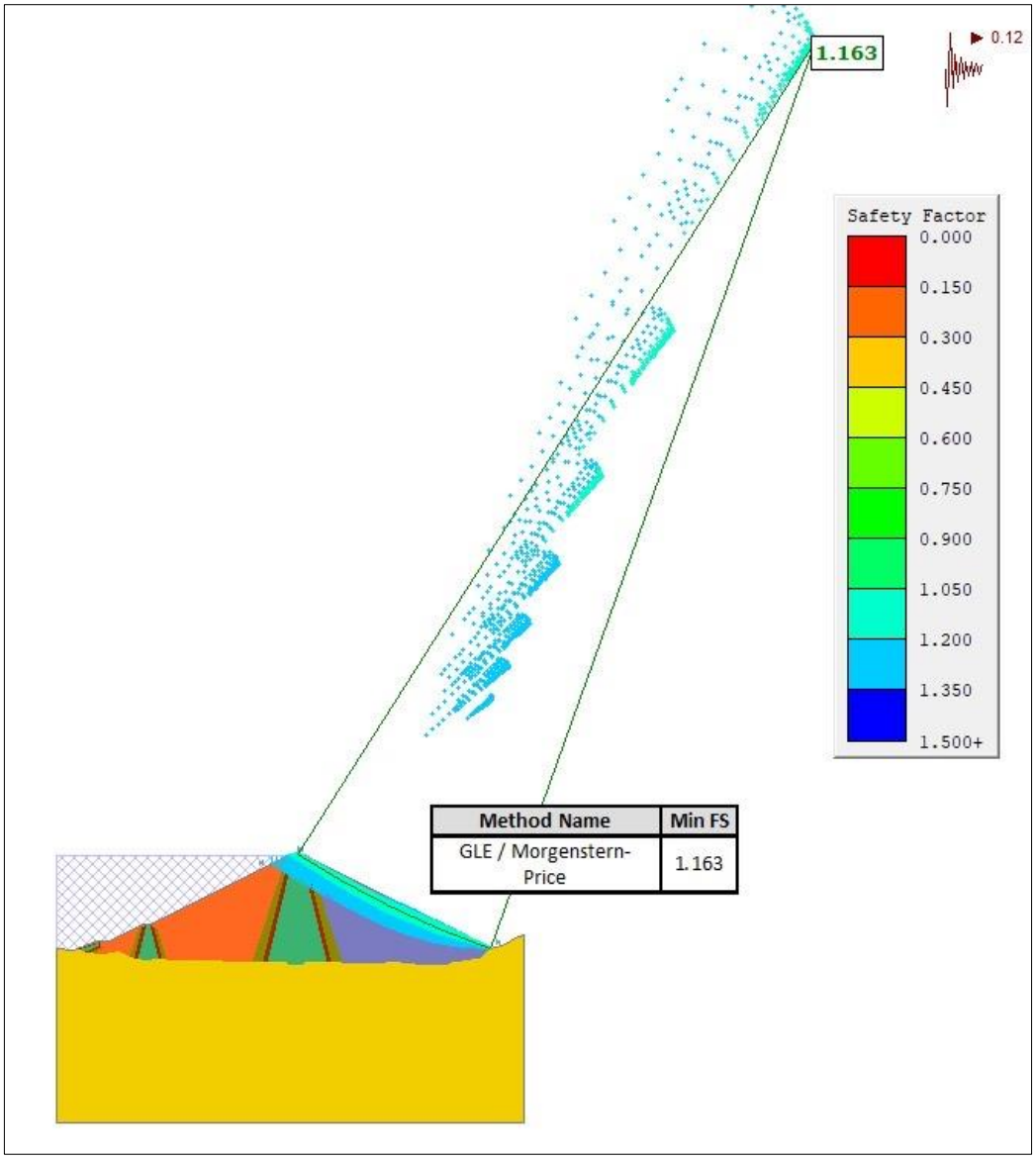

Figure 4.9 Ondokuz Mayıs Dam slope stability analysis in operational with earthquake case

4.6 A Specific Method To Mitigate Dam Slope Failure Risk

In this section, the objective is to determine a safer and more economical design option by considering the failure probability and costs of the dam body for different downstream slope configurations.

The current slope gradient of the dam is 2.0H/1.0V on both the upstream and downstream sides. In the operational earthquake case, as analyzed previously in Section 4.5.1, the minimum safety factor for the most critical slip circle on the downstream side was 1.163. However, suppose the strength parameters of clay and rock fill materials were to reduce in the future, leading to instability in the system. In that case, the improvement of the downstream slope of the dam can be evaluated in the long term.

In this context, a slope stability analysis was conducted for multiple slope configurations, where the downstream slope gradient was varied from 2.0H/1.0V to 2.6H/1.0V. Using Monte Carlo simulation within Slide 2 software, the probability of failure was calculated for each slope gradient. Additionally, a risk-based benefit analysis was performed by estimating the cost of failure and computing the benefit/cost ratio for each configuration. The primary aim of this analysis was to determine the optimal slope gradient that minimizes failure risk while maximizing economic viability.

4.6.1 Risk-Based Benefit Analysis

Risk-based benefit analysis is a method used to evaluate costs associated with a structure or system's failure probability. It aims to quantify the potential cost advantages between alternative designs. This analysis provides a cost-effective solution and enables a numerical evaluation of the benefits of a safer design option, (Baecher et al., 1980).

In this risk-based benefit analysis, the cost of the dam body for each slope was multiplied by the corresponding failure probability, providing an estimate of the potential losses (costs) if the dam were to fail. The relevant formulas are as follows:

$$\text{Risk Costs}=\text{Dam Cost} \times \text{Failure Probability} \quad (4.6)$$

The cost-benefit between two slopes is calculated by taking the difference between these risk costs by Equation (4.7), in which costs are to be explained in detail in Section 4.6.5

$$\text{Benefit} = (\text{Cost}_n \times \text{Failure Probability}_n)-(\text{Cost}_{n+1} \times \text{Failure Probability}_{n+1}) \quad (4.7)$$

In the formula, *n* represents a specific design scenario, while *n+1* refers to the subsequent design scenario.

4.6.2 Strength Reduction Factor (SRF) Analyses

In the above, Chapter 4, various failure probabilities of the dam were evaluated. The parameters used in these analyses were obtained from the literature or previous approved reports. Particularly in cases where the parameters carry uncertainty, the SRF method was used to interpret the risk and safety factors better. In this method, the strength parameters of clay and rock fill materials used in the dam body were gradually reduced to determine when the structure's shear resistance would become insufficient. When the SRF value reached a certain point, the shear strength along the slip surface diminished, and the system became unstable. This critical SRF value represents the shear safety factor of the dam body.

Several variations were created using the Monte Carlo method at this stage, and many simulations were run. In the 1000 simulations conducted, the strength properties of the dam body fill material (cohesion c and internal friction angle ϕ) were gradually reduced, and the probability distribution of these parameters (normal distribution) was determined. The probability of dam failure was found when the safety factor fell below 1.0 (FS<1.0), indicating that the slope had become unsafe.

4.6.3 Development of Monte Carlo Simulation Model to Calculate Probability of Slope Failure

Table 4.6 presents the input data for the Monte Carlo Simulation (MCS), showing the cohesion (c) and friction angle (ϕ) values for clay core and rockfill (upstream and downstream) materials. Each parameter is defined with minimum and maximum limits and varies according to a uniform distribution.

Table 4.6 Input data for Monte Carlo Simulation

Material Name	**Input parameters**	**Minimum**	**Maximum**	**Function**
Clay core	*c (kPa)*	30	50	Uniform
	ϕ (◦)	22	28	Uniform
Rockfill Downstream	*c (kPa)*	0	0	Uniform
	ϕ (◦)	31.5	42.5	Uniform
Rockfill Upstream	*c (kPa)*	0	0	Uniform
	ϕ (◦)	33	51	Uniform

Initial Analysis (Existing Slope: 2.0H/1.0V):

Figure 4.10 shows the statistical summary of FS obtained with the MCS model. The minimum and maximum FS are 0.66 and 1.79, respectively. The average value of FS was simulated as 1.194 due to the MCS model. The frequency of FS values falling below 1.0 indicates a critical stability condition.

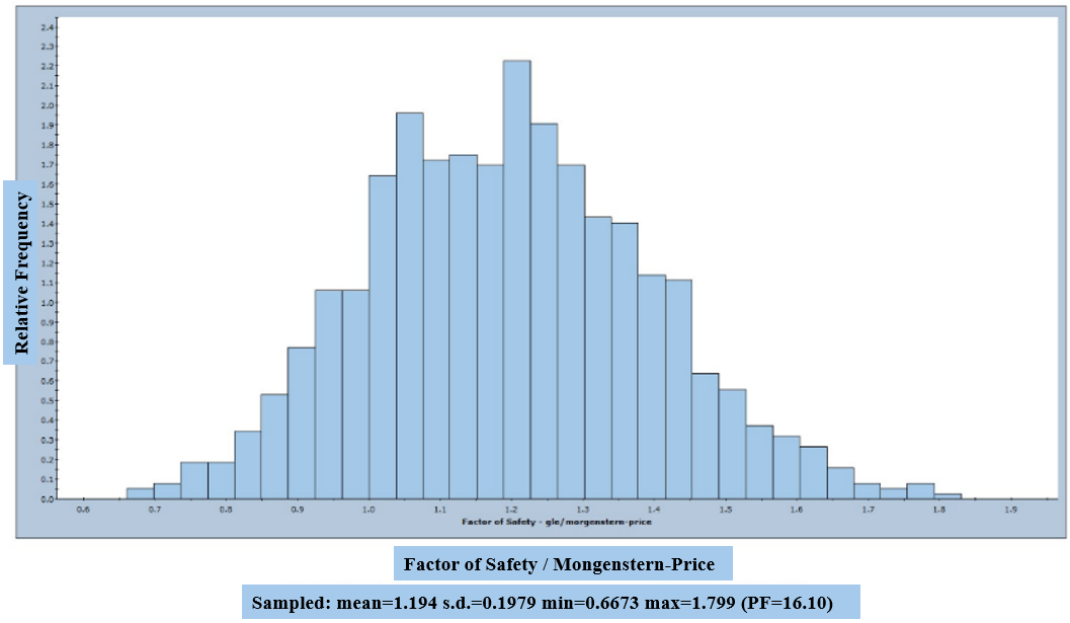

Figure 4.10 Distribution of FS for the existing slope, obtained by the MCS model

A total of 1000 simulations were conducted as part of the Monte Carlo analysis. Among these, 161 simulations failed, while 839 were deemed stable or safe. Consequently, the probability of failure (P_f) was calculated as:

$$Pf = \frac{Number\ of\ Failure}{Total\ Simulations} = \frac{161}{1000} = 0.161 \quad (4.8)$$

Thus, the probability of failure for the analyzed slope is 0.161 (Figure 4.11), corresponding to 16.1%. This indicates that the slope, in its current state, has a 16.1% of failure probability.

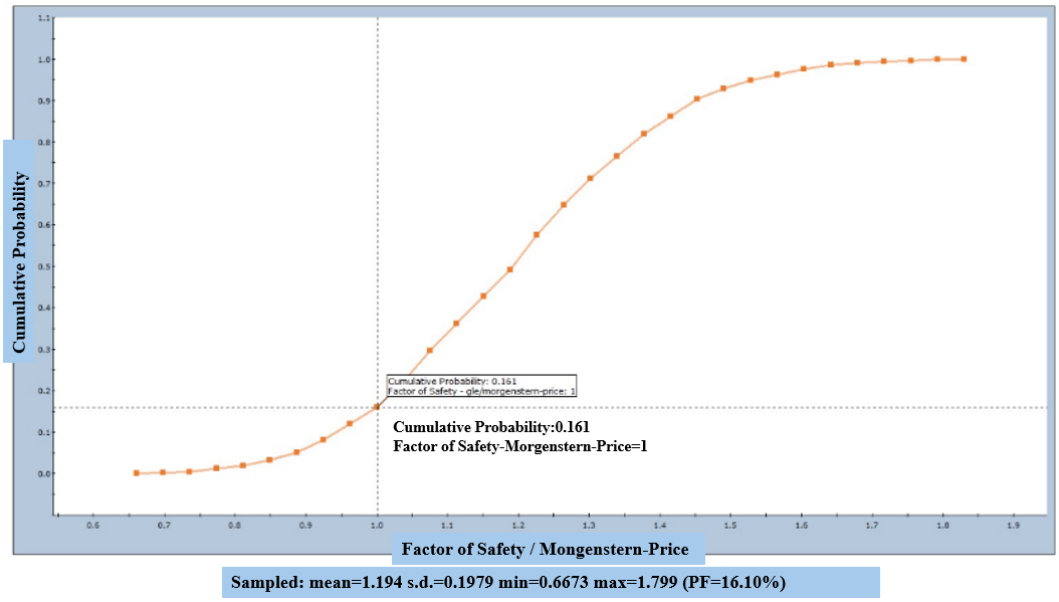

Figure 4.11 Probability of existing slope stability failure, obtained by the MCS model

Second Analysis (Proposed Slopes: 2.1H/1.0V~2.6H/1.0V):

As the downstream slope angle was gradually increased up to 2.6H/1V, a significant improvement in slope stability was observed. 1000 simulations were conducted as part of the Monte Carlo analysis. The probability of failure decreased consistently with flatter slopes, as shown in Table 4.7.

Table 4.7 The probability of failure for the proposed slopes, obtained by the MCS model

Proposed Dam Downstream Slopes	Probability of Failure (%)
2.0 H/1.0V	16.10
2.1 H/1.0V	14.70
2.2 H/1.0V	10.80
2.3 H/1.0V	8.20
2.4 H/1.0V	5.90
2.5 H/1.0V	3.40
2.6 H/1.0V	2.50

Reducing the slope angle from 2.0H/1.0V to 2.6H/1.0V enhances stability. The expected increase in FS and a significant reduction in P_f validate this design modification as a safer alternative. This adjustment improves the reliability of the structure and significantly reduces risks, as seen in Table 4.8.

Table 4.8 The safety factor of slope stability analysis for varied slope configurations of Ondokuz Mayıs Dam

Proposed Dam Downstream Slopes	**FS for Operational + Earthquake Case (MCE)**
2.0 H/1.0V	1.163
2.1 H/1.0V	1.221
2.2 H/1.0V	1.272
2.3 H/1.0V	1.320
2.4 H/1.0V	1.367
2.5 H/1.0V	1.414
2.6 H/1.0V	1.459

4.6.4 Calculation of Cost of Existing Slope Stability Failure

The measurements and material quantities for the existing dam were sourced from DSI-approved project reports. The areas of fill materials and their amounts estimated at the dam's maximum cross-section for the existing dam slope are given in Table 4.9.

Table 4.9 Materials and volumes in the existing dam slope (2.0H/1.0V)

The Existing Dam Slope (2.0H/1.0V)		
Material Name	**Area of Max. Section (m^2)**	**Volume (m^3)**
Impervious fill	2,764	643,000
Sand Filter material	377	93,603
Gravel Filter material	344	92,092
Rockfill	11,291	2,660,637
Transition Zone	10	4,520
Riprap	20	8,040
Rock Fragments	1,095	251,565

The areas and estimated volumes of rockfill material at the dam's maximum cross-section, after improving the downstream slope, are given in Table 4.10.

Table 4.10 Areas and estimated volumes of rockfill material in the slope varied from 2.0H/1.0V to 2.6H/1.0V.

Proposed Dam Downstream Slopes (Only the quantities of rockfill material have changed.)	**Total Area of Max. Section (m^2)**	**Volume (m^3)**
Rockfill (2.0H/1.0V)	11,291	2,660,637
Rockfill (2.1H/1.0V)	11,577	2,728,076
Rockfill (2.2H/1.0V)	11,852	2,793,000
Rockfill (2.3H/1.0V)	12,116	2,855,207
Rockfill (2.4H/1.0V)	12,368	2,914,539
Rockfill (2.5H/1.0V)	12,608	2,971,121
Rockfill (2.6H/1.0V)	12,984	3,059,749

Table 4.11 presents the cost breakdown for the existing dam body and cofferdam, according to the 2024 unit prices provided by DSI.

Table 4.11 Dam body and cofferdam cost breakdown/Existing Dam Slope - 2024 DSI unit prices

Samsun Ondokuz Mayıs Dam					
Clay Core Rockfill Dam					
Dam Body and Cofferdam Cost Breakdown (2024) DSI Unit Prices					
Pos. No.	**Description of Work**	**Unit**	**Quantity**	**Unit price TRY**	**Total TRY**
	Dam Body and Cofferdam Excavation				
B-15.330	Foundation excavation	m^3	385,000	238.86	91,960,628
B-07.D/5	Hauling of rock material (f = 2.65 km)	m^3	385,000	46.85	18,035,370
	Dam Body and Cofferdam Excavations Total				**109,995,998**
	Impervious- Filter Material				
B-15.302	Impervious fill	m^3	616,700	59.11	36,453,137
B-15.D/1	Impervious fill (cofferdam)	m^3	26,300	178.40	4,691,920
B-15.342	Raw filter material	m^3	4,520	56.29	254,431
B-15.343	Screened filter material	m^3	188,402	291.08	54,840,054

Table 4.11 Existing dam body and cofferdam cost breakdown - 2024 DSI unit prices (Continued)

B-14.018	Compaction of embankment or dam embankment with mechanical hammer	m³	40,481	310.00	12,549,141
B-15.054	Sheep's foot roller compaction	hour	6,167	1,577.04	9,725,606
B-15.344	Washing of filter material	m³	188,402	19.99	3,766,156
B-15.321	Watering of sheep's foot roller fill	m³	61,670	58.96	3,636,063
B-15.322	Watering of rock/sheep's foot roller/Harrow fill	m³	9,646	40.68	392,403
B-15.052/A	Vibratory cylinder compaction	hour	1,286	1,510.03	1,942,120
B-07.D/3	Hauling of filter material (f = 60.0 km)	m³	188,402	225.40	42,465,811
B-07.D/4	Hauling of filter material (f = 60.0 km)	m³	4,520	202.86	916,927
B-07.D/3	Hauling of impervious material (f = 1.48 km)	m³	450,000	26.93	12,118,292
B-07.D/3	Hauling of impervious material (f = 2.68 km)	m³	193,000	36.20	6,987,426
	Impervious-Filter Material Total				**190,739,488**
	Rockfill				
Pos. No.	**Description of Work**	**Unit**	**Quantity**	**Unit price TRY**	**Total TRY**
B-15.312	Rockfill from quarry	m³	3,044,565	199.15	577,319,121
B-15.323	Pressure watering of rockfill	m³	913,370	37.89	32,951,978
B-15.052/B	Vibratory cylinder compaction	hour	12,178	2,222.93	25,776,349
B-15.348	Riprap from quarry rock	m³	8,040	369.13	2,967,805
B-07.D/3	Hauling of rockfill material (f = 1.48 km)	m³	259,605	26.93	6,991,043
B-07.D/3	Hauling of rockfill material (f = 1.03 km)	m³	2,793,000	22.41	59,329,611
	Rockfill Total				**705,355,908**
	Estimated Cost				**1,006,071,393**

Based on the updated volume of the rockfill material, the cost breakdown for the different downstream slope configurations is provided in Table 4.12 As expected, the total cost of the Ondokuz Mayıs Dam has increased due to the increased volume of rockfill material for different downstream slope configurations.

Table 4.12 Cost Breakdown for different downstream slope configurations

Proposed Dam Downstream Slopes	Cost Breakdown (2024)
2.0 H/1.0V	1,006,071,393
2.1 H/1.0V	1,027,428,905
2.2 H/1.0V	1,041,292,184
2.3 H/1.0V	1,061,208,693
2.4 H/1.0V	1,072,902,124
2.5 H/1.0V	1,091,257,687
2.6 H/1.0V	1,105,797,577

The data presented in Table 4.7 and Table 4.12 were used for the cost-effectiveness analysis of various downstream slope values, which was conducted to determine the most suitable downstream slope. According to the analysis, while the investment cost increases from 2.0 H/1.0V to 2.6 H/1.0V, the probability of failure decreases. This indicates that structural improvements contribute to risk reduction. Additionally, the cost of failure follows a generally decreasing trend.

4.6.5 Calculation of Expected Value

Baecher et al.'s (1980) study states, "To determine risk costs, the probability of failure and its consequences must be calculated using the expected value approach." This explains that the total cost of a failure event is derived by multiplying the likelihood of the failure occurring by the magnitude of its consequences. The comparison between different slope designs clearly illustrates the relationship between safety measures and economic benefits.

In section 4.6.4 the cost of the existing slope design (2.0H:1.0V) was calculated as 1,006,071,393 TRY, with a failure probability of $P_0 = 0.161$. As the downstream slope gradient increased incrementally from 2.0H:1.0V to 2.6H:1.0V, the associated costs rose accordingly. However, the probability of failure showed a decreasing trend, reaching $P_6 = 0.025$ at 2.6H:1.0V.

The net benefit for each alternative slope configuration was calculated using the expected value approach, considering both failure probability and cost. The benefit-cost analysis highlights that while gentler slopes require higher initial costs, they also significantly reduce failure risks, leading to long-term economic advantages.

For example, when transitioning from 2.0H:1.0V to 2.6H:1.0V, the probability of failure decreases from 0.161 to 0.025, while the cost increases from 1,006,071,393 TRY to 1,105,797,577 TRY. The expected benefit is calculated as:

$$Benefit = Prob.of\ Failure_n * Cost\ of\ Failure\ _n - Prob.of\ Failure_{n+1} * Cost\ of\ Failure\ _{n+1}$$

$$Benefit = 0.161 * 1{,}006{,}071{,}393\ - 0.025 * 1{,}105{,}797{,}577 =\ 134{,}332{,}554\ \text{TRY}$$

In Table 4.13, the cost of failure and net benefits for each slope gradient are calculated. The most significant benefit increase is observed in the transition from 2.1 H/1.0V to 2.2 H/1.0V, where the benefit-to-total cost ratio is recorded at 0.033. This value represents the highest benefit-to-total cost ratio compared to other slope gradients.

Table 4.13 Cost-benefit analysis of downstream slope configurations for Ondokuz Mayıs Dam

1	2	3	4 = (2)x(3)	5 =Δ (4)	6 = (2)+(4)	7 = (5) : (6)
Downstream Slope	**Investment Cost (2024) (TRY)**	**Probability of Failure**	**Cost of Failure (TRY)**	**Benefit (TRY)**	**Total Cost (TRY)**	**Benefit/Total Cost Ratio**
2.0 H/1V	1,006,071,393	0.161	161,977,494	-	1,168,048,888	-
2.1 H/1V	1,027,428,905	0.147	151,032,049	10,945,445	1,178,460,955	0.009
2.2 H/1V	1,041,292,184	0.108	112,459,556	38,572,493	1,153,751,740	0.033
2.3 H/1V	1,061,208,693	0.082	87,019,113	25,440,443	1,148,227,806	0.022
2.4 H/1V	1,072,902,124	0.059	63,301,225	23,717,887	1,136,203,350	0.021
2.5 H/1V	1,091,257,686	0.034	37,102,761	26,198,464	1,128,360,448	0.023
2.6 H/1V	1,105,797,577	0.025	27,644,939	9,457,822	1,133,442,517	0.008

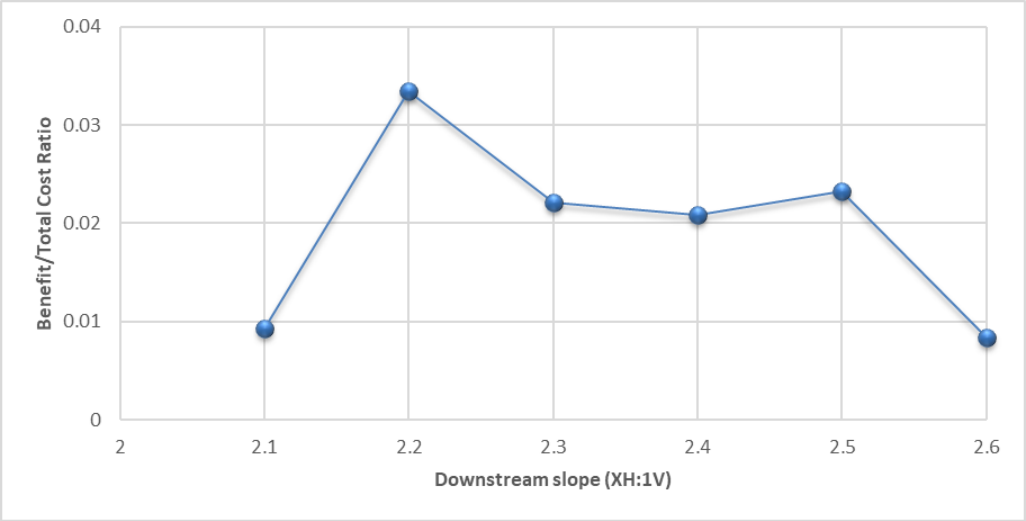

Figure 4.12 Benefit/Total Cost ratio variation in different downstream slopes

As seen in Figure 4.12, this analysis identifies the 2.2 H/1.0V slope as a strategic point where the return on investment and dam safety are optimally ensured in the long term. The total benefit/cost ratio (7) is highest at the 2.2 H/1.0V slope, indicating that further increases in slope reduce cost-effectiveness. Therefore, the 2.2 H/1.0V slope has been identified as a strategic point where the return on investment is maximized, making it the optimal choice for long-term dam safety. Implementing the 2.2 H/1.0V slope configuration, based on this study, suggests that it could be the most cost-effective and safest setup for the Ondokuz Mayıs Dam.

This result demonstrates that investing in a more stable slope configuration reduces failure risks and provides economic benefits over the long term. The expected value method effectively quantifies the financial implications of different failure scenarios, assisting decision-makers in selecting the most cost-effective and resilient design.

4.6.6 Conclusions and Future Works for Considering Other Improvements

Developing strategic approaches to enhance dam safety is of significant technical and economic importance. In the above section, only one method—downstream slope stability improvement—was examined for dam safety, demonstrating that a slight increase in the downstream slope inclination reduces the risk of failure and provides economic benefits.

Other methods that can be incorporated to reduce dam failure risks and provide economic benefits include:

Improvement of Filter Systems in the Dam Body: Enhancing the filter materials and drainage systems used in the dam body can prevent uncontrolled seepage and reduce erosion risk. This method can also lower maintenance and repair costs in the long term.

Optimization of Seepage Control Systems: Methods such as cutoff walls, bentonite barriers, or jet grouting can be used for seepage control. Alternatively, if an existing system is in place, the lengths of cutoff walls can be extended. Additionally, foundation reinforcement or fill improvements can be implemented at the base of the dam.

Increasing the Downstream Slope Inclination: As previously stated in Section 4.6, increasing the downstream slope inclination has reduced the probability of failure and improved the dam's overall stability. Additionally, adjusting the upstream slope inclination could also be considered an alternative improvement measure.

Implementation of Early Warning and Monitoring Systems: Sensor-based early warning systems that monitor groundwater pressure, deformation, and seismic activity can be installed in dams to reduce the risk of failure. These systems provide an opportunity for early intervention in the event of potential danger and help prevent economic losses.

Implementation of Proper Operation and Maintenance Policies: Regular maintenance and inspections of dams enable the early detection of potential problems. Improving operational efficiency plays a fundamental role in risk reduction strategies.

CHAPTER 5

IN-DEPTH EXPLORATION OF KEY ISSUES

5.1 Determination of Key Issues Affecting Breach Analysis Results

This section explores key issues in depth, including breach parameters, hydrodynamic model grid structures, breach prediction techniques, numerical solution methods of hydrodynamic models, and their impact on flooding caused by dam failures. By carefully examining these factors, the study intends to deepen the understanding of the complex interactions that influence different flood behaviors and their consequences. Furthermore, it includes a detailed evaluation of the economic damages from selected critical failure scenarios. It offers insights to inform effective risk management and flood mitigation strategies in dam safety.

5.1.1 Investigation of the Effects of Dam Breach Parameters

In the dam-break analysis, various parameters such as breach width, breach formation time, and breach slope angle vary depending on the construction material (type) of the dam and factors such as the design and structural integrity of the dam, the hydrological conditions, and the specific characteristics of the surrounding environment. However, the selection of these parameters often carries uncertainty. For this purpose, the effects of the parameters on the outflow hydrographs resulting from the breach have been investigated within the thesis.

To determine which parameters have a more dominant effect on the maximum outflow from the breach, the Aeronautical Reconnaissance Coverage Geographic Information System (ArcGIS) and the Hydraulic Engineering Center River Analysis

System (HEC-RAS) software were used to analyze the impact of dam breaches and conduct sensitivity assessments. HEC-RAS was selected for its ability to simulate dynamic flood scenarios and its user-friendly interface. Additionally, HEC-RAS is a program that integrates well with ArcGIS software.

The sensitivity analysis was performed by systematically altering each breach parameter individually while keeping all other parameters constant. This allowed for a detailed examination of how variations in the breach formation time (T_f), side slope (S), and breach width (W) influenced the outflow hydrograph. The results showed distinct changes in peak discharge and the time to reach peak discharge, with different combinations of parameters leading to variations in the flood wave dynamics. The analysis helped to identify the most sensitive parameters affecting flood characteristics, providing valuable insights for flood modeling and risk assessment.

In this context, W represents the average breach width (in meters), T_p is the time to reach peak discharge (in hours), HD is the height of the dam (in meters), T_f is the breach formation time (in hours), and S denotes the side slope of the breach (XH/1V). These parameters were analyzed to evaluate their influence on the flood hydrograph behavior and the corresponding variations in peak discharge, Figure 5.1.

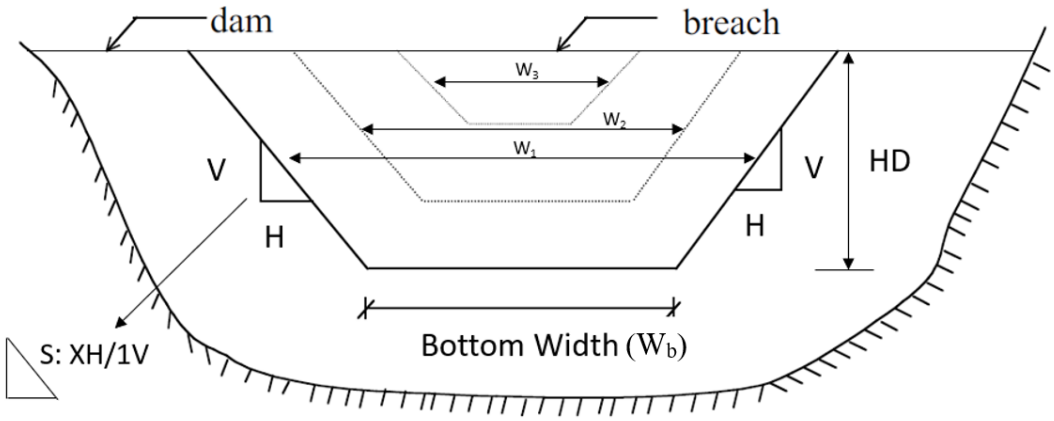

Figure 5.1 Description of the breach parameters (adapted from Bozkuş & Güner, 2001, with modifications)

In dam breach modeling, the trapezoidal geometry is commonly assumed to represent the breach shape, especially for embankment dams. This assumption simplifies the calculation of the breach development and the resulting outflow characteristics, (Wahl, 2004). An overtopping breach starts from the crest level. In contrast, a piping breach initially appears as a point at the centerline station and elevation specified by the user, with a rectangular opening. By default, the breach growth is assumed to be linear from start to maximum size, (USACE, 2014). It is assumed that the eventual shape of a fully developed breach, whether from piping or overtopping, could indeed take on a trapezoidal form, particularly as erosion widens the breach and affects larger embankment sections.

The breach outflow hydrographs were generated for each scenario, allowing a comparative analysis of flood behavior. Combining the three main scenarios and their six sub-scenarios each, 18 scenarios were analyzed, Table 5.1. This structured approach allows for a detailed sensitivity analysis of the parameters and their role in determining the hydrodynamic response during a dam breach event;

Main Scenario 1:

Tf = 0.5 hours, *S*: 1.0H/1.0V ~ 0.5H/1.0V, *W* = 2 *HD.*

This scenario focuses on a short breach formation time with steepening slopes and a large breach width (double the dam height).

Six sub-scenarios were analyzed by varying the breach side slope values from *S* = 1.0H/1.0V to 0.5H/1.0V.

Main Scenario 2:

Tf = 1 hour, *S*: 1.0H/1.0V ~ 0.5H/1.0V, *W* = 2 *HD.*

This scenario extends the breach formation time while keeping the breach width constant at 2 *HD*.

Different side slope values created six sub-scenarios between *S* = 1.0H/1.0V to 0.5H/1.0V.

Main Scenario 3:

Tf = 1 hour, *S*: 1H/1V ~ 0.5H/1.0V, *W* = 1.5 HD.

Here, the breach width was reduced to 1.5 *HD* with a constant breach formation time of 1 hour.

Six sub-scenarios were generated by adjusting the breach side slope values from *S* = 1.0H/1.0V to 0.5H/1.0V.

Table 5.1 Variation of peak breach outflow with different breach parameters

Scenario No	Physical Models (Federal Agency Guidelines)	Breach Bottom Width (m) *(W)*	Side Slopes (*S*=H:1.0V)	Breach Development Time (hr) *Tf*	Peak Breach Outflow (m^3/s)	Difference ΔQ (m^3/s)
Main-1	Estimation-1	167.78 (2x*HD*)	1	0.5	93456.53	
	Estimation-2	167.78 (2x*HD*)	0.9	0.5	91256.73	-2199.8
	Estimation-3	167.78 (2x*HD*)	0.8	0.5	89056.19	-4400.34
	Estimation-4	167.78 (2x*HD*)	0.7	0.5	86326.87	-7129.66
	Estimation-5	167.78 (2x*HD*)	0.6	0.5	84015.29	-9441.24
	Estimation-6	167.78 (2x*HD*)	0.5	0.5	81919.96	-11536.57
Main-2	Estimation-7	167.78 (2x*HD*)	1	1	55982.04	
	Estimation-8	167.78 (2x*HD*)	0.9	1	56800.88	818.84
	Estimation-9	167.78 (2x*HD*)	0.8	1	56960.84	978.8
	Estimation-10	167.78 (2x*HD*)	0.7	1	55650.02	-332.02
	Estimation-11	167.78 (2x*HD*)	0.6	1	56085.87	103.83
	Estimation-12	167.78 (2x*HD*)	0.5	1	55791.95	-190.09
Main-3	Estimation-13	112 (1.5x*HD*)	1	1	38288.06	
	Estimation-14	112 (1.5x*HD*)	0.9	1	37516.32	-771.74
	Estimation-15	112 (1.5x*HD*)	0.8	1	37583.84	-704.22
	Estimation-16	112 (1.5x*HD*)	0.7	1	36596.39	-1691.67
	Estimation-17	112 (1.5x*HD*)	0.6	1	36572.01	-1716.05
	Estimation-18	112 (1.5x*HD*)	0.5	1	35468.02	-2820.04

The sensitivity analysis showed that increasing the breach width raises the maximum discharge value while reducing T_p. Conversely, decreasing the breach width resulted in the opposite effect. As shown in Figure 5.2, when the breach width (W) increases from 1.5 *HD* to 2 *HD* corresponds to a 34% increase, the peak discharge (Q_p) rises from 40,000 m³/s to 60,000 m³/s, resulting in a 50% increase. Simultaneously, the time to peak (T_p) decreases from 6 hours to 3 hours, corresponding to a 50% reduction.

Furthermore, no apparent change was observed in the time to reach peak discharge (T_p) or the peak discharge magnitude (Q_p) with modifications to the breach side slope (S). Specifically, reducing the side slope from *S*:1.0H/1.0V to *S*:0.5H/1.0V (a 50% reduction) resulted in minor variations: the time to peak decreased from 6.0 hours to 5.7 hours (a 5% reduction), while the peak discharge decreased from 40,000 m³/s to 38,000 m³/s (a 5% decrease). Although these changes can be measured, they are quite small when compared to the significant effects caused by changes in breach width. Therefore, the influence of the breach side slope on the Ondokuz Mayıs Dam appears to be limited.

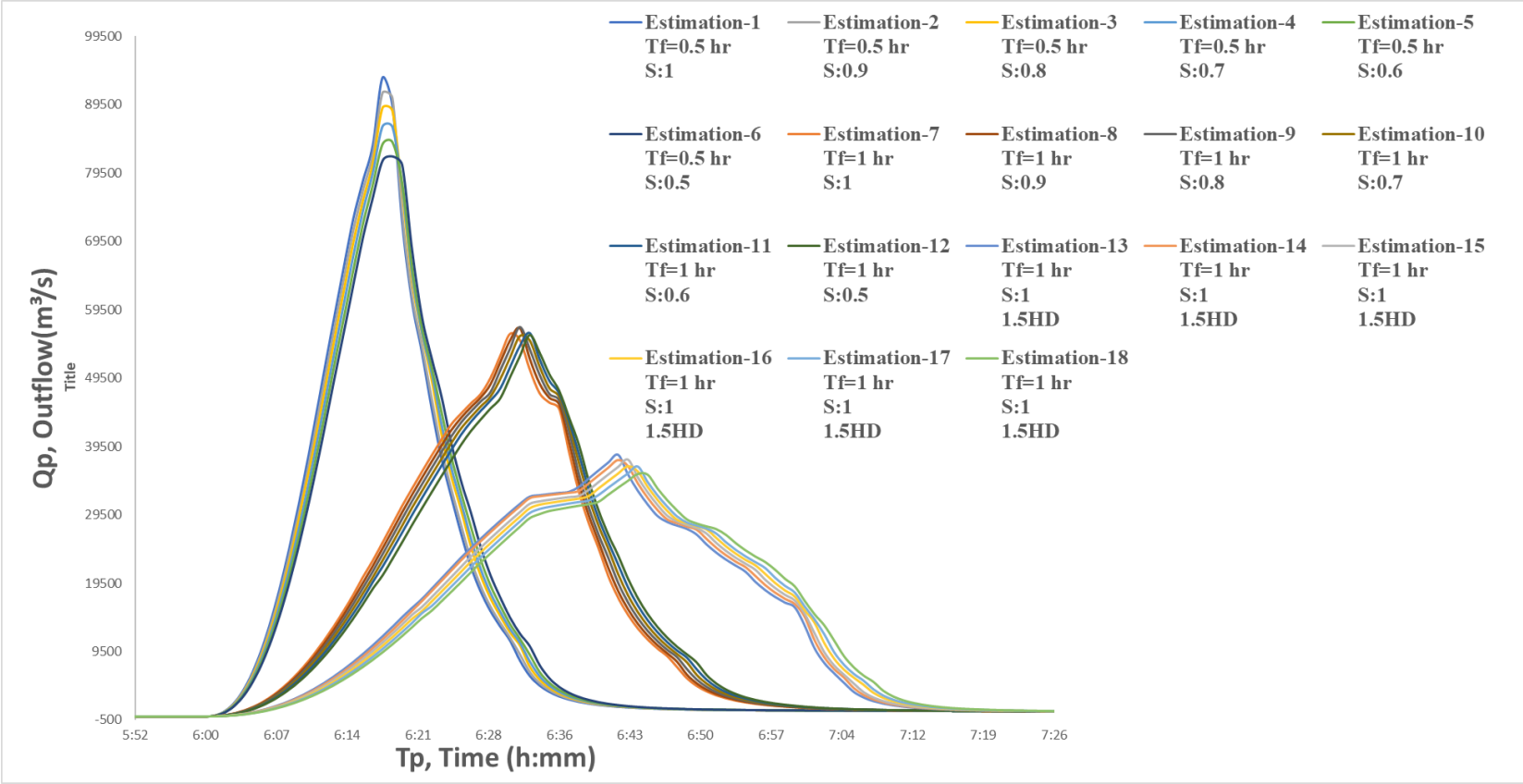

Figure 5.2 The impact of side slope, failure time, and breach width on the flood hydrograph resulting from a dam breach in the overtopping failure.

Figure 5.3, shows the change in peak flow concerning the breach side slope (%) graph, which was prepared to illustrate the percentage change in peak discharge values caused by variations in breach side slopes**.** The graph includes three main scenarios and their corresponding 18 sub-scenarios**.** These sub-scenarios display the percentage changes in Tp (time to peak discharge) and peak discharge resulting from changes in breach side slopes. The curves indicate that as the breach side slopes decrease (e.g., from 1.0H/1.0V to 0.5H/1.0V), the peak discharge also decreases, demonstrating the influence of side slopes on flood discharge.

In cases of shorter failure times (30 minutes, W=2HD), the impact of side slopes is more pronounced, as the peak flow decreases significantly with steeper slopes. In contrast, for longer failure times (60 minutes, W=2HD), the effect is minimal, with only slight variations in peak flow. The effect becomes moderate for narrower breach widths (60 minutes, W=1.5HD), showing a more noticeable decrease in peak flow.

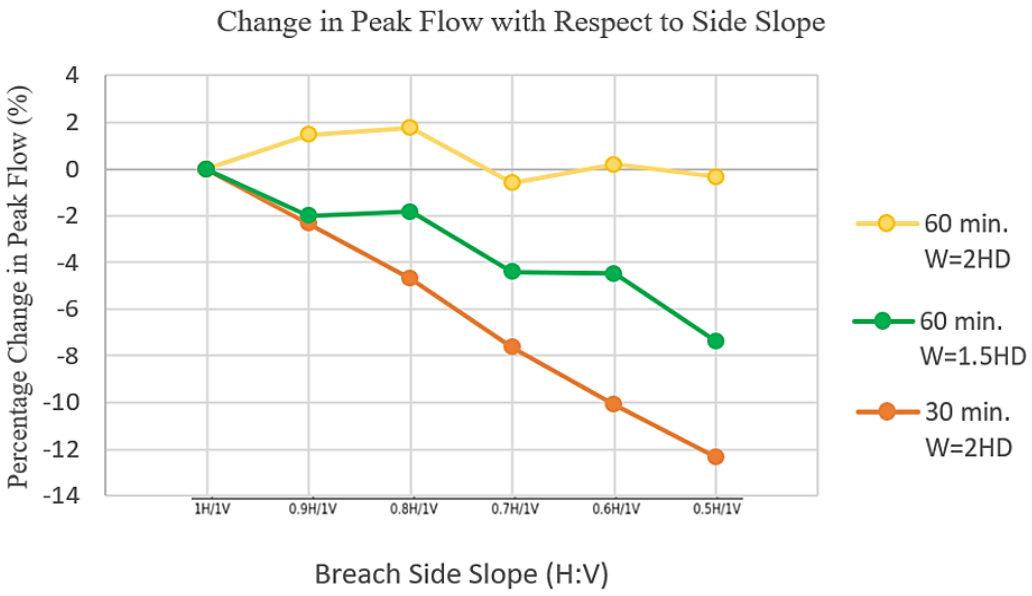

Figure 5.3 Change in peak flow concerning varying breach side slopes

In summary, the study findings show that the breach formation time significantly affects maximum discharge (Q_p) and the time to reach peak discharge (T_p). When the breach formation time increased from 0.50 hours to 1 hour (an increase of 100 %),

Q_p decreased from 93,456.53 m³/s to 55,982.04 m³/s, corresponding to a reduction of 46.83%.

5.1.2 Sensitivity Analysis of Model Grid Sizes

Under the same breach scenario (using the same breach parameters), flood inundation maps of models with different mesh grid sizes were compared, and data from 1000 randomly selected points were analyzed using various statistical methods. The study examined the sensitivity of mesh size across five different grid configurations: 50 × 50 m, 25 × 25 m, 10 × 10 m, 7.5 × 7.5 m, and 6.0 × 6.0 m, aiming to determine the most suitable representation of topography while maintaining optimal computational efficiency. The maximum water depth maps obtained from the analysis for each grid size are provided in Appendix A.

To investigate the impact of different grid sizes on dam break analysis, a set of 1000 randomly generated points was created on the flood map using Geographic Information System (GIS) software. The water depths resulting from flooding were recorded at these 1000 points for various grid sizes, and a sensitivity analysis was conducted among the values obtained. Below, the 1000 randomly generated points are shown in Figure 5.4.

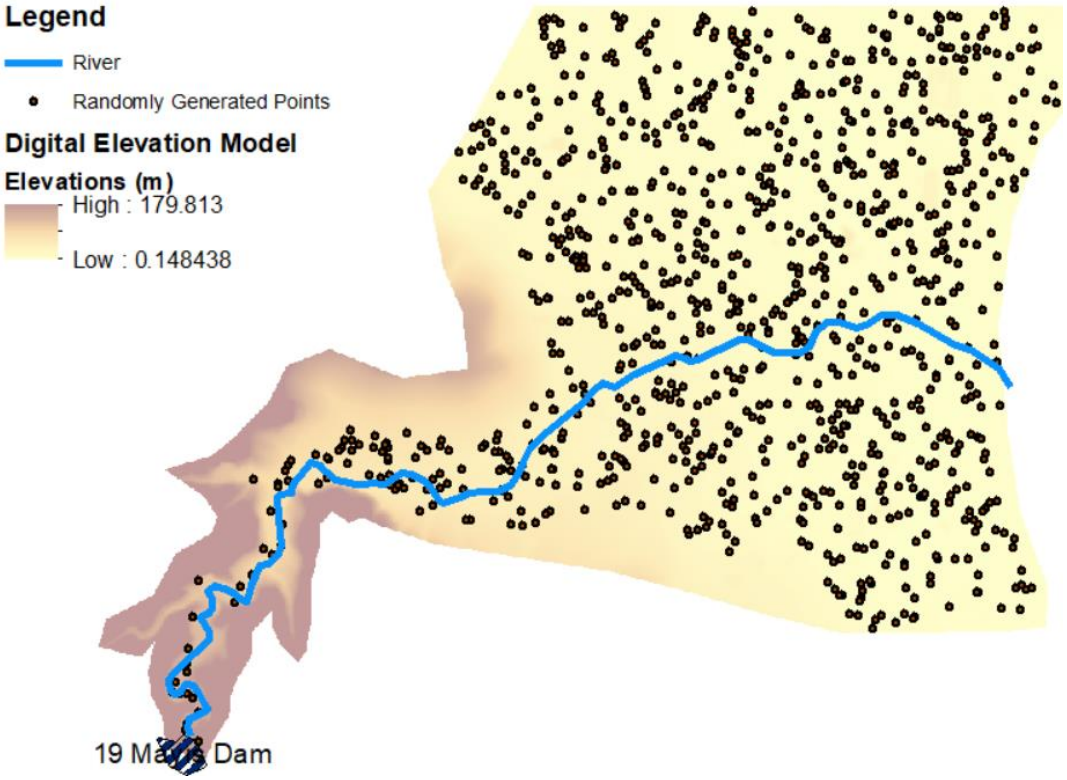

Figure 5.4 1000 randomly distributed points on the DEM model.

Table 5.2 shows that larger mesh sizes lead to a slight decrease in water depth values. However, the statistical analysis conducted in this study indicates that these changes do not significantly impact the water depth. The R^2 and RMSE values were calculated using the 6x6 m grid size as the flow depth reference (base model).

Table 5.2 Statistical parameters for comparing different mesh sizes derived from 1000 random points.

Mesh size (m)	**Mean depth (m)**	**Median depth (m)**	**STD (m)**	**R^2**	**RMSE**	**Correlation**	**Computation Time (hh:mm:ss)**	**Inundation Area (km^2)**
6.0 x 6.0	4.055	3.710	2.626	-	-	-	22:05:04	26.22
7.5 x 7.5	4.058	3.715	2.623	0.9999	0.0220	1.0000	16:09:33	26.21
10 x 10	4.055	3.726	2.622	0.9999	0.0288	0.9999	03:09:48	26.20
25 x 25	4.046	3.708	2.618	0.9997	0.0436	0.9999	00:07:34	26.19
50 x 50	4.034	3.708	2.607	0.9972	0.1388	0.9987	00:04:56	26.16

The model outcomes showed that the base model (6.0x6.0 m) and the models with 7.5x7.5 m, 10x10 m, and 25x25 m grid sizes were strongly correlated, exhibiting high R^2 values (0.9999) and low RMSE values (0.022, 0.0288, and 0.0436 respectively), as well as similar inundation areas. For the 50x50 m grid size, the correlation value was calculated as 0.9972. Although this value is slightly lower than the other grid sizes, it is still considered a high correlation. However, the R^2 value (0.9972) and the RMSE value (0.1388) indicate increased error and deviation compared to the smaller grid sizes. In conclusion, the 50x50 m grid size may be appropriate for analyses requiring lower levels of detail. However, in terms of accuracy, smaller grid sizes, such as 6.0x6.0 m, 7.5x7.5 m, and 10x10 m, demonstrate superior reliability and precision. Consequently, a 6 m mesh size was used in subsequent scenario analyses to ensure the highest level of detail and accuracy.

The study examined the impact of grid size on computational performance and inundation results. A 6.0 x 6.0 m grid size produced 879,214 cells, an inundation area of 26.22 km^2, and a computational time step (ΔT) of 0.3 seconds. When the grid size increased to 7.5 x 7.5 m, the number of cells decreased to 559,222, the

inundation area slightly reduced to 26.21 km², and the time step increased to 0.5 seconds. Similarly, a 10 x 10 m grid size further reduced the number of cells to 316,398, the inundation area to 26.20 km², and the time step to 1.0 seconds. For larger grid sizes, such as 25 x 25 m and 50 x 50 m, the total cell counts were 51,635 and 12,829, respectively, with a time step of 1.0 seconds. Additional details regarding the computational time step are provided in Section 5.1.2.1 below.

The computation times, as presented in Table 5.2, were obtained using a system equipped with an Intel® Core™ i5-8265U CPU @ 1.60GHz (up to 1.80GHz) and 8GB of RAM. It is important to note that the simulation times are specific to the performance capabilities of this hardware configuration and the selected time steps.

Ashraf (2021) analyzed the sensitivity of different grid sizes on a cross-sectional basis, demonstrating that a 5 m grid size provided the most accurate results for flood extent and flow depth, though at the cost of significantly increased computational time. In contrast, the 10 m grid size achieved a balance between accuracy and computational efficiency. In comparison, the 25 m and 50 m grid sizes led to a decline in model performance and loss of terrain detail. In the present study, grid size sensitivity was assessed at a regional scale using RMSE and R^2 analyses across 1000 points within the flood area, offering a distinct perspective on the influence of grid size variations on model performance.

The results align with and validate findings documented in previous studies conducted by various researchers; however, using high-spatial-resolution DEMs is recommended for future studies aiming to increase the accuracy of 2D hydrodynamic models, (Brunner et al., 2015), (Mattas et al., 2023), (Ibrahimkhan et al., 2022).

5.1.2.1 Computational Time Steps

HEC-RAS discretizes the governing equation both spatially and temporally. The temporal resolution of the numerical simulation directly impacts the accuracy of the approximations of the temporal derivatives in the governing equation. The selection of suitable time intervals depends on how the hydraulic characteristics evolve between two successive time intervals. The selection of excessively large time steps may result in a significant disparity in hydraulic properties between two consecutive time steps, leading to instability. Using a computational time step that is too small will increase the overall computational time (USACE 2014).

The optimal approach for determining a computational time step in HEC-RAS is using the Courant Condition. This becomes particularly crucial in the context of dam break flood studies (USACE 2014). According to the Courant Condition, the recommended time step should be as follows:

$$C = \frac{v_W \, \Delta T}{\Delta X} \leq 1 \tag{5.1}$$

and therefore

$$\Delta T \leq \frac{\Delta X}{v_W} \tag{5.2}$$

Where C is the Courant Number, ΔT is the time step (in seconds), ΔX is the distance step (in meters), and v_W is wave speed (meter per second).

This sensitivity analysis aims to evaluate how variations in the computational time step affect both the model's stability and the accuracy of the simulation. This study determined the computational time step value using Equation 5.2 through an iterative trial-and-error procedure, Table 5.3. The ultimate value of the computational time step was derived for different mesh size models.

Table 5.3 Time Step and distance step values for different mesh sizes

Mesh size (m)	***ΔX* (m)**	***ΔT* (sec)**
6.0 x 6.0	6.00	0.30
7.5 x 7.5	7.50	0.50
10.0 x 10.0	10.0	1.00
25.0 x 25.0	25.00	1.00
50.0 x 50.0	50.00	1.00

5.1.3 Comparison of Different Governing Equations

The HEC-RAS 2D program provides various analytical methods for modeling unsteady flow in open channels and floodplains. It uses full momentum equations, also called Shallow Water Equations (SWE) or 2D-Saint Venant Equations as well, to capture the complete dynamics of flow, while the diffusive wave method offers a simplified approach to model flow movement. In this study, analyses were carried out using both methods, and their results were compared. The question of which hydrodynamic approach, whether the diffusion wave model or the shallow water model, provides a more accurate and reliable simulation of the dynamics of a flood resulting from a dam failure has been investigated along the course of the study.

HEC-RAS 2D offers its users alternative solution methods for applying both full momentum and diffusive wave equations in water surface engineering. The diffusive wave approximation assumes that gravity and friction are the primary forces exerted on the control volume. Conversely, the 2-D full momentum equation solver incorporates acceleration terms, turbulence, and Coriolis effects in addition to those forces in the flow field, necessitating increased computational power and longer simulation times.

The 2D Saint Venant equations in their non-conservative forms are as follows:

$$\frac{\partial H}{\partial t} + \frac{\partial (hu)}{\partial x} + \frac{\partial (hv)}{\partial y} + q = 0 \tag{5.3}$$

$$\frac{\partial u}{\partial t} + u\frac{\partial u}{\partial x} + v\frac{\partial u}{\partial y} = -g\frac{\partial H}{\partial x} + V_t\left(\frac{\partial^2 u}{\partial x^2} + \frac{\partial^2 u}{\partial y^2}\right) - c_f u + fv \tag{5.4}$$

$$\frac{\partial v}{\partial t} + u\frac{\partial v}{\partial x} + v\frac{\partial v}{\partial y} = -g\frac{\partial H}{\partial y} + V_t\left(\frac{\partial^2 v}{\partial x^2} + \frac{\partial^2 v}{\partial y^2}\right) - c_f v + fu \tag{5.5}$$

The variables in the equation are defined as follows: *t* represents time, *u* and *v* represent the horizontal components of velocity in the *x* and *y* directions, respectively, and *q* represents a term that represents a source or sink of flux. *H* represents the elevation of the water surface, *h* represents the depth of the water, *g* represents the acceleration due to gravity, V_t represents the coefficient of horizontal eddy viscosity, c_f represents the coefficient of bottom friction, and *f* represents the Coriolis parameter. (Brunner, 2016)

According to Brunner (n.d), in his presentation "Diffusion Wave vs. Full Momentum (SWE)" the Diffusion Wave Equation (DWE) method provides a fast and stable solution, particularly suitable for flows primarily driven by gravity and friction forces. The DWE method is ideal for estimating broad-scale scenarios, such as flood extents, and serves as a quick preliminary tool before applying more complex models. However, due to neglected acceleration terms, its accuracy is limited in sudden flow changes or where detailed velocity distributions are required.

The advantages and limitations of the methods discussed in this study are derived from CivilGEO's HEC-RAS 2D computational equations comparison article (CivilGEO, n.d.). The methods, along with their strengths and limitations, are outlined below.

Diffusion Wave Equation:

The Diffusion Wave Equation (DWE) method is commonly used as a default solver due to its efficiency and ability to model a wide range of hydraulic processes. This method is particularly effective for many flood simulation studies. As a computational approach for simulating 2D flow, the Diffusion Wave Equation offers specific strengths and limitations outlined below:

Strengths of DWE:

- It is well-suited for scenarios dominated by gravity and friction forces, such as floodplain inundation modeling.
- It provides faster computation times and can handle larger time steps with improved stability.
- It is useful for estimating the effects of dam failures or levee breaches in enclosed areas.
- It is ideal for obtaining broad flood extent estimations efficiently.
- Serves as a practical tool for generating initial flood assessments before applying more detailed solvers like the Shallow Water Equations (SWE)

Limitations of DWE:

- The method cannot account for fluid acceleration, which reduces its precision in detailed hydrodynamic simulations involving wave dynamics.
- It is not suitable for scenarios with abrupt flow changes, such as sharp contractions or channel expansions.
- It has limitations in accurately predicting detailed velocity profiles around complex structures or within channels.
- Its performance is inadequate in mixed flow regimes or hydraulic jumps.

Shallow Water Equations-Eulerian-Lagrangian Method (SWE-ELM)

The SWE-ELM is a widely used approach for solving the Shallow Water Equations (SWE) in HEC-RAS modeling and applies to various hydraulic conditions. This method offers distinct strengths and limitations, making it a valuable option for specific hydrodynamic applications. Below are the strengths and limitations of this approach:

Strengths of SWE-ELM:

- The SWE-ELM facilitates detailed and highly accurate hydrodynamic modeling, making it suitable for complex hydraulic systems.
- It supports advanced features such as turbulence modeling and Coriolis force considerations, which expand its application in diverse scenarios.
- Compared to the DWE method, it requires shorter computational time steps to ensure numerical stability, thereby improving the precision of results.
- The method performs well in river systems with gentle slopes, ensuring reliable results under such conditions.

Due to these strengths, the SWE-Eulerian-Lagrangian Method is considered a robust and reliable tool for complex hydraulic analyses.

Limitations of SWE-ELM:

- This method requires more processing power, resulting in longer simulation times compared to simpler methods.
- It may experience numerical instability in rapidly changing flow directions, affecting the accuracy of the results.

According to Figure 5.5 and Figure 5.6, while directly comparing the boundaries between the two solution methods may not reveal significant differences, a closer examination of travel time and water surface elevations shows notable variations in many areas. Noticeable differences between the two methods, particularly in velocity and depth, arise because the DWE (Diffusion Wave Equation) method neglects acceleration terms. This omission leads to a failure to account for energy losses in regions with sharp contractions, expansions, or highly dynamic wave phenomena, such as dam breaks or flash floods. The resultant maps for water depth and water surface elevations for both governing equations are provided in Appendix D.

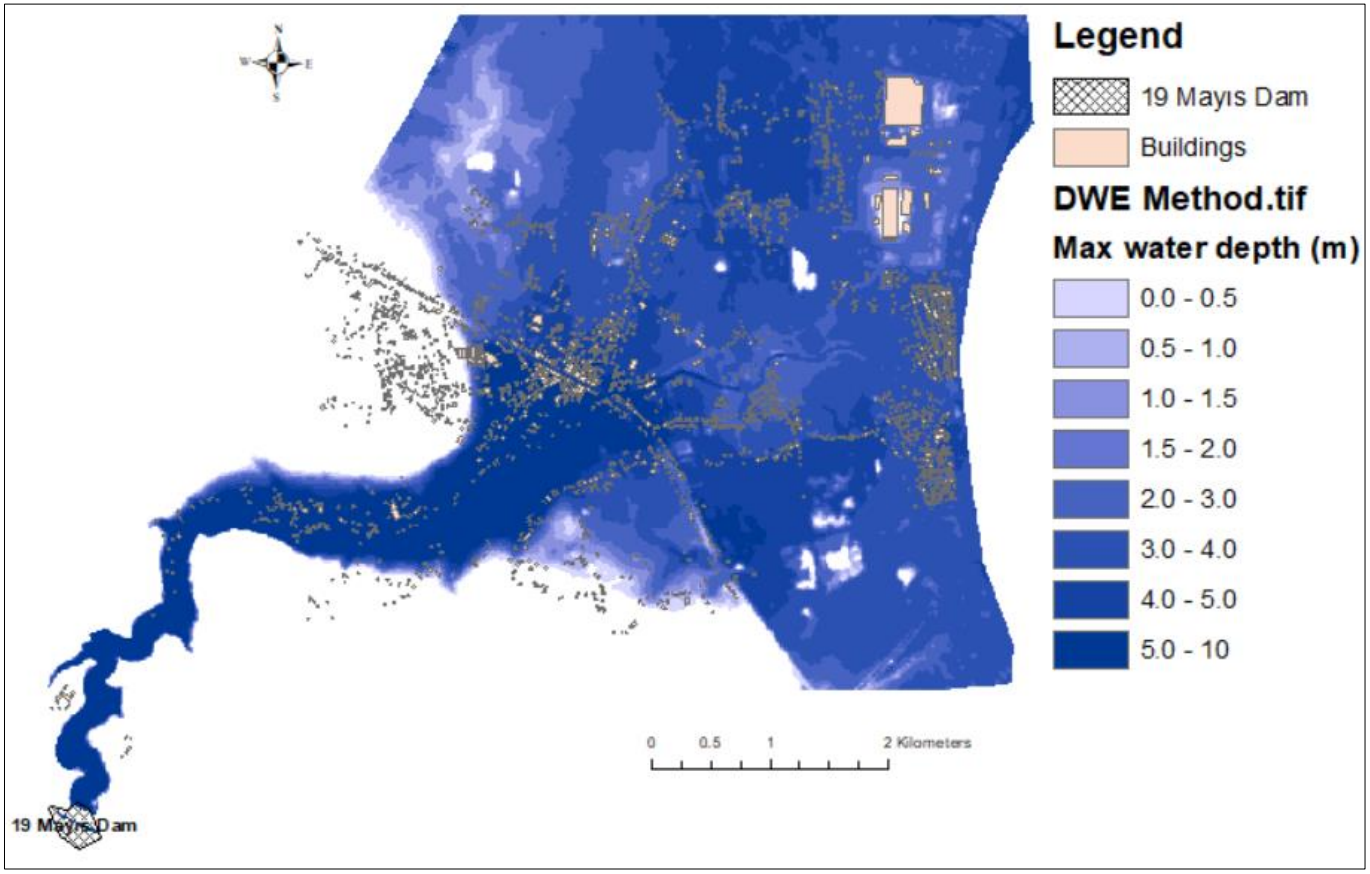

Figure 5.5 Inundation maps for diffusion wave equation method

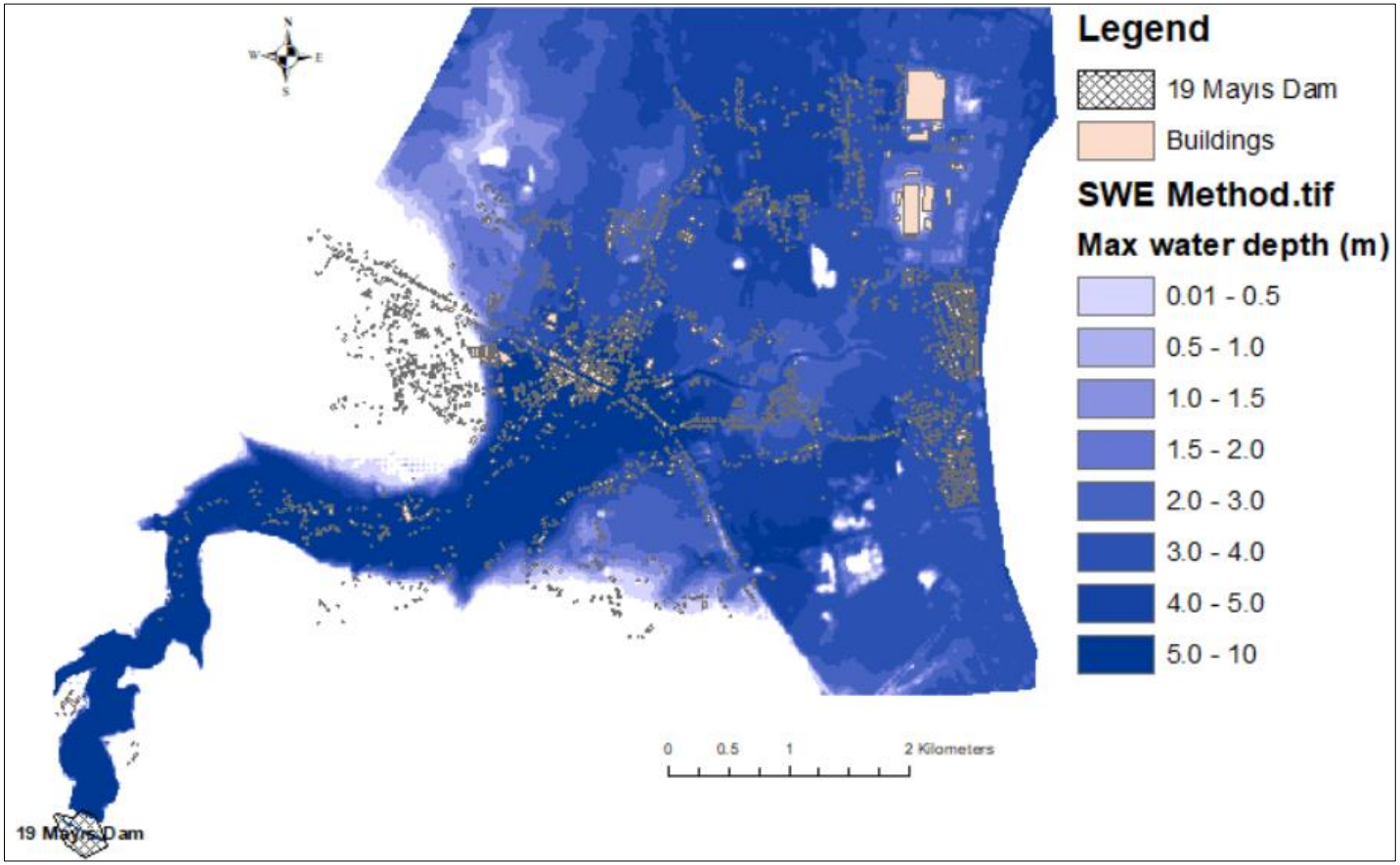

Figure 5.6 Inundation maps for shallow water equation method

When comparing the change in flood area for different equations, the full momentum equation results in a larger flood area, especially in regions with high velocities and sharp curves, Figure 5.7. However, it requires longer computational time compared to the diffusive wave equation. The results indicate that the two models differ in their predictions of flow depths and velocities. In the diffusive wave model, the time it takes for the flood wave to reach downstream points is shorter, and the average velocity of the flood wavefront is higher.

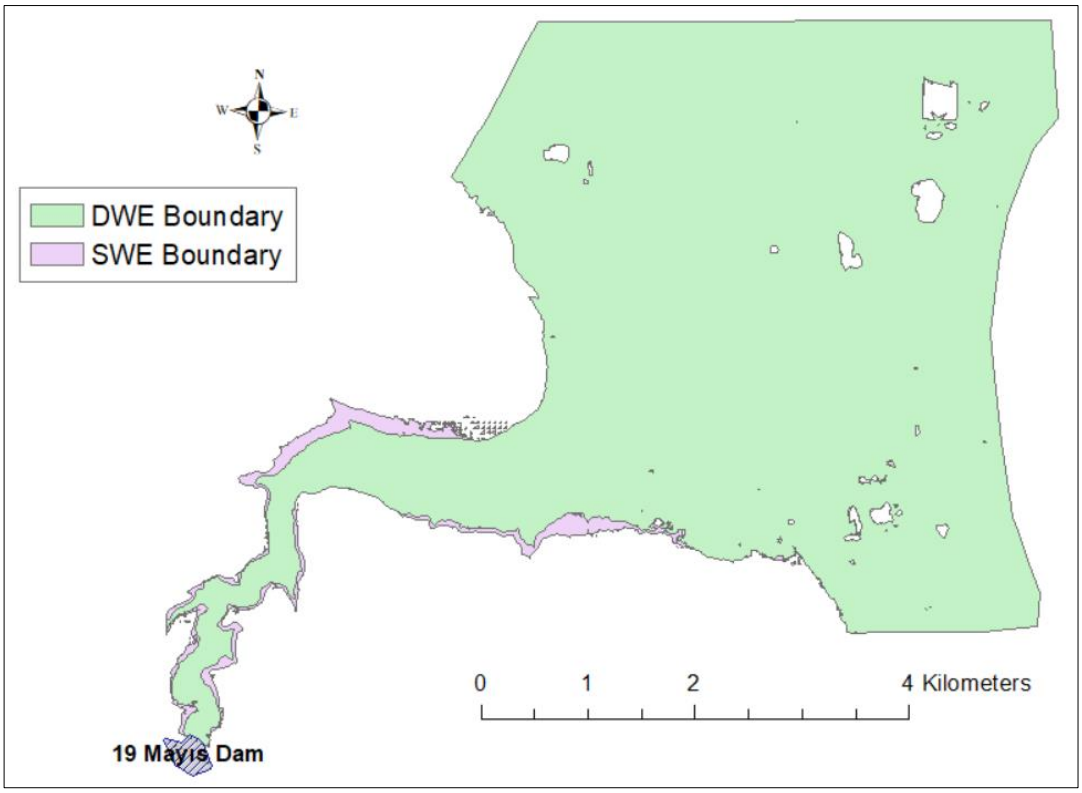

Figure 5.7 Boundary of the inundation map corresponding to different solution methods

The breach scenario used for the comparison of governing equations is defined as follows: the breach occurs when the water surface elevation reaches 167.00 m, and the breach formation time is assumed to be 30 minutes. The simulation starts at 00:00 (hh:mm), and based on the inflow conditions, the reservoir reaches the critical level of 167.00 m at 01:30 (hh:mm). In other words, the dam failure begins at this time. Following the breach, the propagation of floodwaters through the breach is analyzed

for different simulation times, as detailed below. The extent of the floodplain area was examined in both solution methods during the same simulation time, and the reasons for the differences were discussed in Figure 5.8 ~ Figure 5.10.

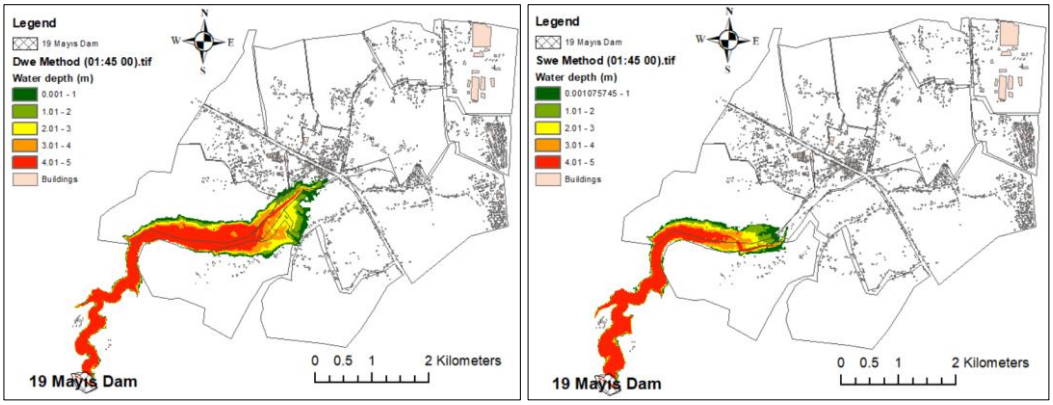

Figure 5.8 Comparison of water depth distributions computed by: a) diffusion wave equation, b) shallow water equation, (at simulation time: 01.45 (hh:mm))

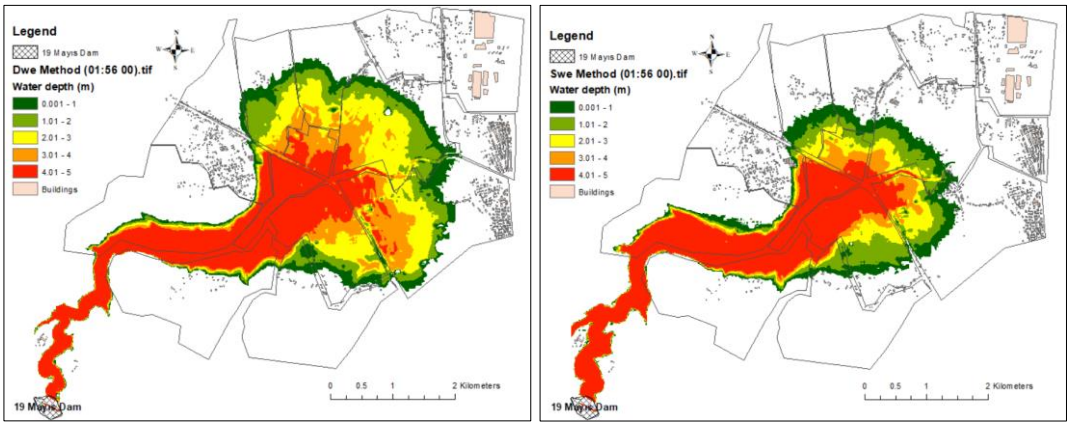

Figure 5.9 Comparison of water depth distributions computed by: a) diffusion wave equation, b) shallow water equation, (at simulation time: 01.56 (hh:mm))

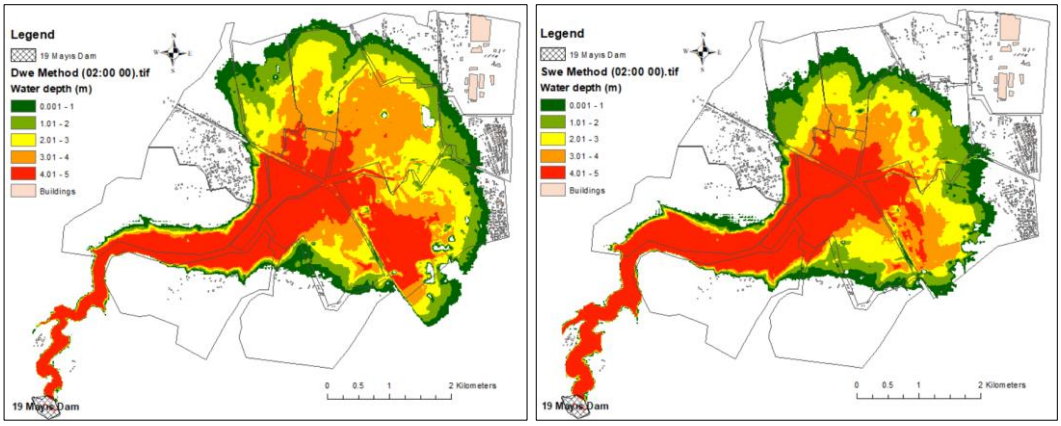

Figure 5.10 Comparison of water depth distributions computed a) diffusion wave equation, b) shallow water equation, (at simulation time: 02.00 (hh:mm)

In the water depth distribution from the DWE, the flow spreads more uniformly, with lower peak depths across the floodplain. The gradual movement of water suggests that this model smooths out sudden changes, leading to a more consistent distribution over time. In contrast, the SWE model shows greater variation in water depth, with higher depths covering larger and more distinct areas. This variation suggests that the SWE model captures the dynamics of the flood wave more accurately, showing sharper changes in depth across the floodplain.

The differences in water depth and flow behavior at different times reflect how these models represent water movement in different ways. The DWE takes a simpler approach by assuming smoother transitions, while the SWE model offers a more detailed and realistic simulation of flow behavior. These differences are important when selecting the most suitable model for specific flood scenarios.

It is recommended to use SWEs for highly dynamic flood events, sudden contractions or expansions, and rivers with gentle slopes. However, some studies suggest that DWEs can still provide accurate results even in these dynamic conditions (Moussa and Bocquillon, 2009; Marangoz and Anilan 2022; Mitsopoulos et al. 2022). Additionally, Yılmaz et al. (2023) do not recommend DWEs for flat plains; they compared both methods and concluded that SWE solutions were more appropriate and thus were used for further analysis.

5.1.4 Sensitivity Analyses of Breach Parameter Prediction Equation

Risk assessment studies related to embankment dam failures commonly apply breach parameter estimation methods developed through analyses of past dam failures. Similarly, predictions for peak breach outflow are made using empirical relationships based on historical case data, (Wahl, 2004).

To perform a dam-break flood routing simulation, breach parameters must first be estimated. These parameters then serve as inputs to the model used for dam-break and flood routing simulations. Multiple methods exist for estimating these parameters, each offering different approaches to match specific modeling needs.

Numerous researchers have created regression equations to determine breach dimensions such as width, side slope, and volume of erosion and failure time. These equations were formulated based on data collected from earthen dams, earthen dams with impermeable cores (like clay or concrete), and rockfill dams. Wahl conducted a study in 1998 that summarized the existing methods used to predict breach parameters. (Wahl, 1998) The breach prediction equations and details presented in this section are directly derived from Wahl's research.

The guideline published by the Dam Safety Office in 1998 states that the regression equations by Froehlich (1995a, 2008), MacDonald and Langridge-Monopolis (1984), and Von Thun and Gillette (1990) have been widely used in various dam safety studies in the literature, except for the Xu and Zhang (2016) equation. Therefore, these regression equations, except for the Xu and Zhang approach, were compared and utilized accordingly.

MacDonald and Langridge-Monopolis (1984)

MacDonald and Langridge-Monopolis developed prediction equations using 42 data sets, primarily consisting of earth-fill dams, earth-fill dams with a clay core, and rock-fill dams. These data sets capture the relationship between the volume of water released from the dam and the volume of material eroded from the dam's

embankment. The data used by MacDonald and Langridge-Monopolis for their regression analysis fall within the following ranges;

Height of the dams: 4.27 – 92.96 meters (with 76% < 30 meters, and 57% < 15 meters)

Breach Outflow Volume: 0.0037 x 10^6 m^3 – 660.0 x 10^6 m^3 (with 79% < 25.0 x 10^6 m^3, and 69% < 15.0 x 10^6 m^3)

The equation developed by MacDonald and Langridge-Monopolis estimates the volume of eroded material and the time required for breach formation;

For earth fill with clay core or rockfill dams:

$$V_{eroded} = 0.00348(V_{out}\, x\, h_w)^{0.852} \quad (5.6)$$

$$T_f = 0.0179(V_{eroded})^{0.364} \quad (5.7)$$

Where V_{eroded} represents the volume of material eroded from the dam embankment in cubic meters, V_{out} is the volume of water passing through the breach, measured in cubic meters. It includes the storage volume at the time of the breach, the inflow volume after the breach begins, and any flow-through spillways or gates once the breach has started. The variable h_w denotes the water depth above the bottom of the breach in meters, and T_f is the breach formation time in hours. It should be noted that Wahl's study indicates that this method may overestimate times in some instances, whereas many other equations tend to underestimate.

Von Thun and Gillette (1990)

Von Thun and Gillette developed their methodology using 57 dams from the studies by Froehlich (1987) and MacDonald and Langridge-Monopolis (1984). The data Von Thun and Gillette used for their regression analysis fell within the following ranges.

Height of the dams: 3.66 – 92.96 meters (with 89% < 30 meters, and 75% < 15 meters)

Volume of water at breach time: 0.027 x 10^6 m^3 – 660.0 x 10^6 m^3 (with 89% < 25.0 x 10^6 m^3, and 84% < 15.0 x 10^6 m^3)

The Von Thun and Gillette equation for average breach width is:

$$W = 2.5h_w + C_b \quad (5.8)$$

Where W represents the average breach width in meters, h_w is the water depth above the bottom of the breach in meters, and C_b is a coefficient dependent on reservoir size, as shown in Table 5.4.

Table 5.4 C_b coefficient depending on the reservoir size

Reservoir Size (m^3)	**C_b (m)**	**Reservoir Size (acre-ft)**	**C_b (ft)**
< 1.23 x 10^6	6.1	< 1,000	20
1.23 x 10^6 – 6.17 x 10^6	18.3	1,000 – 5,000	60
6.17 x 10^6 – 1.23 x 10^7	42.7	5,000 – 10,000	140
> 1.23 x 10^7	54.9	> 10,000	180

Von Thun and Gillette developed two alternative breach formation time equations for "erosion resistant" and "easily erodible" dams.

$$T_f = 0.02h_w + 0.25 \text{ (erosion resistant)} \quad (5.9)$$

$$T_f = 0.015h_w \ (easily\ erodible) \quad (5.10)$$

Where:

T_f = breach formation time (hours)

h_w = depth of water above the bottom of the breach (meters)

Froehlich (1995a)

Froehlich employed a total of 63 data sets, including those from earthen, zoned earthen, earthen with a clay core, and rockfill dams, to create a set of equations aimed

at predicting average breach width, side slopes, and failure time. The ranges of data used by Froehlich for his regression analysis are as follows:

Height of the dams: 3.66 – 92.96 meters (with 90% < 30 meters, and 76% < 15 meters)

Volume of water at breach time: 0.0130 x 10^6 m^3– 660.0 x 10^6 m^3 (with 87% < 25.0 x 10^6 m^3 , and 76% < 15.0 x 10^6 m^3)

Average breach width and failure time for Froehlich's regression equation

$$W = 0.1803\, K_o\, V^{0.32} h_b^{0.19} \tag{5.11}$$

$$T_f = 0.00254\, V_w^{0.53} h_b^{-0.90} \tag{5.12}$$

Where W represents the average breach width in meters, K_o is constant (1.4 for overtopping failures and 1.0 for piping) V_w is the reservoir volume at the time of failure in cubic meters, h_b is the height of the final breach in meters, and T_f is the breach formation time in hours.

Froehlich also states that the average side slopes should be 1.4H/1V for overtopping failures and 0.9H/1V for other scenarios.

Froehlich (2008)

In 2008, Froehlich revised his breach equations by incorporating new data. He analyzed 74 data sets, including earthen, zoned earthen, earthen with a clay core, and rockfill dams, to formulate a set of equations for predicting average breach width, side slopes, and failure time. The ranges of data utilized by Froehlich for his regression analysis are as follows:

Height of the dams: 3.05 – 92.96 meters (with 93% < 30 meters and 81% < 15 meters)

Volume of water at breach time: 0.0139 x 10^6 m^3– 660.0 x 10^6 m^3 (with 86% < 25.0 x 10^6 m^3, and 82% < 15.0 x 10^6 m^3)

The average breach width and failure time, according to Froehlich's regression equations are:

$$W = 0.27\, K_o\, \mathrm{V}_w^{0.32} h_b^{0.04} \tag{5.13}$$

$$T_f = 63.2 \sqrt{\frac{V_w}{g h_b^2}} \tag{5.14}$$

Where W represents the average breach width in meters, K_o is constant (1.3 for overtopping failures and 1.0 for piping), Vw is the reservoir volume at the time of failure in cubic meters, h_b is the height of the final breach in meters, g is the gravitational acceleration (9.80665 meters per second squared), and T_f is the breach formation time in seconds.

Froehlich also states that the average side slopes should be 1.0H/1.0V for overtopping failures and 0.7H/1.0V for other scenarios.

Alongside these equations, numerous federal agencies have issued guidelines that provide potential ranges for breach width, side slopes, and development time.Table 5.5 outlines several of these guidelines. These guidelines should be used as minimum and maximum bounds for estimating breach parameters (USACE, 2014).

Table 5.5 The value ranges for breach characteristics based on USACE (2016)

Dam type	**Average breach width (*W*)**	**Horizontal component of breach side slope (*S*=H:1 V)**	**Failure time T_f (hours)**	**Agency**
Earthen/ Rockfill	(0.5 to 3.0) x *HD*	0 to 1.0	0.5 to 4.0	COE 1980
Earthen/ Rockfill	(1.0 to 5.0) x *HD*	0 to 1.0	0.1 to 1.0	FERC
Earthen/ Rockfill	(2.0 to 5.0) x *HD*	0 to 1.0 (Slightly larger)	0.1 to 1.0	NWS
Earthen/ Rockfill	(0.5 to 5.0) x *HD**	0 to 1.0	0.1 to 4.0	COE 2007

*Where: *HD* height of the dam

**Dams with huge volumes of water and long dam crest lengths will continue to erode for long durations (i.e., as long as a significant amount of water is following through the breach) and may, therefore, have longer breach widths.

The peak outflow discharge (Q_p) and breach development time (T_p) for dam failures were compared using four different approaches, Table 5.6. Appendix C provides the resultant maps for maximum velocity distribution, arrival time, water depth, and water surface elevations for each breach parameter prediction equation.

Table 5.6 Dam breach outflow & breach development hour of analyses

Approach	Variable	Unit	Failure Type	Value
Froehlich (1995)	Q_p	(m^3/s)	Overtopping	56.3 x 10^3
	T_p	min.		53.4
Froechlich (2008)	Q_p	(m^3/s)	Overtopping	53.2 x 10^3
	T_p	min.		45
Von Thun & Gilette	Q_p	(m^3/s)	Overtopping	62.9 x 10^3
	T_p	min.		136.2
MacDonald & Monopolis	Q_p	(m^3/s)	Overtopping	27.9 x 10^3
	T_p	min.		92.4

As seen in Table 5.6 and Figure 5.11, the results for peak outflow discharge (Q_p) and breach development time (T_p) are as follows: the Froehlich (1995) method estimates Q_p = 56.3 x 10^3 m^3/s and T_p = 53.4 minutes, while the Froehlich (2008**)** method gives Q_p = 53.2 x 10^3 m^3/s and T_p = 45 minutes. The Von Thun & Gillette method produces the highest values, with Q_p = 62.9 x 10^3 m^3/s and T_p = 136.2 minutes. In contrast, the MacDonald & Monopolis method provides the lowest discharge of Q_p = 27.9 x 10^3 m^3/s and a breach time of T_p = 92.4 minutes**.**

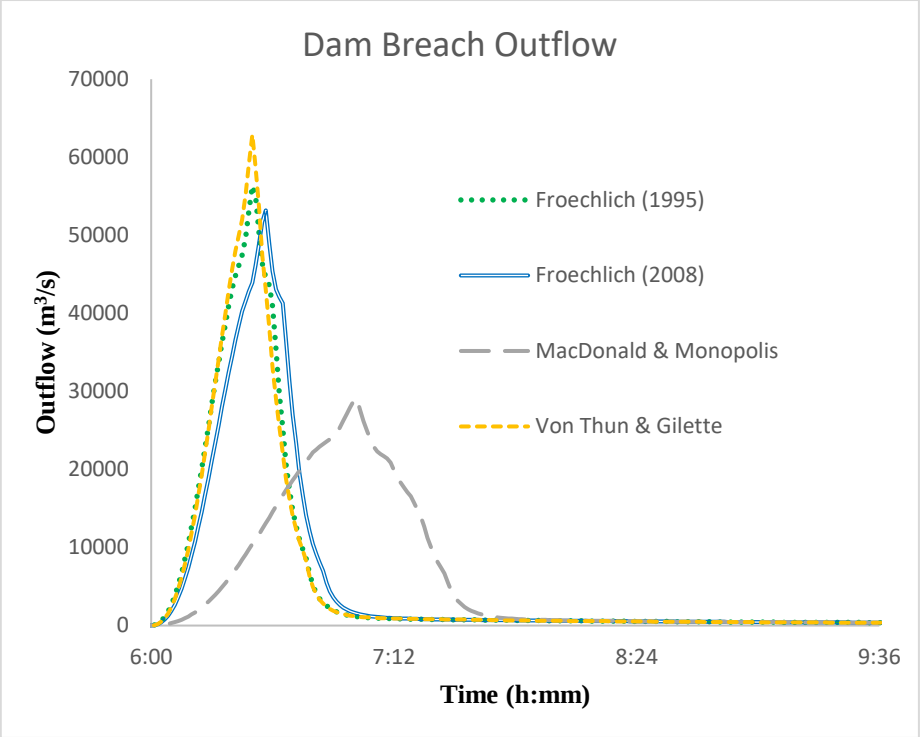

Figure 5.11 Breach outflow for all approaches in overtopping failure mode.

The hydrograph patterns calculated using the approaches of Von Thun and Gillette showed fewer peaks and shorter base times. At the same time, Froehlich's (2008) method provided moderate outputs for both quantities (peak discharge and peak time). In contrast, MacDonald and Monopolis's approach produced hydrographs with longer times to peak discharge and base durations, reducing peak values by roughly half. Froehlich's (1995) method resulted in the highest peak discharge in the shortest time compared to the other approaches. However, this method was later updated and refined into the 2008 version, incorporating a larger database for improved accuracy.

Considering various analyses and dam-break studies in the literature, it is evident that Froehlich's (2008) method provides the most reliable results. According to the analysis by Kostecki and Banasiak (2020), Froehlich's (2008) equations can predict peak discharge within a 3% confidence interval. Yılmaz et al. (2023) also showed in their study Froehlich's (2008) method is most reliable. Additionally, the results of the dam break study on Ürkmez Dam, based on the research by Najar and Gül (2022),

reveal that the Froehlich approach is the most reliable method for estimating dam-breach parameters.

5.1.5 Comparison of Different Dam-Break Scenarios

Froehlich's (2008) method provided more moderate results for peak discharge and time to peak compared to other empirical methods. Various authors, such as Yılmaz et al. (2023) and Najar and Gül (2022), have agreed that Froehlich's approach is the most reasonable method for estimating dam-breach parameters; therefore, the Froehlich equation was used for scenario-based comparisons. Additionally, since the SWE method is recommended for flat plains, it was employed in the scenarios developed for this study.

As shown in Table 5.7, breach parameters for Ondokuz Mayıs Dam (according to the Froehlich, 2008 method) are presented. Four scenarios based on the Froehlich breach parameters were used: Scenarios 1 and 3, which involve overtopping failure (rainy day), and Scenarios 2 and 4, which involve piping failure (sunny day). These scenarios were simulated along with flood routing over the downstream floodplain.

Table 5.7 Breach parameters for Ondokuz Mayıs Dam (according to Froehlich, 2008 method)

Breach Scenario	**Scenario-1**	**Scenario-2**	**Scenario-3**	**Scenario-4**
Mode of failure	**Overtopping**	**Piping**	**Overtopping**	**Piping**
Bottom width (m)	72	54	72	54
Breach formation timing (hr)	0.75	0.68	1.5	1.5
Side Slope (H:V)	1.0	0.7	1.0	0.7
Peak Flow (m^3/sec)	51983.44	52417	30143.9	34285.61
Time to Peak Flow (hr)	0:33	0:34	0:57	1.00

For overtopping scenarios, the breach was assumed to begin when the reservoir reached its maximum water level of 166.80 m, six hours after the probable maximum flood. At this point, water exceeds the crest level, reaching 169.50 m. Figure 5.12 presents a sketch illustrating the dam crest level and the maximum water level. The elevation of 169.50 m corresponds to the water level associated with the volume of water that reached the reservoir six hours after the onset of the probable maximum flood (PMF), as calculated based on the reservoir's capacity and inflow characteristics detailed in the hydrological analysis. Furthermore, the six-hour timeframe was strategically selected for the simulation to surpass the peak discharge and allow for significant volume accumulation, assessing the dam's resilience under extreme conditions.

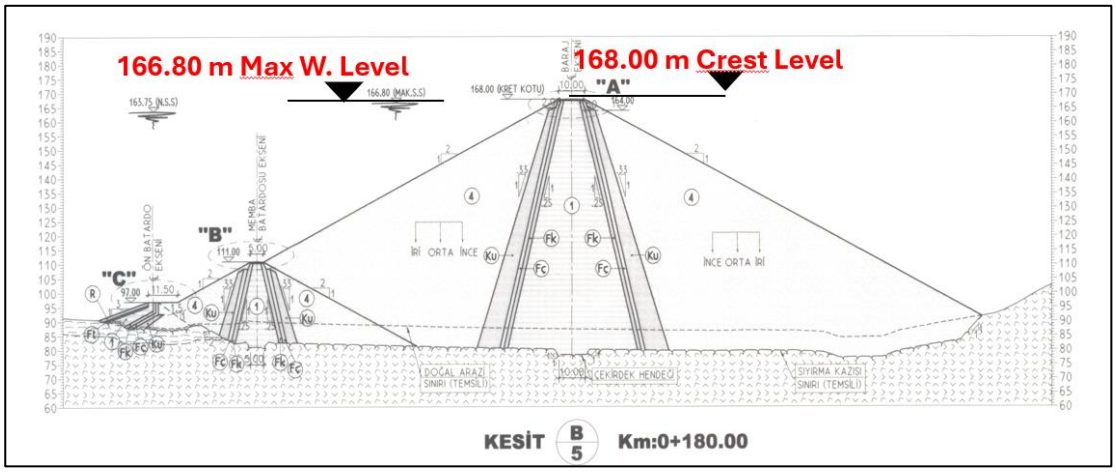

Figure 5.12 Maximum water level and crest level of the dam

Figure 5.13 illustrates the breach initiation process during overtopping scenarios. The graph shows that the reservoir water level reached its maximum of 166.80 m six hours after the probable maximum flood (PMF). At this point, water overtopped the dam crest level, rising further to 169.50 m, which triggered the breach. The plot includes the water elevation, breach width, and flow velocity changes over time, highlighting the rapid drop in elevation and velocity following the breach.

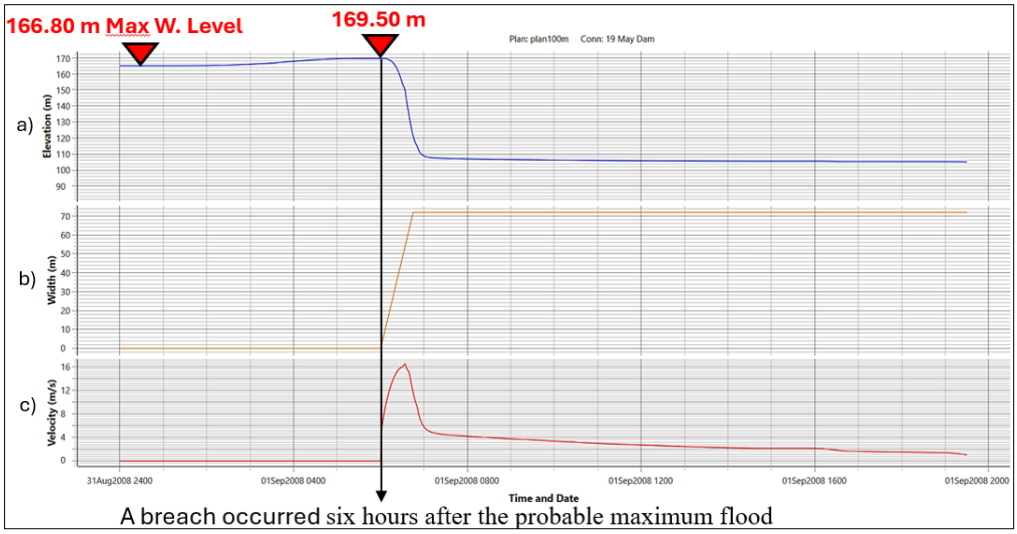

Figure 5.13 a) Time-series of reservoir elevation, b) breach width, and c) outflow velocity during dam failure

Figure 5.14 presents the routed probable maximum flood (Q_{PMF}) hydrograph. The peak flood discharge reached 1405 m^3/s at the 4.5^{th} hour, after which the flow gradually decreased. At t = 6 hours, the flood volume accumulated at the moment of breach formation was calculated as 15.31 hm^3 from the hydrograph.

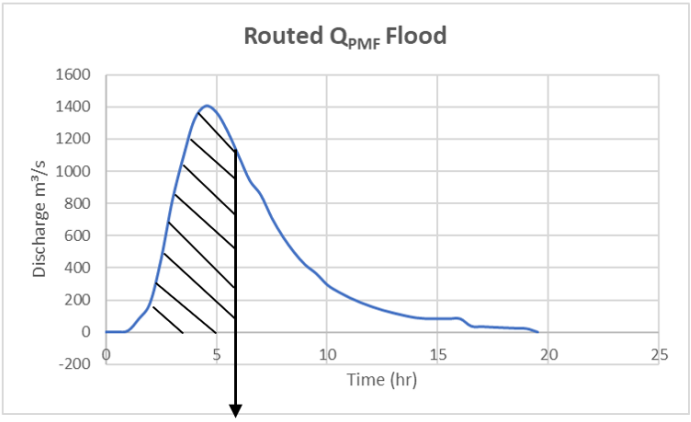

Figure 5.14 Routed (Q_{PMF}) probable maximum flood hydrograph through the reservoir

Figure 5.15 presents a sketch illustrating the dam crest and normal water levels for the piping case. The analysis began at the normal water level for piping scenarios (sunny days), assuming base flow (3.5 m³/s) conditions. The initial piping elevation was determined through trial and error to be 127.60 m in order to achieve the highest breach outflow.

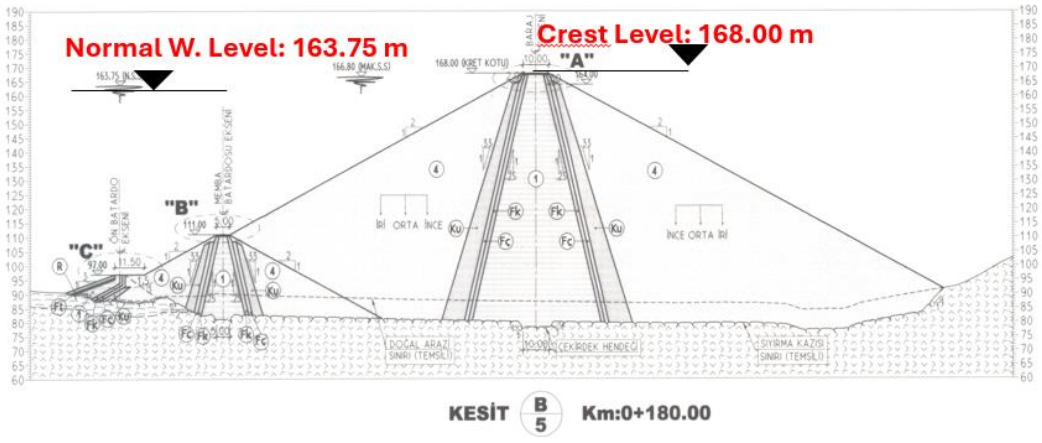

Figure 5.15 Normal water and crest level of the dam

Figure 5.16 presents the breach hydrographs for four scenarios of Ondokuz Mayıs Dam. When the outflow hydrographs resulting from the breach are examined, it can be seen that the results of Scenario 1 and Scenario 2 are similar, as are the results of Scenario 3 and Scenario 4, due to their close failure times. However, the hydrograph geometries differ, which results in variations in arrival times for each scenario. Since the failure times are close, their peak arrival times are also near. It should be noted that the areas under the piping and overtopping hydrographs are equal, as the area of a hydrograph represents the total volume of water released.

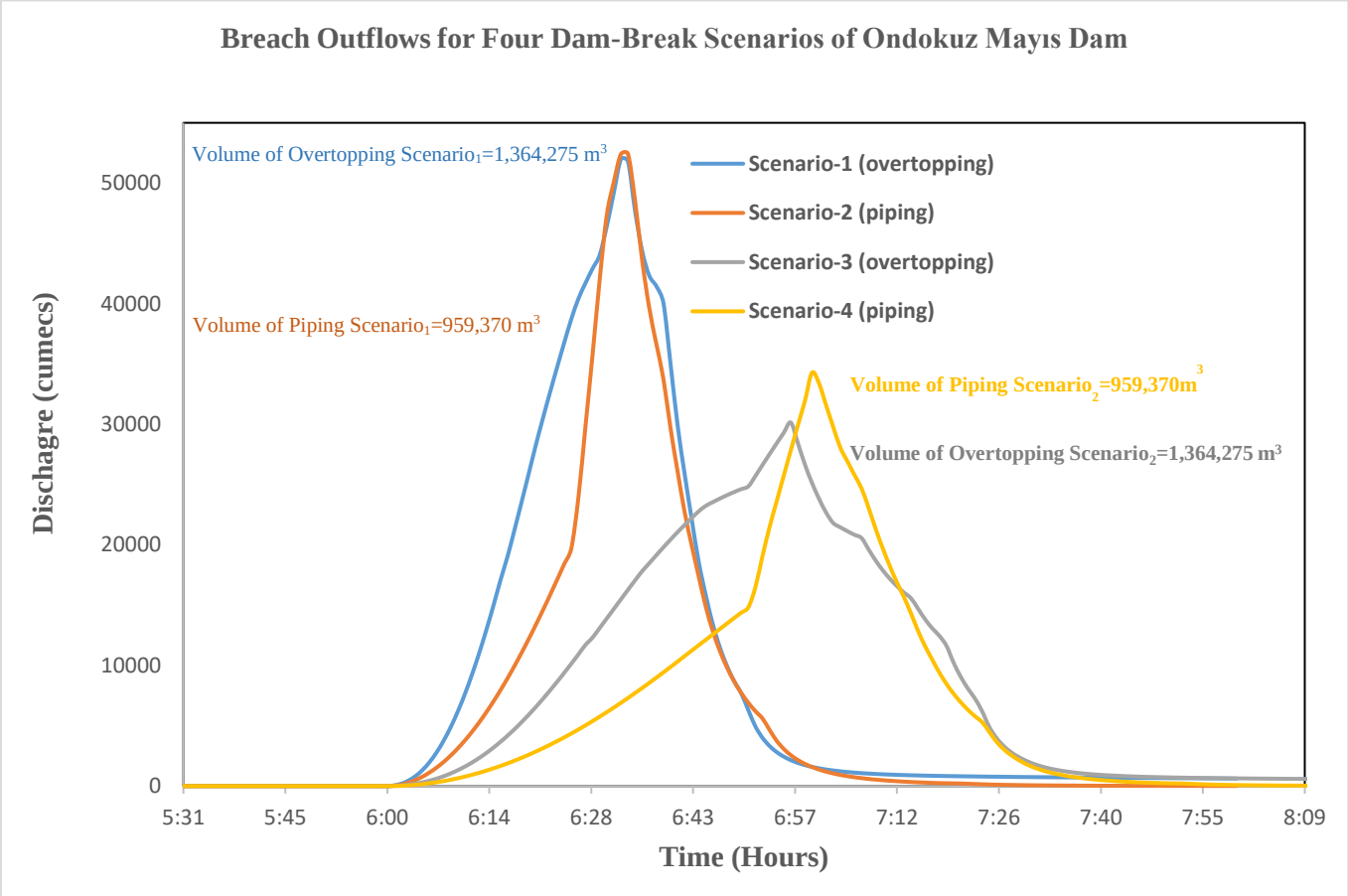

Figure 5.16 Breach hydrograph for four Scenarios of Ondokuz Mayıs Dam

Figure 5.17 shows the hydrographs for the worst-case scenarios, Scenario 1 and Scenario 2. The arrival time of the flood wave varies depending on whether the failure scenario involves overtopping or piping. This is due to differences in the total volume of water released from the breach. However, although the failure mechanisms differ, both scenarios ultimately result in a complete dam breach. While the total released water volume varies between scenarios, the peak outflow and timing similarity can be attributed to the comparable breach formation times. Since the rate of breach expansion is similar, the hydrographs exhibit nearly identical peak discharges despite differences in the total volume released. For the worst-case scenarios, Scenarios 1 and 2, the flood's arrival time, water depth, and velocity were compared across specific neighborhoods. These analyses contribute to determining the necessary response times and identifying priority areas for flood mitigation efforts.

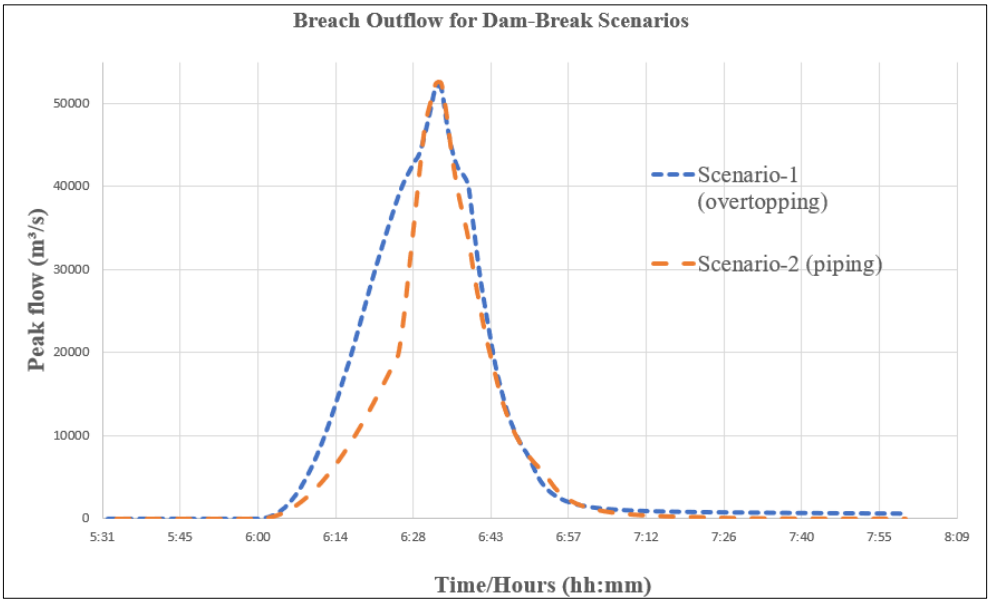

Figure 5.17 Breach hydrograph for worst scenarios of Ondokuz Mayıs Dam

Figure 5.18 and Figure 5.19 present the maximum water depth maps and flood arrival times at critical residential areas and bridges for the overtopping and piping scenarios of the Ondokuz Mayıs Dam, respectively. These maps illustrate the spread of floodwaters across various regions, considering both water depth and flow velocity.

In the overtopping scenario, the probable maximum flood (PMF) began at midnight (00:00 AM), causing the water level to exceed the dam crest at 04:08 AM, followed by breach initiation at 06:00 AM. As a result, floodwaters rapidly approach residential areas. In the piping scenario, the flood event is assumed to start at 06:00 AM.

The reason for initiating the PMF at midnight and scheduling the dam failure for the early morning hours during scenario development is that this period represents a critical time when emergency response is most challenging due to limited visibility and the fact that most people are asleep, significantly increasing the overall risk.

Figure 5.20 presents the maximum velocity distributions for the piping and overtopping scenarios. In the overtopping scenario, red and orange tones spread over a larger area, indicating higher flow velocities and showing that water flows over the dam and rapidly inundates a wide region. The flow in this scenario is more abrupt and intense, resulting in faster water reaching residential areas and bridges.

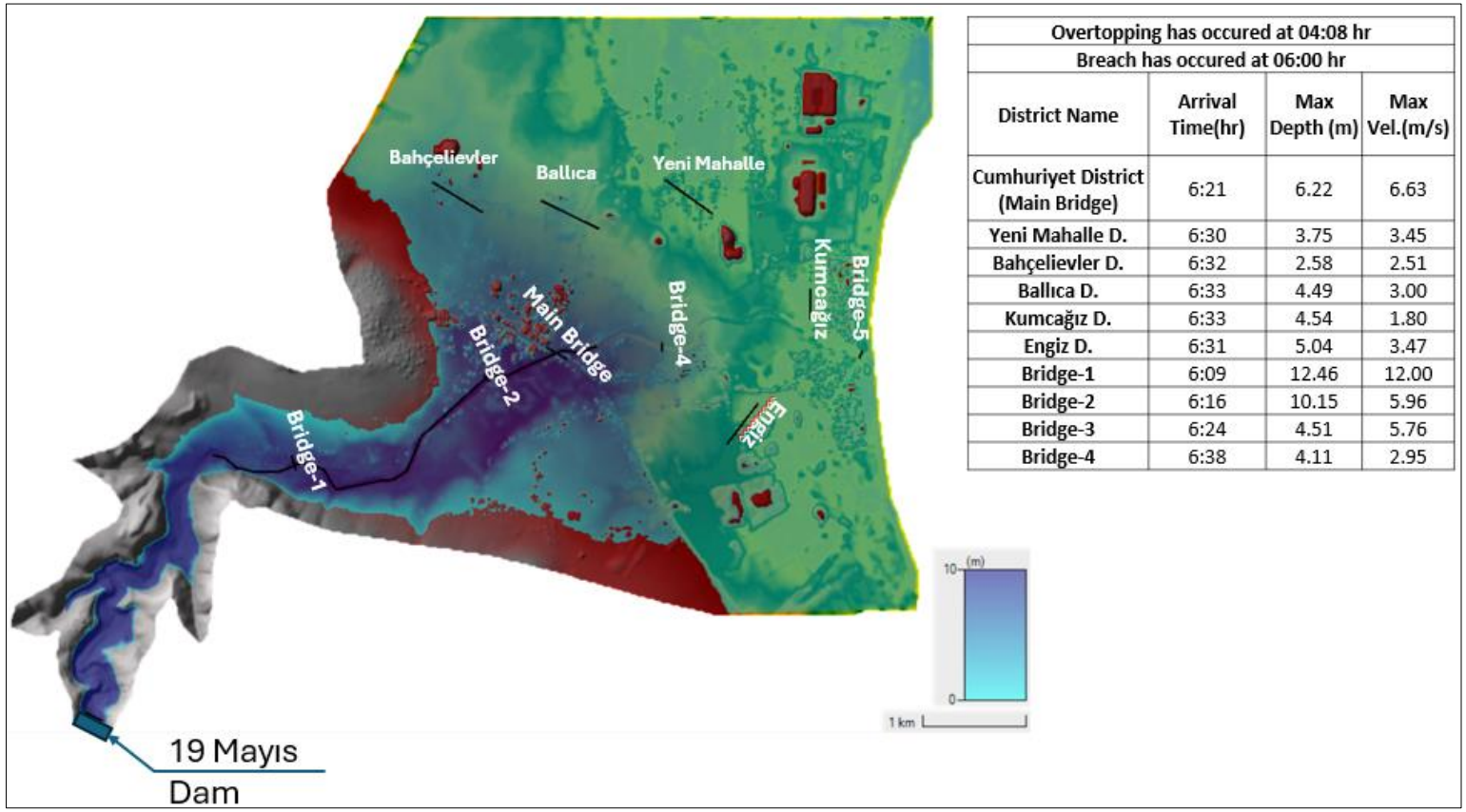

Overtopping has occured at 04:08 hr			
Breach has occured at 06:00 hr			
District Name	Arrival Time(hr)	Max Depth (m)	Max Vel.(m/s)
Cumhuriyet District (Main Bridge)	6:21	6.22	6.63
Yeni Mahalle D.	6:30	3.75	3.45
Bahçelievler D.	6:32	2.58	2.51
Ballıca D.	6:33	4.49	3.00
Kumcağız D.	6:33	4.54	1.80
Engiz D.	6:31	5.04	3.47
Bridge-1	6:09	12.46	12.00
Bridge-2	6:16	10.15	5.96
Bridge-3	6:24	4.51	5.76
Bridge-4	6:38	4.11	2.95

Figure 5.18 Maximum water depth map in the Ondokuz Mayıs floodplain and a summary of the flood arrival times at important residential areas for the overtopping scenario (Scenario-1).

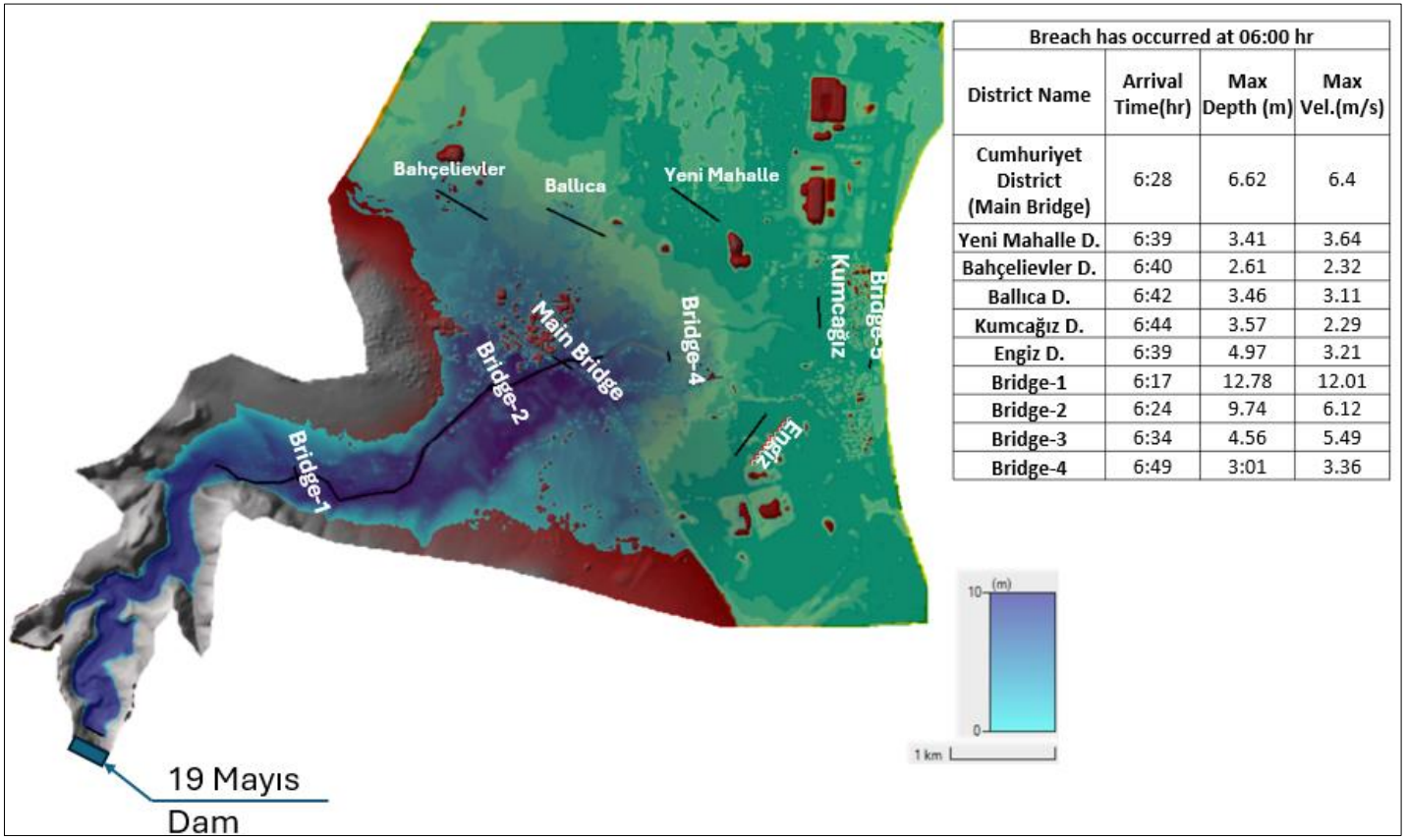

Breach has occurred at 06:00 hr			
District Name	Arrival Time(hr)	Max Depth (m)	Max Vel.(m/s)
Cumhuriyet District (Main Bridge)	6:28	6.62	6.4
Yeni Mahalle D.	6:39	3.41	3.64
Bahçelievler D.	6:40	2.61	2.32
Ballıca D.	6:42	3.46	3.11
Kumcağız D.	6:44	3.57	2.29
Engiz D.	6:39	4.97	3.21
Bridge-1	6:17	12.78	12.01
Bridge-2	6:24	9.74	6.12
Bridge-3	6:34	4.56	5.49
Bridge-4	6:49	3:01	3.36

Figure 5.19 Maximum water depth map in the Ondokuz Mayıs floodplain and a summary of the flood arrival times at important residential areas for the piping scenario (Scenario-2)

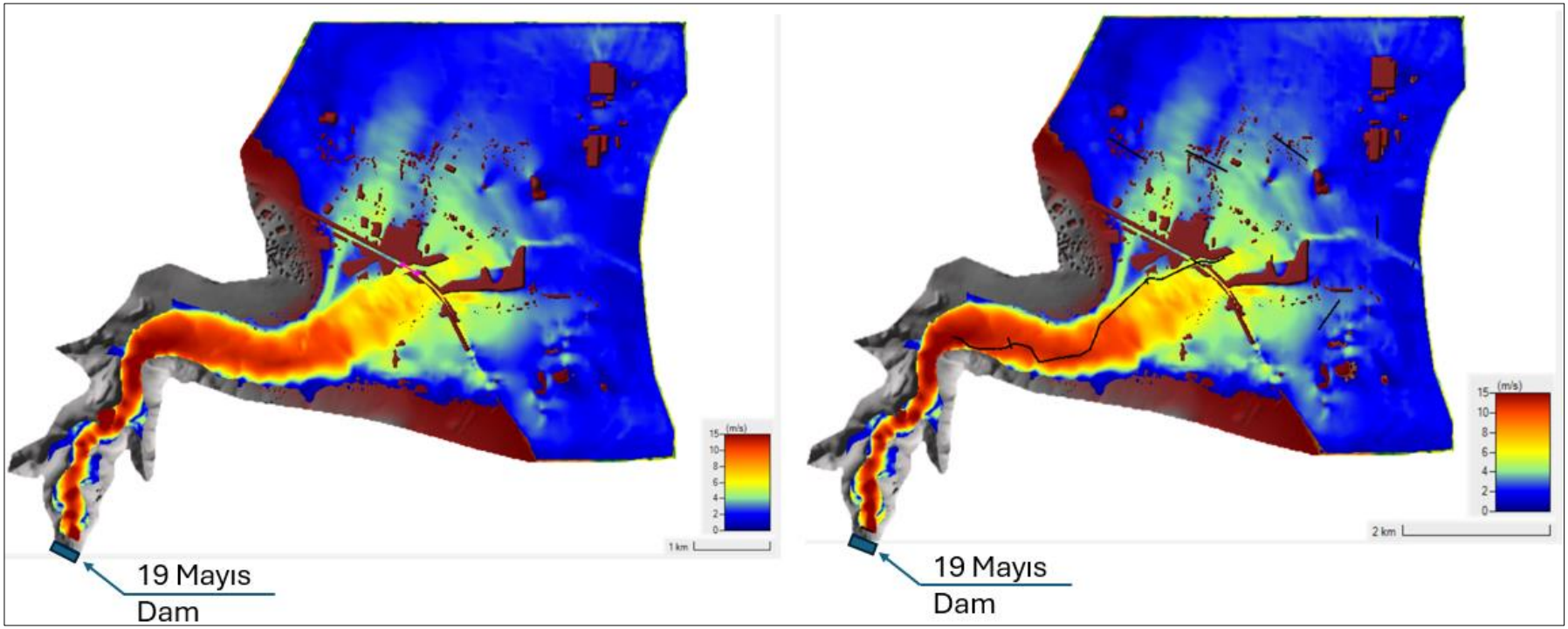

Figure 5.20 Maximum velocity distribution of Ondokuz Mayıs floodplain a) overtopping scenario b) piping scenario

In contrast, the piping scenario exhibits a more controlled and horizontal progression. The red and orange tones are concentrated in more limited areas, indicating lower flow velocities and a longer water-spreading time. In the piping scenario, the slower release of water results in longer travel times, but the discharge becomes more evenly distributed over time.

5.1.6 Inundation Maps for Ondokuz Mayıs Dam Breach

This section presents inundation maps obtained from each breach scenario. The inundation maps for the piping and overtopping scenarios reveal distinct flood propagation patterns and depth distributions. In both scenarios, large portions of the floodplain experience significant inundation. However, there are vital differences in the extent and severity of the flooding. Figure 5.21, and Figure 5.22 represent the maximum water depths recorded throughout the simulation period rather than a specific moment in time. The peak flood depths reached at different points during the event are reflected in these maps, illustrating how water accumulated in various regions for the piping and overtopping scenarios, respectively.

In the piping scenario (Figure 5.21), the flood seems to propagate more gradually, with higher water depths concentrated closer to the breach origin. This suggests that the water release in the piping failure mode leads to a slower but deeper water accumulation in certain areas, potentially posing severe risks to infrastructure near the breach's source. Furthermore, the velocity distribution patterns in such worst-case scenarios are critical for assessing flood dynamics. The maximum velocity distribution for these scenarios is provided in Appendix B.

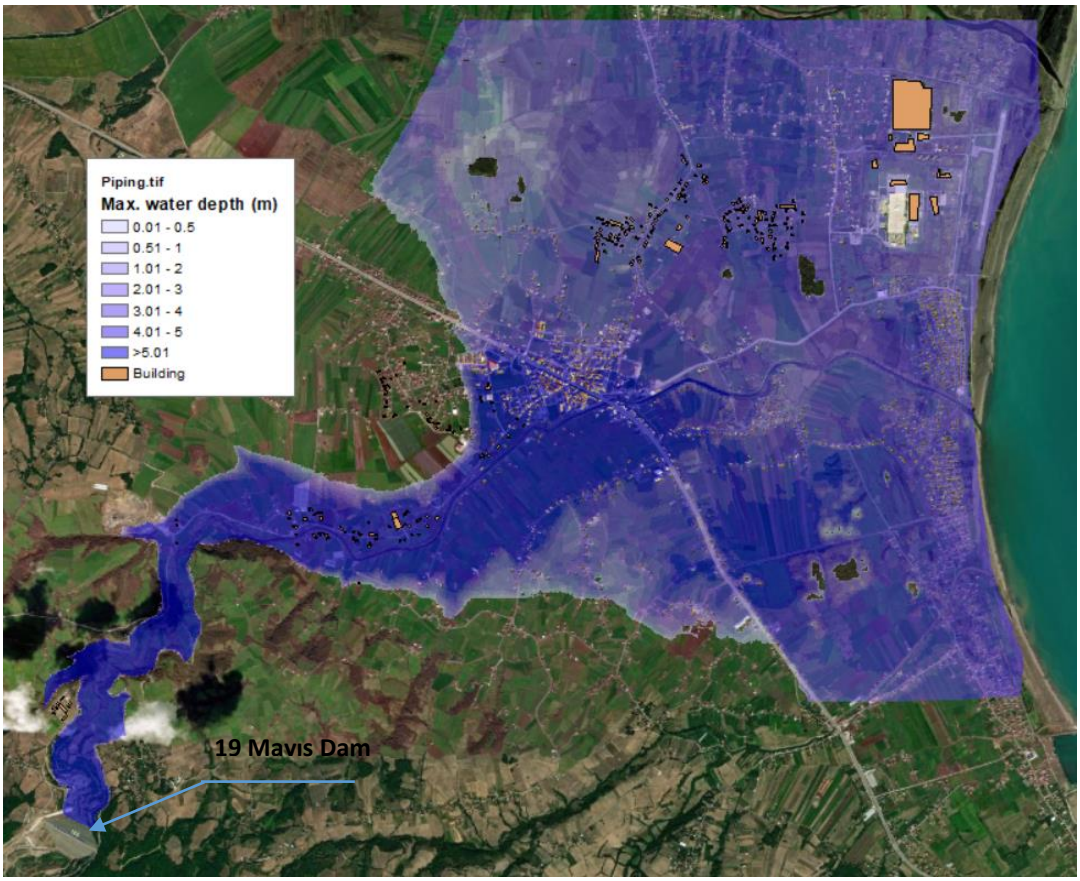

Figure 5.21 Maximum water depth map for piping scenario

On the other hand, the overtopping scenario (Figure 5.22) demonstrates a broader water spread across the floodplain, with floodwaters extending farther downstream. The water depths are generally lower in the overtopping scenario than in the piping scenario. This suggests that overtopping failure leads to faster water propagation but with less concentrated depths. Such a pattern indicates that overtopping can inundate a more extensive area more quickly, thereby increasing the exposure of distant regions to flood risks.

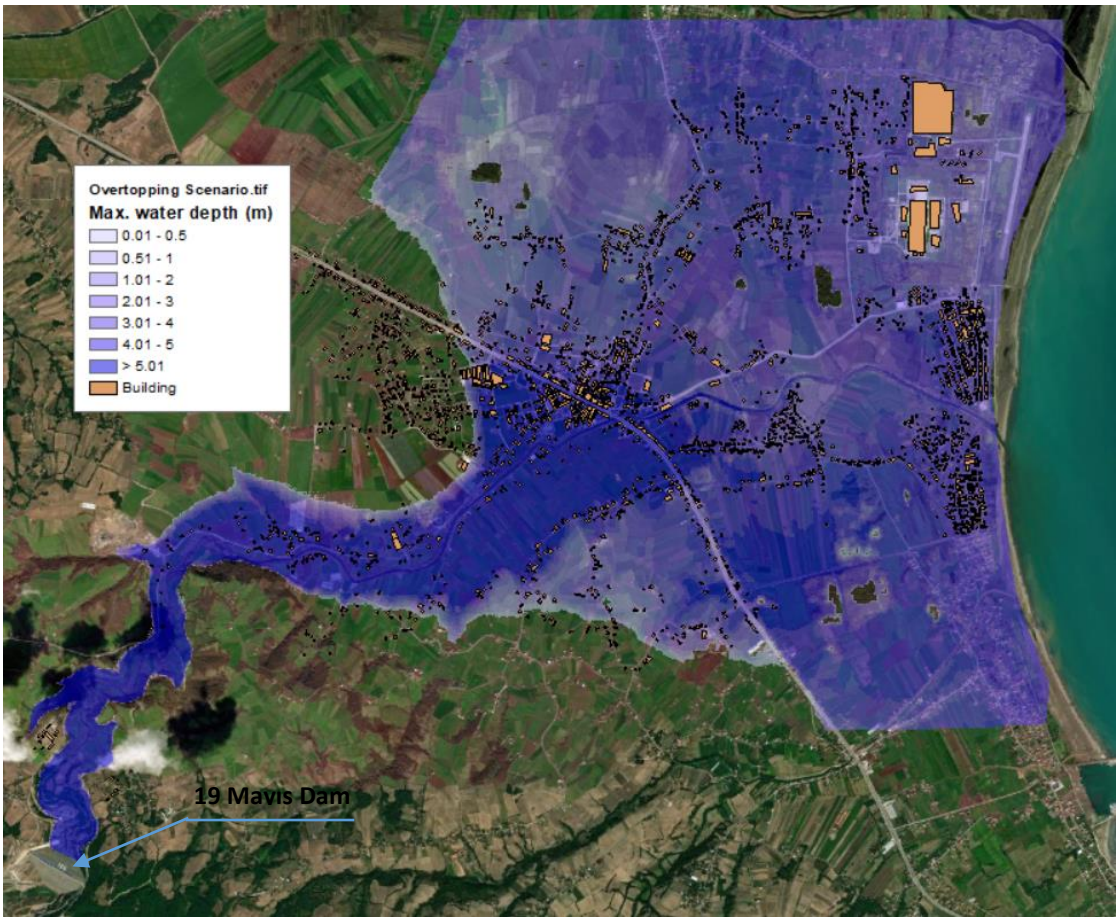

Figure 5.22 Maximum water depth for overtopping scenario

Water depth distribution maps and the patterns of water spread help us understand how flooding propagates and how buildings and infrastructure may be affected during failure scenarios such as piping or overtopping. Understanding this is crucial for making flood management more effective. This information can enable a focus on areas with deeper water accumulation in the case of piping or regions exposed to sudden inundation in the case of overtopping.

Figure 5.23 compares water depth results from two dam break scenarios, Scenario 1 (Overtopping) and Scenario 2 (Piping), across 1,000 randomly generated points.

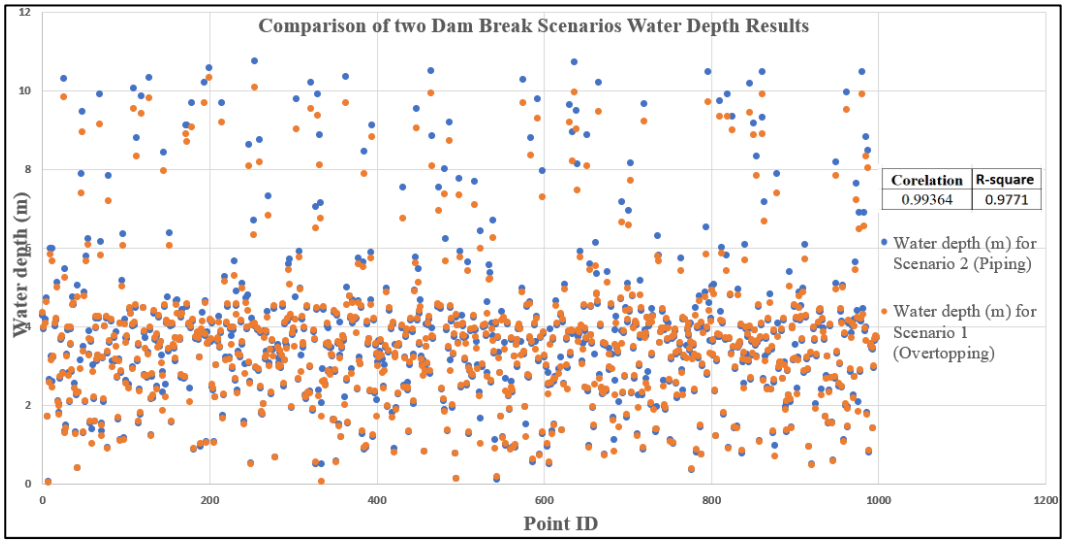

Figure 5.23 Comparison of two dam break scenarios for water depth results

As indicated by the high correlation (0.99364) and R-squared value (0.9771), the results from both scenarios are closely aligned. While the water depths are very similar at many points, there are some outliers where the two datasets diverge. Despite these variations, the average difference in water depth between the two scenarios is only 8 cm, demonstrating a close match overall.

5.1.7 Flood Hazard Maps for Ondokuz Mayıs Dam Breach

Flood hazard maps are essential for visualizing the extent and severity of potential flood events, such as the failure of the Ondokuz Mayıs Dam. These maps help identify vulnerable areas, assess risks to communities, and guide emergency

response efforts. The assessment of flood hazards is often conducted by considering flow depth and velocity. FEMA guidelines suggest using depth x velocity (D x V) to assess the hazard level for each affected area, Table 5.8. This metric helps determine potential risks to people and structures.

Table 5.8 Simplified flood depth and velocity severity raster symbolization categories for flood severity (FEMA, 2020).

Flood Severity Category	**Depth x Velocity Range (m²/sec)**
Low	< 0.2
Medium	0.2 – 0.5
High	0.5 – 1.5
Very High	1.5 – 2.5
Extreme	> 2.5

Considering the procedure mentioned above, spatially varied hazard maps were generated for the failure modes of the overtopping and piping scenarios, Figure 5.24 and Figure 5.25, respectively.

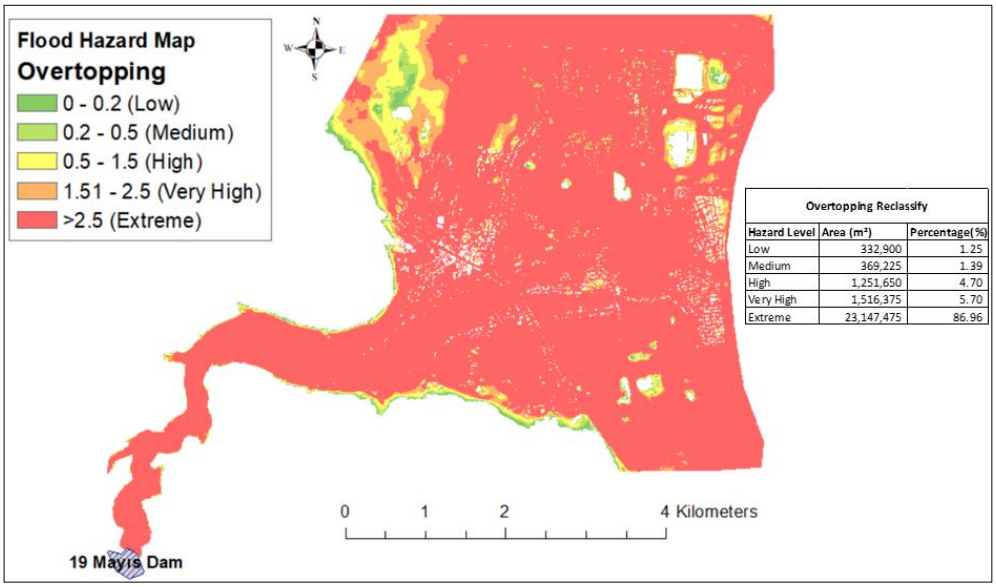

Figure 5.24 Spatially varied hazard classes for overtopping

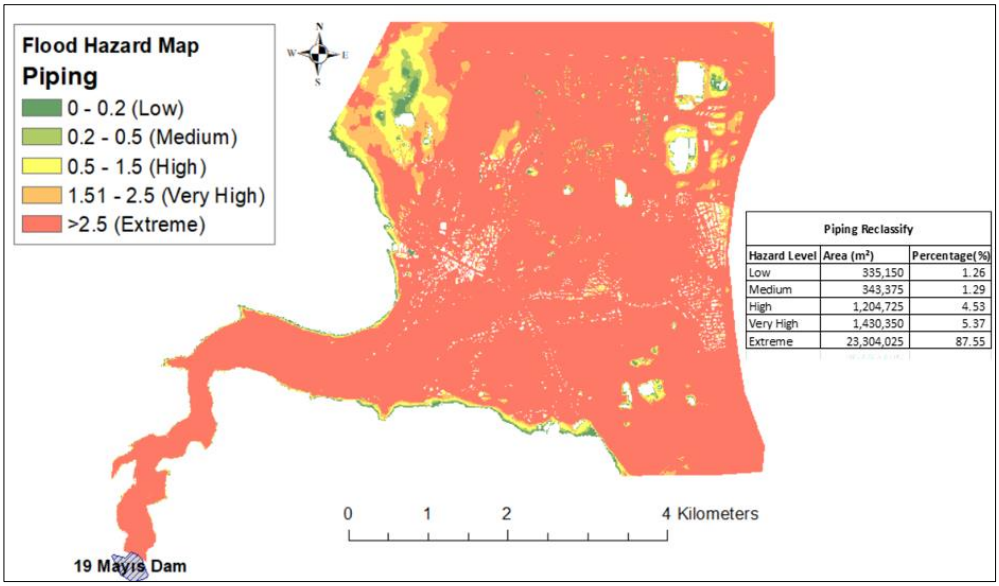

Figure 5.25 Spatially varied hazard classes for piping

In the overtopping scenario (Figure 5.24), the water disperses across a broader area, with most floodplains highlighted in red as a 'high' hazard. Only a few isolated locations exhibit 'very high' or 'extreme' hazard levels. This distribution indicates that the flood depths are relatively shallow, although the overtopping scenario facilitates rapid water movement.

In comparison, the piping scenario (Figure 5.25) reveals a slightly different flood distribution. Although the water spread covers a similar area to the overtopping scenario, a greater concentration of higher hazard levels is observed, particularly in regions marked in yellow and green. While the difference in the spatial extent of flooding may not be visually prominent, the percentage distribution of hazard levels exhibits a slight variation, as detailed in the accompanying table. This pattern suggests that water accumulates more deeply in certain areas, resulting in a slower yet more intense flood, consistent with the nature of a piping failure.

The values presented in the table show the percentage distributions of hazard levels derived from the reclassification process conducted using ArcGIS Software (Esri, 2019, Version 10.7).

5.1.8 Flood Damage Function

Evaluating potential flood damage is a critical part of effective flood risk management. One of the most commonly used tools for this purpose is depth-damage curves, which estimate the level of damage for specific water depths based on asset type or land-use category. Many countries have developed these curves by analyzing historical flood events and incorporating expert opinions. Although some early depth-damage curves were developed in Turkey by Yanmaz & Coşkun (2001), their use has remained limited due to the fact that they were applicable only to the site-specific local condition of the study. As stated by Yeğin (2015), past studies in Turkey have largely relied on depth-damage relationships with other countries, particularly those from Europe.

The report "Global Flood Depth-Damage Functions" prepared by Huizinga et al (2017) offers a global database of depth-damage functions for various asset categories. It aims to improve the consistency and reliability of flood risk assessments across regions, (Huizinga et al., 2017). The presented depth-damage functions were provided for 214 countries in residential buildings, commerce, industry, transport, infrastructure, and agriculture categories, Figure 5.26. The present study utilized these depth-damage functions to estimate the potential damage to buildings, roads, and agricultural land based on flood scenarios.

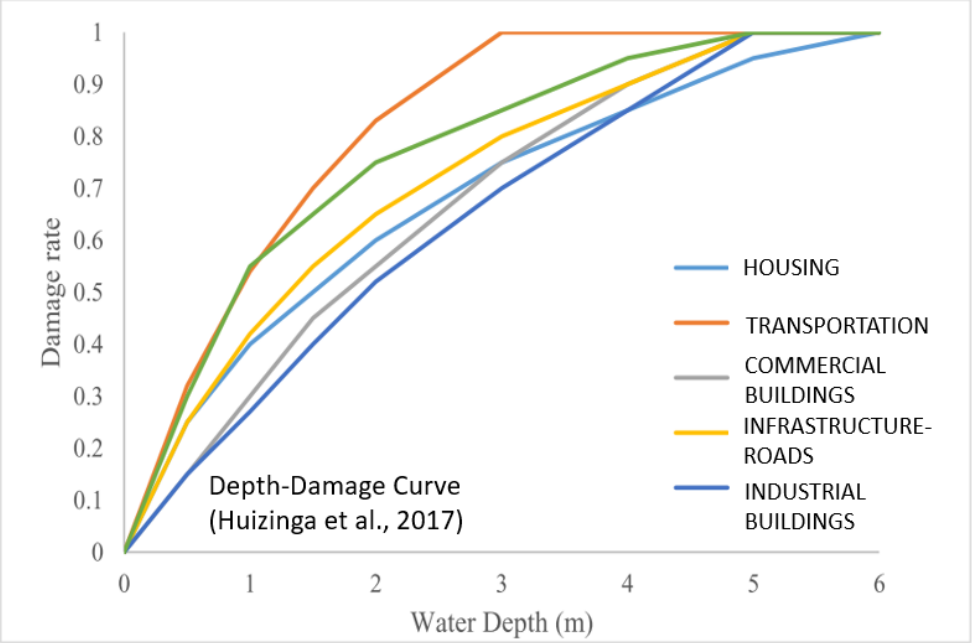

Figure 5.26.Damage factor for Europe for different asset categories, (Huizinga et al., 2017).

Given the limited availability of locally developed depth-damage curves in Turkey, this study employed the globally applicable depth-damage functions outlined by Huizinga et al. (2017). Throughout this study, the maximum water depths experienced by each structure in the flood area were measured using ArcGIS software, and these depths were translated into damage ratios using the depth-damage curve. This curve features water depth on the x-axis and the estimated percentage of structural damage on the y-axis. Utilizing this methodology, the potential flood damage for each building was precisely estimated, and economic cost calculations for each structure are detailed in Section 5.3

5.1.9 Flood Wave Arrival Times

Effective emergency planning requires careful consideration of flood timing, as precise predictions regarding flood wave arrival are essential for implementing successful mitigation measures. This study examines critical parameters, such as

flow depth, velocity, and hazard levels, for both overtopping and piping scenarios, with the flood arrival times at key control points.

The legend in Figure 5.27 represents the entire simulation duration (8 hours), whereas the legend in Figure 5.28 represents the duration from the post-breach period (after the 6th hour) until the flood reaches the center**.**

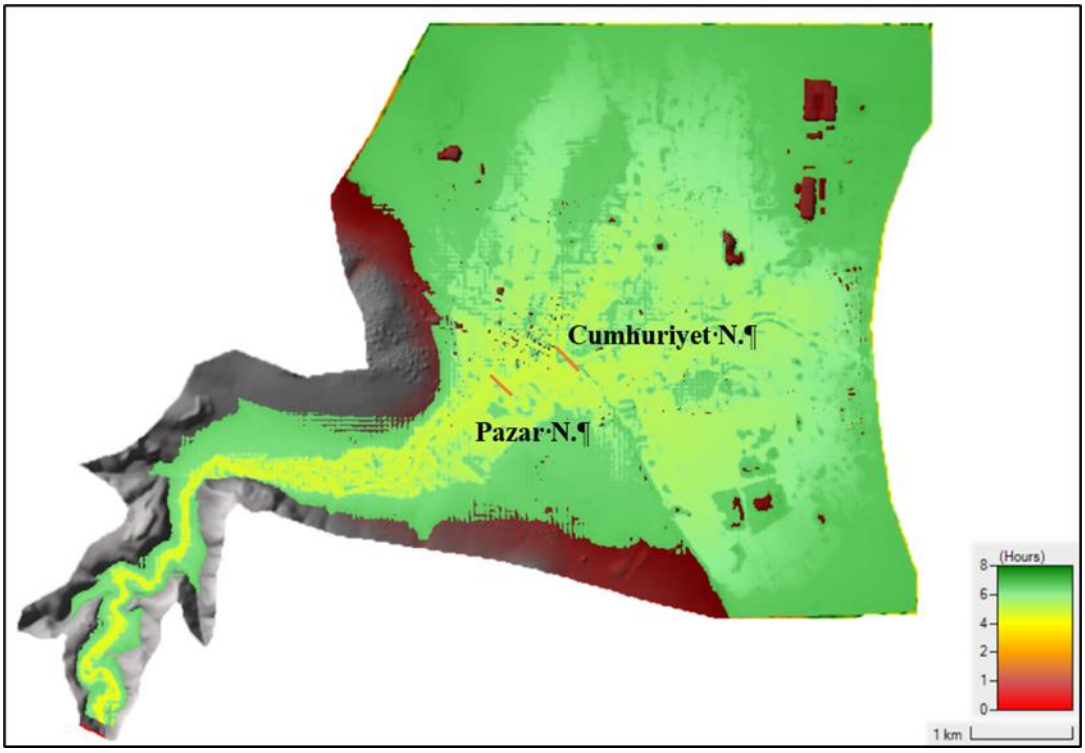

Figure 5.27 Flood arrival times for overtopping scenario

According to estimation, overtopping began at 6:00 AM in this scenario. As seen in Figure 5.28, flood waves arrived in Pazar and Cumhuriyet Neighborhoods approximately 16 and 21 minutes later at 6.25, respectively, following the failure. The light green areas indicate that distant neighborhoods have more time to take precautionary actions.

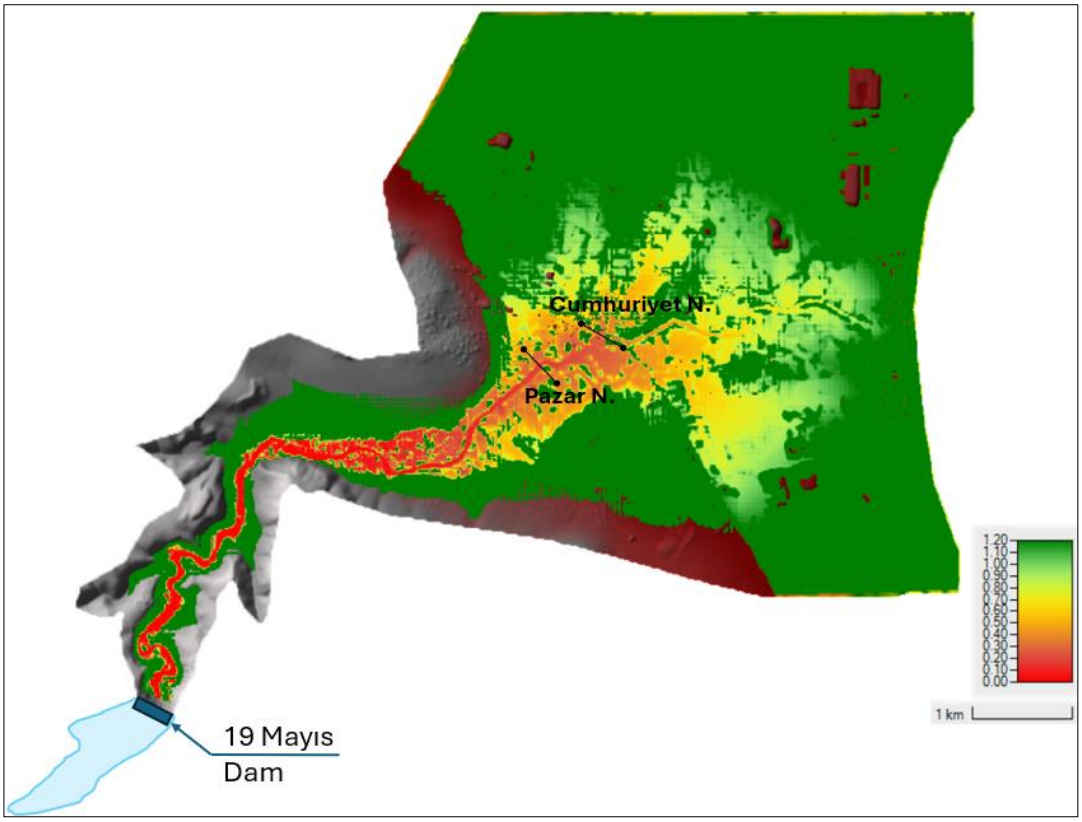

Figure 5.28 Flood arrival times after the occurrence of the overtopping event.

According to estimation, piping began at 0:00 AM in this scenario. As seen in Figure 5.29, in the piping scenario, after the failure, flood waves arrived in Pazar and Cumhuriyet Neighborhoods approximately 24 and 28 minutes later, respectively. The light green areas show that the distant neighborhoods had more time to take action.

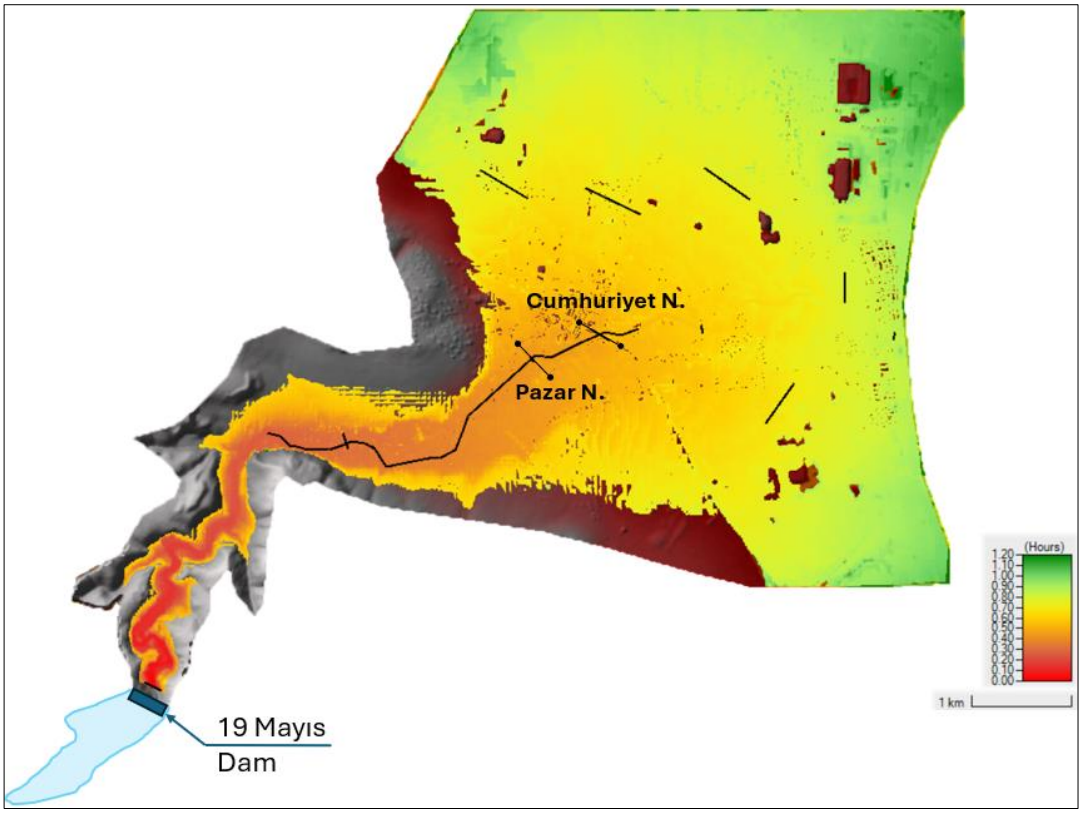

Figure 5.29 Flood arrival times for piping scenario

5.2 Calculated Damages

After obtaining flood propagation for the selected critical failure scenarios, damage percentages on structures, roads, and agricultural lands are determined based on flood depths using depth-damage functions provided in the literature. The modeling stages for determining damage percentages are schematically illustrated in Figure 5.30.

More specifically, Figure 5.30 illustrates the modeling stages conducted within the scope of this thesis to determine the damage rate caused by dam-break scenarios. It begins with simulating two failure scenarios: overtopping and piping, as represented in the breach outflow graph. These scenarios are then used to model flood propagation and water depth distribution across the affected area. Subsequently, a global depth-damage function is applied to assess the relationship between water depth and the extent of damage. The damage assessment is divided into three

categories: damage to buildings, roads, and agricultural land. Each category is mapped to visualize the spatial distribution of flood impact, providing a comprehensive understanding of potential damage across the region. In the following section, these maps are analyzed in detail to highlight specific areas at risk and the extent of the damage.

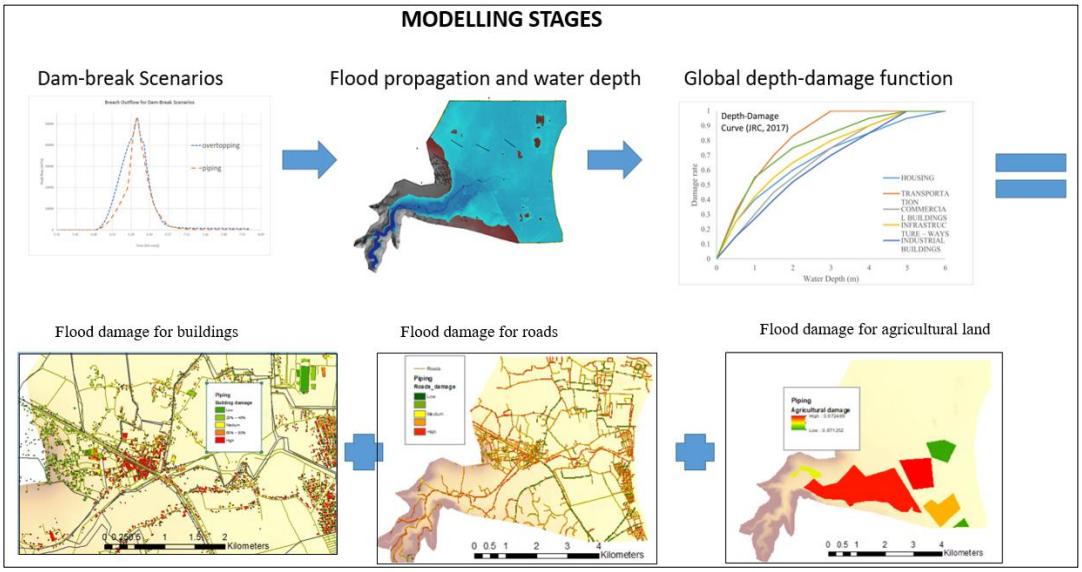

Figure 5.30 The modeling stages for determining the damage rate

5.2.1 Flood Damages for Buildings

Flood damage was calculated by applying depth-damage curves to each building based on the water depth observed during the piping scenario. The extent of damage was categorized into four levels—low, medium, high, and very high—reflecting the percentage of potential building damage. ArcGIS software /spatial analysis tools were used to overlay the flood extent with building locations, assigning damage levels accordingly.

The maps are shown in Figure 5.31 and Figure 5.32 for the piping and overtopping scenarios, respectively. The figures visually show the spatial distribution of building damage, calculated using depth-damage curves. These curves were applied to each building, correlating observed water depths with corresponding damage percentages, and the results were categorized into four levels: low, medium, high, and very high.

Using ArcGIS spatial analysis tools, the flood extent was overlaid with building locations, enabling the assignment of damage levels and the creation of these maps. Although the differences between the damage maps generated for these two scenarios may not be noticeable at first glance, they will become evident due to the economic analysis.

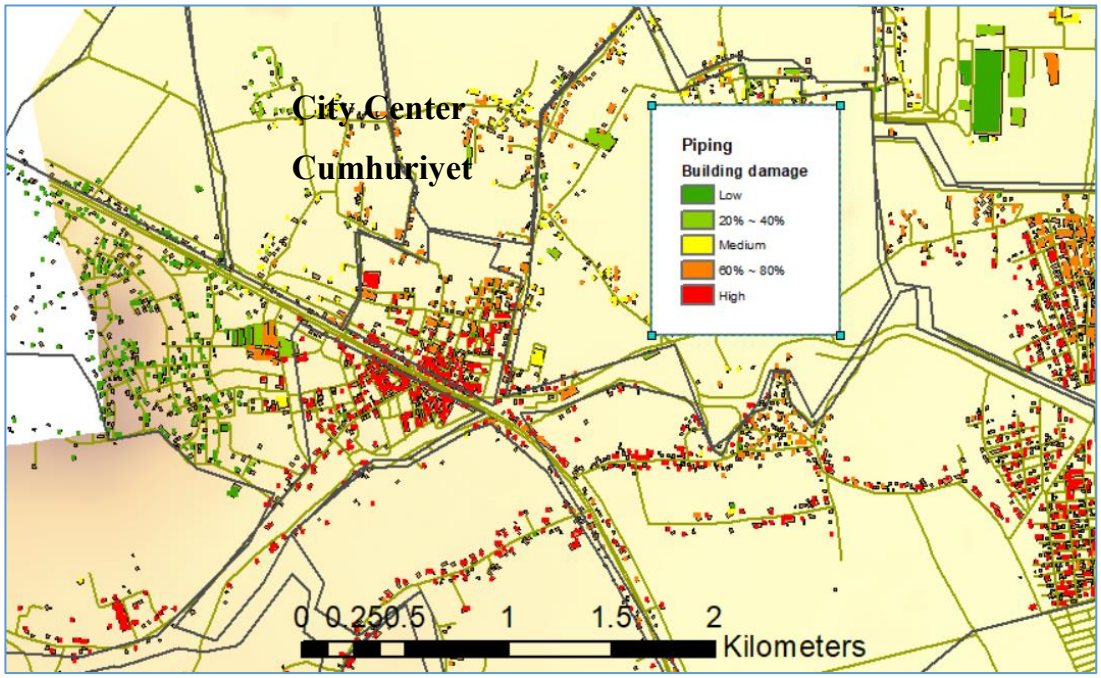

Figure 5.31 Building damage for piping scenario

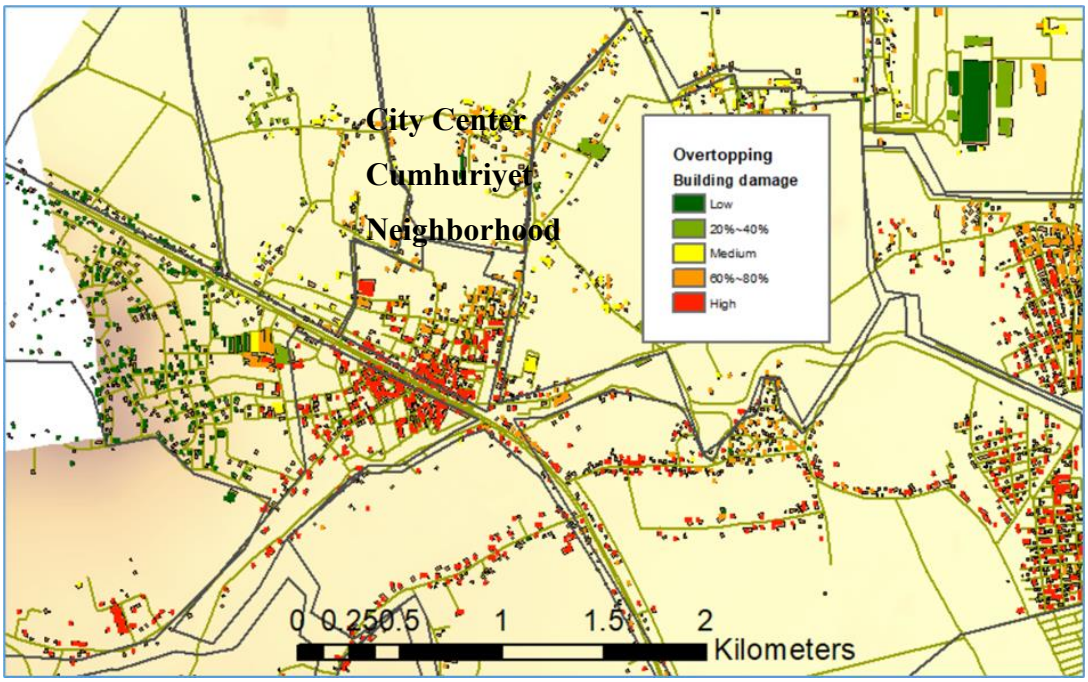

Figure 5.32 Building damage for overtopping scenario

The economic damages estimated for buildings under flood scenarios due to piping and overtopping are 7,313,221,914 TRY and 7,289,383,130 TRY, respectively. The results of analyses show that building damage was 83.0 % for the piping scenario and 82.6 % for the overtopping scenario.

5.2.2 Flood Damages for Roads

According to Huizinga et al. (2017), most flood events show that the contribution of damage to roads to total damage is approximately 4-18%, and road damage is lower in rural areas compared to urban areas.

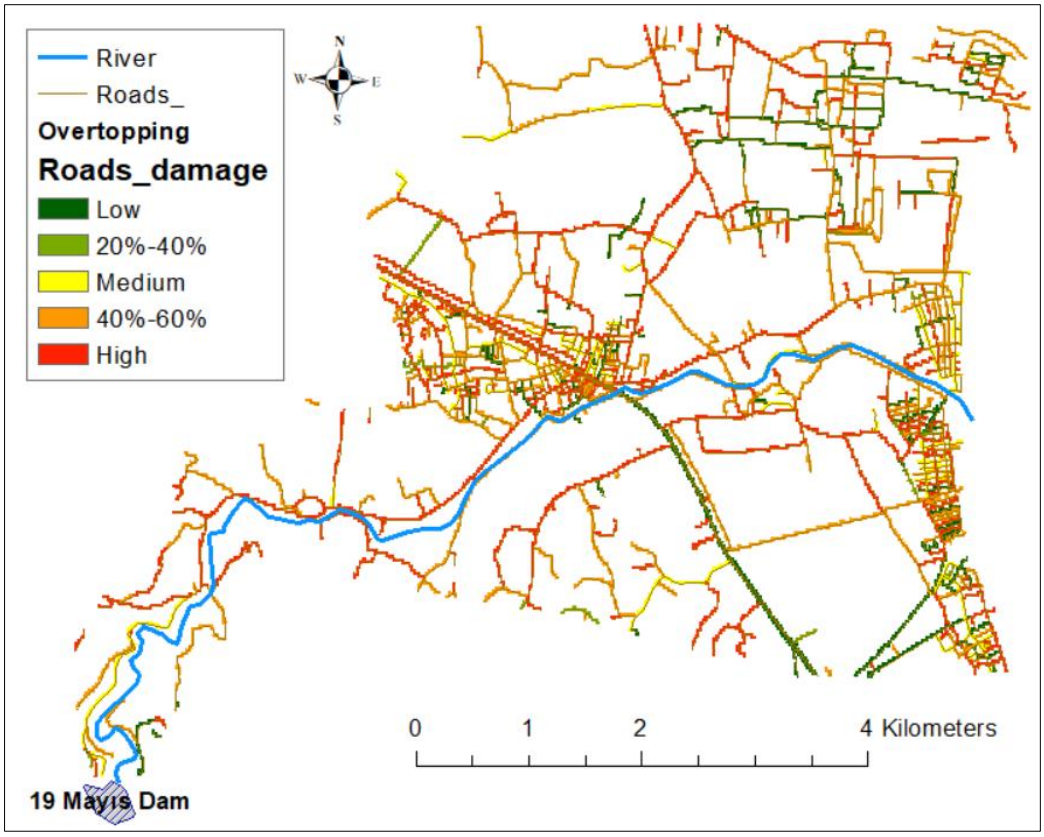

Figure 5.33 Road damage for overtopping scenario

The maps are shown in Figure 5.33 and Figure 5.34, for the road damage scenarios, the spatial distribution of road damage is visually represented and calculated using depth-damage curves. These curves were applied to each road segment, correlating observed water depths with corresponding damage percentages. The damage was classified into three levels: low, medium, and high. Using ArcGIS spatial analysis tools, the flood extent was overlaid with road network data, enabling the assignment of damage levels to different road segments and creating these maps.

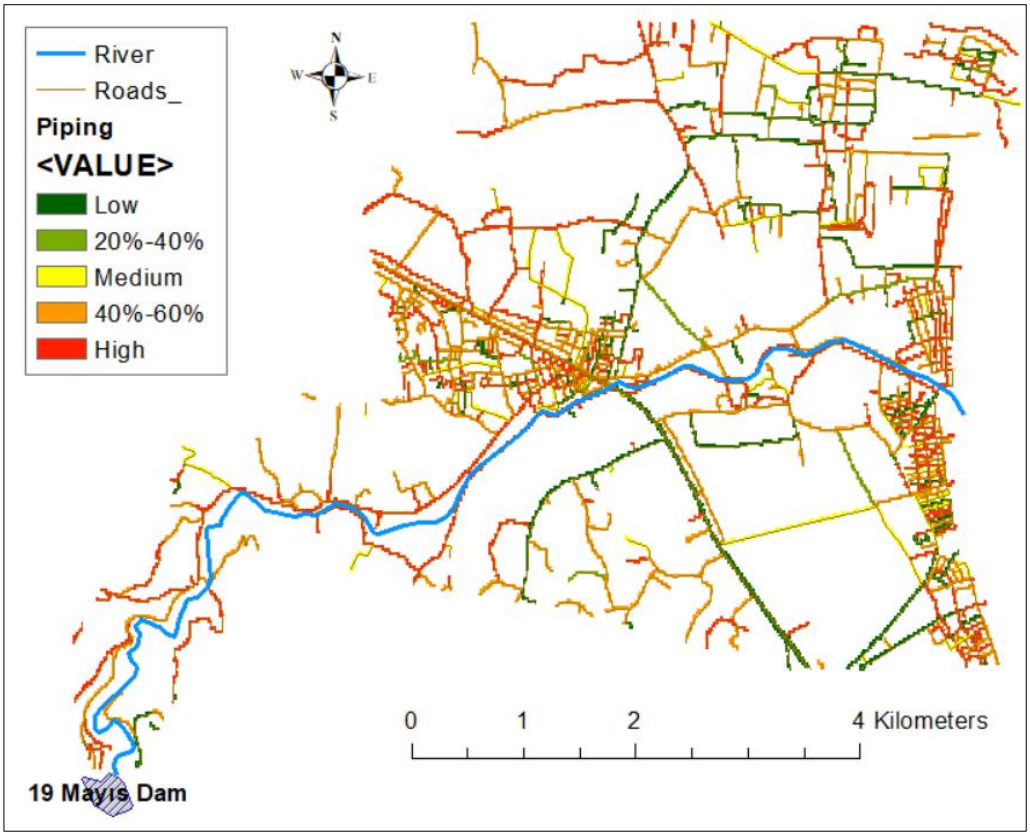

Figure 5.34 Road damage for piping scenario

The economic damages estimated for infrastructure under flood scenarios due to piping and overtopping are 1,367,184,161 TRY and 1,406,154,103 TRY, respectively. The results of analyses show that infrastructure damage was 15.518% for the piping scenario and 15.932% for the overtopping scenario.

5.2.3 Flood Damages for Agriculture

When the levels of agricultural damage between the piping and overtopping scenarios are compared, only a visible difference can be observed. The reflection of this difference was also evident in the economic analysis. According to Huizinga et al., (2017), for agriculture, the damage is related to a loss in output when floods destroy the yield. Figure 5.35 and Figure 5.36 illustrate the agricultural damage scenarios, visually representing the spatial distribution of agricultural damage calculated using depth-damage curves. High damage rates were observed based on

the damage percentages, assuming that crop losses would occur depending on the water depth resulting from the dam break.

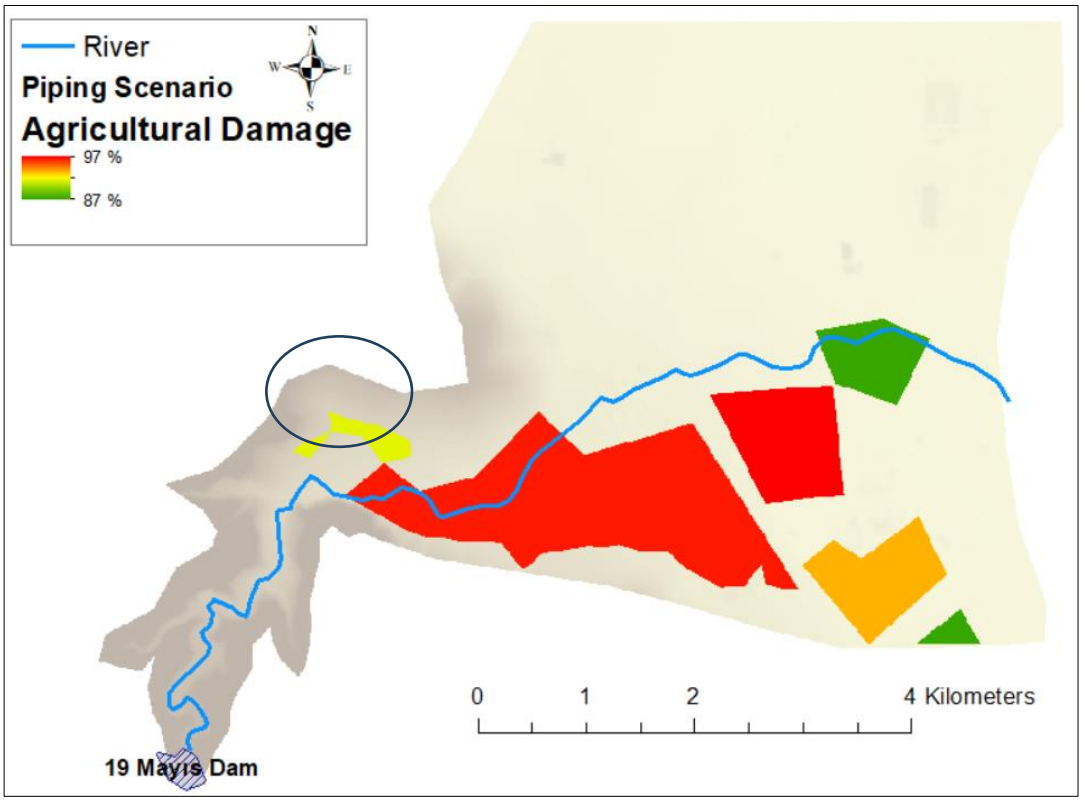

Figure 5.35 Agricultural damage for piping scenario

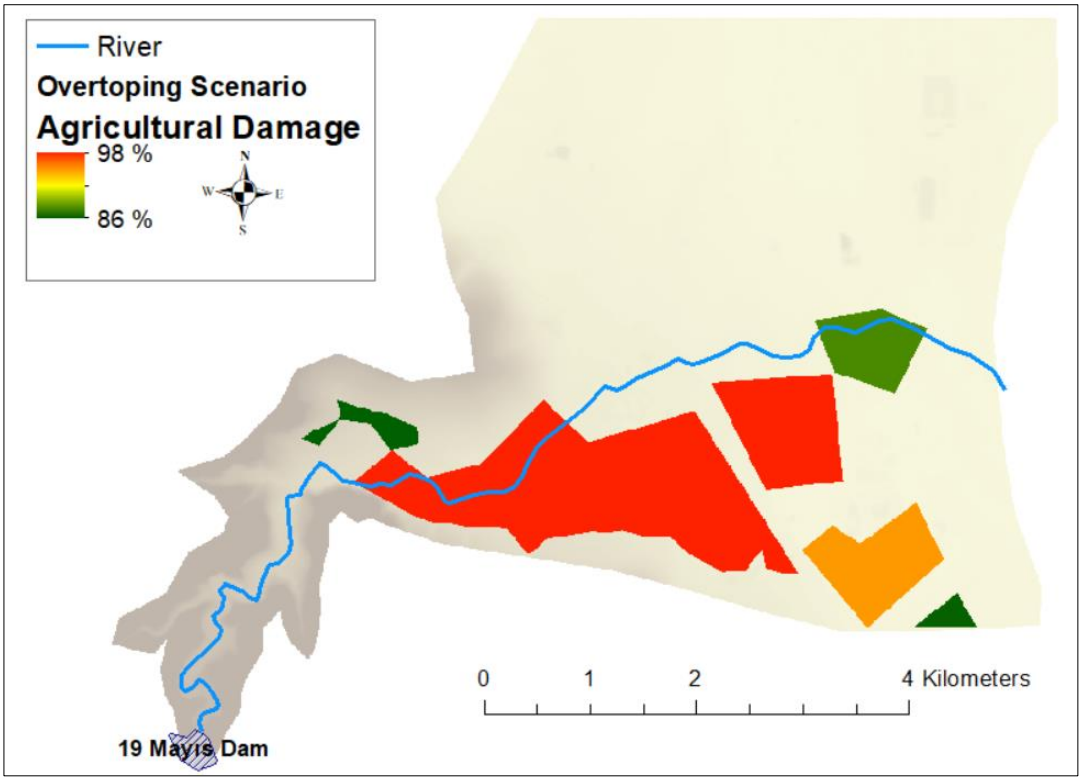

Figure 5.36 Agricultural damage for overtopping scenario

The agricultural area affected by the flood was 5,808,058 m² (5.8 km²). In section 3.3.6, it was calculated in Table 3.4 that the average income per square meter of crops cultivated in the Ondokuz Mayıs District. This section presents the economic damages estimated for agricultural areas under flood scenarios due to piping and overtopping as 130,279,781 TRY and 129,823,680 TRY, respectively.

5.3 Economical Cost Summary

The bar chart below in Figure 5.37 illustrates the economic losses across three categories—Agricultural Loss, Building Loss, and Infrastructure—for the overtopping and piping scenarios. Examining these distributions reveals that building damage accounts for the most considerable portion of total costs, followed by infrastructure, with agricultural losses being the smallest. This pattern aligns with the fact that buildings and infrastructure represent high-value assets that are more expensive to repair or replace. On the other hand, the total economic loss is

approximately similar in both scenarios, indicating that each scenario poses comparable financial risks.

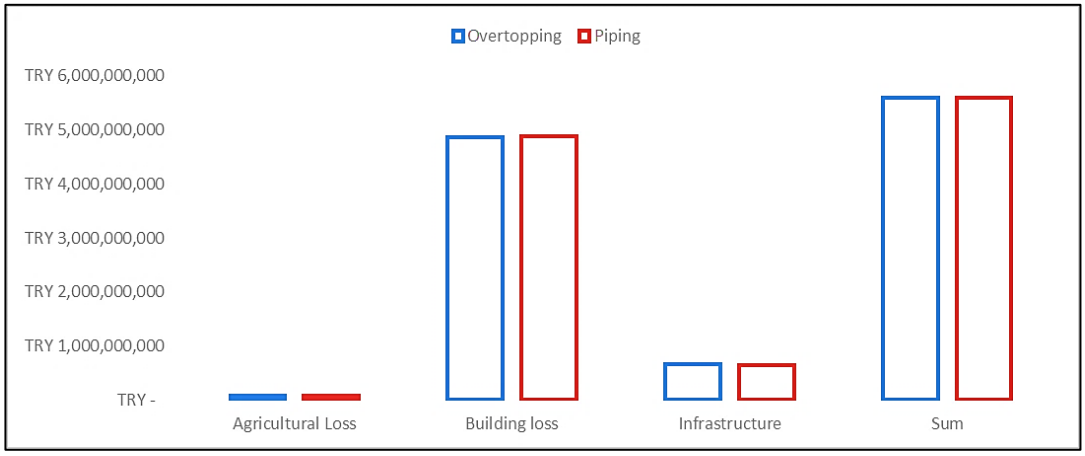

Figure 5.37 Comparison of costs of subcomponent

Given the high percentage of costs attributed to buildings and infrastructure, flood management strategies should prioritize protective measures for these assets. Infrastructure damage, though smaller than building loss, is still considerable. Although agricultural losses are present, their lower financial impact might indicate a relative resilience in agriculture or lower economic density in the affected areas compared to urban infrastructure.

Table 5.9 and Table 5.10 present the distribution of subcomponent costs and the economic costs of different failure scenarios. Flood risk management should focus on protecting buildings and infrastructure because they account for much of the total damage costs. While agricultural losses have less financial impact, they still affect the economy, particularly in rural areas. Although more minor than buildings, damage to infrastructure is still necessary and should be noticed.

Table 5.9 The economic cost for each failure scenario (1 $=34.36 TRY)

Scenarios				
	Overtopping		**Piping**	
Agricultural Loss	TRY	130,279,781	TRY	129,823,680
Building loss	TRY	7,289,383,130	TRY	7,313,221,914
Infrastructure	TRY	1,406,154,103	TRY	1,367,184,161
Sum (TRY)	TRY	8,825,817,014	TRY	8,810,229,755
Sum ($)	$	256,863,126	$	256,409,481

Table 5.10 Percentage distribution of subcomponent costs within total cost

Scenarios		
	Overtopping	**Piping**
	Percentage (%)	**Percentage (%)**
Agricultural Loss	1.48	1.47
Building loss	82.59	83.01
Infrastructure	15.93	15.52

CHAPTER 6

CONCLUSIONS AND FUTURE RECOMMENDATIONS

6.1 Summary of the Results and Conclusions

In this study, flood risks associated with the hypothetical failure of the Ondokuz Mayıs Dam were comprehensively assessed using advanced two-dimensional modeling techniques. Various failure scenarios, such as overtopping and piping, were analyzed to evaluate their impacts on downstream areas.

For Ondokuz Mayıs Dam, the effects of breach parameters, such as breach width, breach formation time, and side slopes on the outflow hydrographs were investigated. The findings show that breach formation time significantly influences both the maximum discharge (Q_p) and the time to reach peak discharge (T_p). Specifically, shorter formation times lead to higher peak discharges and reduced time-to-peak. Breach width was identified as another critical factor, with increases in width resulting in a notable rise in peak discharge. Conversely, variations on side slopes had relatively minor impacts on hydrograph characteristics. These results emphasize the importance of accurately estimating breach parameters, as they play a key role in determining flood dynamics, including peak discharge, arrival time, and inundation extent.

Different governing equations in the HEC-RAS 2D program were compared to evaluate their performance in simulating flood dynamics caused by dam failure. The strengths and weaknesses of the Diffusion Wave Equation (DWE) and Shallow Water Equation (SWE) methods were discussed, and the resulting water depth and velocity were compared. The results showed that the DWE method is fast and efficient for estimating overall flood extents. However, it struggles to capture sudden changes in water depth and velocity due to its simplified approach. In contrast, the SWE method provides more accurate and detailed results, especially in areas with sharp changes, such as high velocities, contractions, or expansions. Nevertheless, it

requires more computational power and time. These findings emphasize the importance of selecting the appropriate method based on the specific flood scenario and modeling objectives.

The sensitivity analysis of grid sizes demonstrated the significant impact of mesh resolution on computational performance. Using five different grid configurations (6.0 × 6.0 m, 7.5 × 7.5 m, 10 × 10 m, 25 × 25 m, and 50 × 50 m), water depths at 1000 randomly selected points across the flood map were analyzed using RMSE and R^2 statistical methods. The regional scale results showed that smaller grid sizes (6 × 6 m, 7.5 × 7.5 m, and 10 × 10 m) provided high accuracy with strong correlations ($R^2 > 0.999$) and low RMSE values. In comparison, although computationally efficient, the 50 × 50 m grid resulted in increased error (RMSE = 0.1388) and a slight reduction in water depth values. These findings align with previous studies, emphasizing the trade-off between accuracy and computational cost. In general, smaller grid sizes are recommended for detailed flood analyses, whereas larger grid sizes may be sufficient for preliminary assessments, provided a balanced approach is maintained.

The breach parameters were generated using Froehlich (1995, 2008), MacDonald and Langridge-Monopolis (1984), and Von Thun and Gillette (1990) methods to evaluate their influence on flood behavior. The peak flood discharges obtained from these methods were compared to assess their reliability and applicability. Froehlich's 2008 method provided balanced and accurate predictions, aligning closely with observed case studies in literature, while MacDonald and Langridge-Monopolis tended to underestimate peak discharge, and Von Thun and Gillette overestimated it. This comparative analysis emphasized the importance of selecting an appropriate breach prediction method to ensure precise flood modeling and risk assessment.

Failure likelihood assessments were conducted to evaluate the potential risks associated with various dam breach scenarios. The results indicated that the dam is safe against backward erosion piping and heave under current conditions, with safety factors exceeding the recommended thresholds, confirming the stability of both the dam body and foundation.

To assess the performance of the existing design, the downstream slope was adjusted from 2.0H/1.0V to 2.6H/1.0V. A probabilistic slope stability analysis was conducted using the Strength Reduction Factor (SRF) method combined with Monte Carlo Simulations (MCS) to evaluate failure risks under varying material strength conditions. The SRF method involved the gradual reduction of the shear strength parameters of dam materials to determine critical stability conditions. The analysis identified the most critical slip circle on the downstream slope under the operational earthquake scenario, with failure probabilities calculated for both slope configurations. Modifying the downstream slope inclination from 2.0H/1.0V to 2.6H/1.0V was considered to mitigate failure risk and meet safety criteria.

An economic analysis was conducted to examine the relationship between stability improvements and financial implications across six slope configurations. (2.0H/1.0V ~ 2.6H/1.0V) While the original slope design exhibited a higher failure probability, modifications significantly enhanced stability and reduced the likelihood of failure. Although increasing the slope inclination resulted in additional construction costs, a net benefit analysis demonstrated that the reduction in failure risks outweighed these expenses.

The analysis further revealed that the benefit/cost ratio is highest at the 2.2H/1.0V slope, identifying it as the most strategic configuration where return on investment is maximized. Consequently, this slope was the optimal choice for ensuring economic efficiency and long-term dam safety. These findings emphasize the importance of risk-based decision-making in dam design to achieve a balance between safety and cost-effectiveness.

For the Ondokuz Mayıs Dam, updated hydrological data, including revised rainfall and flow records obtained from the DSI database, enhanced the reliability of flood discharge calculations and reservoir management strategies. These updates helped identify potential overtopping risks and optimize spillway operations to improve dam safety.

Flood damages were calculated for various scenarios, including overtopping and piping failure modes. Four scenarios were initially developed based on Froehlich

breach parameters: Scenarios 1 and 3 represented overtopping failures (rainy days), while Scenarios 2 and 4 represented piping failures (sunny days). The analysis of high-outflow hydrographs generated from the breach identified Scenario 1 (overtopping) and Scenario 2 (piping) as the worst-case scenarios.

Comparisons and damage calculations were subsequently performed using these worst-case scenarios. In Scenario 1 (overtopping), the flood wave propagated more quickly, reaching the city center and nearby neighborhoods in a shorter time. However, in Scenario 2 (piping), the flood resulted in slightly higher water depths and larger inundation areas. This highlights the critical importance of accurately estimating breach parameters, as they directly influence flood dynamics and the extent of damages. These findings emphasize the need for effective flood risk mitigation strategies tailored to different failure mechanisms.

The economic impact was evaluated using direct loss estimates for residential areas, roads, and agricultural lands based on flood depths and extents. The piping scenario caused the most significant damage, with residential buildings experiencing the highest losses. These results highlight the necessity of accurate flood modeling to prioritize mitigation strategies effectively.

Overall, this study highlights the importance of integrating updated hydrological data, detailed geotechnical evaluations, and optimized modeling approaches into flood risk management strategies. By addressing potential weaknesses in material properties and enhancing slope stability, the dam's safety can be improved, thereby minimizing risks to downstream communities.

6.2 Future Study and Recommendations

While the analyses in this study provide valuable insights, there are several avenues for future research to build on these findings. Incorporating additional breach parameters, such as material heterogeneity and dynamic breach formation processes, could enhance the accuracy of outflow predictions. Additionally, with the increasing frequency of extreme weather events, integrating climate change scenarios into flood modeling would allow for more realistic risk assessments.

Furthermore, the incorporation of real-time monitoring systems, such as sensor-based networks tracking e

, deformation, and pore pressure, represents a crucial area for future research. These systems are vital for providing data that can significantly improve early warning systems and predictive models. Ensuring the safety of dams also demands that operational strategies include continuous monitoring of meteorological data. Establishing a system that regularly updates weather information is essential. During predicted continuous rainfall, proactive management of reservoir levels is critical to prevent overtopping or structural damage, safeguarding downstream communities, agriculture, and infrastructure while enhancing water resource management under varying climatic conditions.

In contemporary studies, dam-break analyses for dams in the design phase are typically conducted based on hypothetical worst-case failure scenarios, and flood risk management strategies are developed accordingly. However, as demonstrated in the present study, thoroughly examining the likelihood of hypothetical dam failure scenarios and supporting these probabilities with robust analyses can significantly enhance such studies' scientific accuracy and reliability.

Several key questions must be addressed in this context: Is the spillway capacity genuinely insufficient? Could an overtopping event occur? Are the material strength properties of the dam body as low as assumed? Is there a realistic potential for piping to develop? Furthermore, do geotechnical analyses reveal foundational erosion risks that could compromise dam stability? Addressing these questions through

comprehensive and detailed investigations would make dam failure analyses more reliable and scientifically grounded.

In the context of hydraulic analyses, calculating flood damages caused by dam failure requires detailed modeling techniques. This study emphasizes the importance of three-dimensional modeling of structures on maps for calculating flood damages caused by dam failure from a hydraulic perspective. Adopting a three-dimensional structure modeling approach is strongly recommended for future hydraulic analyses to enhance the accuracy and reliability of such studies.

The detailed analyses conducted in this study's flood damage assessment section serve as a reference for similar future studies. This study adopted the equivalent floor density approach at the neighborhood scale as a simplification to facilitate the analysis. However, conducting on-site investigations in smaller flood-prone areas and classifying all buildings in detail based on their floor distribution would undoubtedly yield more precise economic results in flood damage assessments.

However, one of Turkey's significant limitations in flood damage assessments is the absence of depth-damage curves. These curves play a crucial role in defining the relationship between flood depth and economic losses for different land uses, significantly improving the accuracy of flood risk evaluations. Most existing studies rely on international datasets; however, these do not fully reflect the local construction standards, economic conditions, and, most importantly, the highly variable topography of the country. Therefore, future research should focus on developing province-level depth-damage curves by utilizing data from past flood events, insurance records, and field surveys. Establishing a comprehensive dataset tailored to Turkey’s urban, rural, and industrial areas would enhance the reliability of flood damage estimations, support cost-benefit analyses, and contribute to more effective disaster risk management strategies.

Finally, to ensure dam safety, it is essential to remember that real-time reservoir operations depend on continuous monitoring of meteorological data. A system should be established that regularly receives updated weather information. When forecasts predict ongoing rainfall, it is advisable to lower reservoir levels in advance

to manage the incoming water volume and prevent any risk of overtopping or structural damage. This proactive measure not only helps avoid downstream flooding—protecting communities, agriculture, and infrastructure—but also improves the management of water resources, adapting efficiently to changing weather conditions.

In future studies, exploring the potential damages inflicted on downstream structures by rock materials transported in the aftermath of a dam failure would be valuable. As the breakdown of a dam can release significant quantities of rock and debris, understanding how these materials interact with and impact man-made structures such as bridges, roads, and levees is crucial. Additionally, conducting field studies in areas historically affected by dam failures could provide valuable empirical data on the impacts of transported rock materials. This type of research could be particularly beneficial in regions prone to extreme hydrological events, where the integrity of aging dams and the safety of downstream communities are continuously at risk.

REFERENCES

Alonso, R., Santillana, M., & Dawson, C. (2008). On the diffusive wave approximation of the shallow water equations. *European Journal of Applied Mathematics, 19*(5), 575–606. https://doi.org/10.1017/S0956792508007675.

Alppay, H. (2019). Dam failure flood risk assessment (Master's thesis). Sakarya University, Graduate School of Natural and Applied Sciences, Sakarya, Turkey.

Association of State Dam Safety Officials (ASDSO). (2021). *Dam failure and incident investigation guide.* Retrieved from https://damsafety.org/ManualsandGuidelines.

Apel, H., Aronica, G. T., Kreibich, H., & Thieken, A. H. (2009). Flood risk analyses: How detailed do we need to be? *Natural Hazards, 49*(1), 79–98. https://doi.org/10.1007/s11069-008-9277-8.

Ashraf, A. (2021). *Numerical investigation of 2D dam-break failures by using GIS applications* (Doctoral dissertation, Middle East Technical University, Ankara, Turkey).

Baecher, G. B., Pate, M. E., & de Neufville, R. (1980). *Risk of dam failure in benefit-cost analysis.* Water Resources Research, 16(3), 449–456. https://doi.org/10.1029/WR016i003p00449.

Beden, N., & Ulke, A. (2021). Estimation of the local financial costs of flood damage with different methodologies in Unye (Ordu), Turkey. *Natural Hazards, 108*(3), 2835–2854. https://doi.org/10.1007/s11069-021-04802-w.

Bellos, V. (2012). Ways for flood hazard mapping in urbanized environments: A short literature review. Water Utility Journal, 4, 25–31. Retrieved from https://www.researchgate.net/publication/260298638.

Bellos, V., & Tsakiris, G. (2015). *Comparing various methods of building representation for 2D flood modelling in built-up areas*. Water Resources Management, 29(2), 379–397. https://doi.org/10.1007/s11269-014-0702-3.

Beretta, R., Ravazzani, G., Maiorano, C., & Mancini, M. (2018). Simulating the influence of buildings on flood inundation in urban areas. Geosciences, 8(2), 77. https://doi.org/10.3390/geosciences8020077.

Bernard-Garcia, Mayari & Mahdi, Tew-Fik. (2022). Review and Updated Guidance for Embankment Overtopping Dam Breach Dimensions. 631-641. 10.1007/978-981-19-1065-4_52.

Bowles, J. E. (1997). Foundation analysis and design (5th ed.). McGraw-Hill.

Bozkuş, Z., & Kasap, A. (1998). Comparison of physical and numerical dam-break simulations. *Turkish Journal of Engineering and Environmental Sciences, 22*(5), 429–443.

Bozkuş, Zafer & Güner, Ali. (2001). Pre-Event Dam Failure Analyses for Emergency Management. 25. 627-641.

Bozkuş, Z., & Bağ, F. (2011). Virtual failure analysis of the Çınarcık Dam. Journal of Civil Engineering, 22(4), 1537–1549.

Brown, J. D., Spencer, T., & Moeller, I. (2007). Modeling storm surge flooding of an urban area with particular reference to modeling uncertainties: A case study of Canvey Island, United Kingdom. Water Resources Research, 43(6), W06402. https://doi.org/10.1029/2005WR004597.

Brunner, G. W., Piper, S. S., Jensen, M. R., & Chacon, B. (2015). Combined 1D and 2D hydraulic modeling within HEC-RAS. Proceedings of the World Environmental and Water Resources Congress 2015: Floods, Droughts, and Ecosystems, 1432–1443. American Society of Civil Engineers. https://doi.org/10.1061/9780784479162.143.

Brunner, G. W. (n.d.). Diffusion wave vs full momentum (SWE). U.S. Army Corps of Engineers Hydrologic Engineering Center. https://www.hec.usace.army.mil/confluence/rasdocs/r2dum/latest/running-a-model-with-2d-flow-areas/shallow-water-or-diffusion-wave-equations.

Brunner, G. W. (2016). *HEC-RAS river analysis system hydraulic reference manual* (Version 5.0). U.S. Army Corps of Engineers, Hydrologic Engineering Center. Retrieved from https://www.hec.usace.army.mil.

Budhu, M. (2015). Soil mechanics and foundations (3rd ed.). John Wiley & Sons.

Çalamak, M. (2017). Tanyeri Barajı örneğinde barajların taşkın nedeniyle üstten aşma güvenilirliğinin belirlenmesi. *Gazi Üniversitesi Mühendislik-Mimarlık Fakültesi Dergisi, 32*(3), 965–975. https://doi.org/10.17341/gazimmfd.337652.

Çalamak, M., Yanmaz, A. M., & Kentel, E. (2017). Probabilistic evaluation of the effects of uncertainty in transient seepage parameters. Journal of Geotechnical Engineering, 143(1), 23–45. https://doi.org/10.1061/(ASCE)GT.1943-5606.0001739.

Çalamak, M., Yılmaz, A., & Yanmaz, A. M. (2018). Performance evaluation of internal drains of earthen dams. Journal of Geotechnical Engineering, 144(2), 45–67. https://doi.org/10.1061/(ASCE)CF.1943-5509.0001232.

Çalamak, M., & Yanmaz, A. M. (2018). Assessment of core-filter configuration performance of rock-fill dams under uncertainties. Journal of Geotechnical Engineering, 144(3), 12–20. https://doi.org/10.1061/(ASCE)GM.1943-5622.0001114.

Çetin, K. Ö. (2015). Dolgu barajlar için sismik tasarım ve performans kriterleri [Seismic design and performance criteria for earthfill and rockfill dams]. In IV. Ulusal Baraj Güvenliği Sempozyumu, 9–11 Ekim 2014, Fırat Üniversitesi, Elazığ. Retrieved from https://www.researchgate.net/publication/282644288.

Charles, J. A., Tedd, P., & Warren, A. (2011). Lessons from historical dam incidents. Environment Agency. ISBN: 978-1-84911-232-1.

CivilGEO. (n.d.). HEC-RAS 2D computational equations comparison. Retrieved December 16, 2024, from https://knowledge.civilgeo.com/hec-ras-2d-computational-equations-comparison/.

Daily Sabah. (2024, November 25). *Torrential rain causes severe flooding in Türkiye's Samsun*. Retrieved from https://www.dailysabah.com/turkiye/torrential-rain-causes-severe-flooding-in-turkiyes-samsun/news.

Das, M. (2010). *Principles of geotechnical engineering* (7th ed.). Cengage Learning.

DSI. (2011). Ondokuz Mayıs Dam Planning Report. State Hydraulics Works, Ankara, Turkey.

DSI. (2013). Ondokuz Mayıs Dam Final Project Reports. State Hydraulics Works, Ankara, Turkey.

Ekmekçioğlu, Ö. (2022). Comprehensive flood risk assessment and identification of the potential flood mitigation strategies (Doctoral dissertation). Istanbul Technical University, Department of Civil Engineering, Hydraulics and Water Resources Engineering Programme, Istanbul, Turkey.

Esri. (2019). *ArcMap (Version 10.7) [Software]*. Esri Inc. Retrieved from https://www.esri.com.

Falter, D., Vorogushyn, S., Lhomme, J., Apel, H., Gouldby, B., & Merz, B. (2013). Hydraulic model evaluation for large-scale flood risk assessments. *Hydrological Processes, 27*(9), 1331–1340. https://doi.org/10.1002/hyp.9553.

Federal Emergency Management Agency (FEMA). (2020). Guidance for flood risk analysis and mapping: Flood depth and analysis rasters (Guidance Document 14). Retrieved from https://www.fema.gov/flood-maps/guidance-partners/guidelines-standards.

Fell, R., MacGregor, P., Stapledon, D., & Bell, G. (2005). Geotechnical engineering for dams. Taylor & Francis Group.

Froelich, D. (1995a). Embankment dam breach parameters revisited. Journal of Water Resources Planning and Management, 121(1), 90-97.

Froehlich, D. C. (1995b). Peak outflow from breached embankment dam. Journal of Water Resources Planning and Management, 121(1), 90–97.

Froehlich, D. C. (2008). Embankment dam breach parameters and their uncertainties. Journal of Hydraulic Engineering, 134(12), 1708–1721. https://doi.org/10.1061/(ASCE)0733-9429(2008)134:12(1708).

Froehlich, D. C. (2016). Empirical model of embankment dam breaching. In G. Constantinescu, M. Garcia, & D. Hanes (Eds.), *River Flow 2016* (pp. 1821–1829). CRC Press. https://doi.org/10.1201/9781315644479-285.

Graham, W. J. (1999). A procedure for estimating loss of life caused by dam failure (DSO-99-06). U.S. Department of the Interior, Bureau of Reclamation, Dam Safety Office. https://www.usbr.gov.

Garai, J. (2016). Hydraulic failure by heave and piping. University of Debrecen, College of Engineering, Department of Civil Engineering.

Griffiths, D. V., & Fenton, G. A. (1997). Extreme hydraulic gradient statistics in stochastic earth dam. *Journal of Geotechnical and Geoenvironmental Engineering, 123*(11), 995–1000. https://doi.org/10.1061/(ASCE)1090-0241(1997)123:11(995).

Guinot, V. (2012). Multiple porosity shallow water models for macroscopic modelling of urban floods. *Advances in Water Resources, 37,* 40–72. https://doi.org/10.1016/j.advwatres.2011.11.002.

Haltaş, İ., Tayfur, G., & Elçi, Ş. (2016). Two-dimensional numerical modeling of flood wave propagation in an urban area due to Ürkmez dam-break, İzmir, Turkey. *Natural Hazards, 81*(3), 2103–2119. https://doi.org/10.1007/s11069-016-2175-6.

Hoek, E., & Brown, E. T. (1980). Empirical strength criterion for rock masses. *Journal of Geotechnical and Geoenvironmental Engineering, 106*(9), 1013-1035. https://doi.org/10.1061/AJGEB6.0001029.

Huizinga, J., De Moel, H., & Szewczyk, W. (2017). *Global flood depth-damage functions: Methodology and the database with guidelines* (EUR 28552 EN). Publications Office of the European Union. https://doi.org/10.2760/16510.

Ibrahimkhan, A., Prasit, P., Agnihotri, G., Patel, D., & Prieto, C. (2022). Mesh grid stability and its impact on flood inundation through (2D) hydrodynamic HEC-RAS model with special use of Big Data platform: A study on Purna River of Navsari city. Arabian Journal of Geosciences, 15, 659. https://doi.org/10.1007/s12517-022-09813-w.

International Commission on Large Dams (ICOLD). (2013). *Dam surveillance: Lessons learnt from case histories*. (Bulletin No. 180).

International Commission on Large Dams (ICOLD). (2019). ICOLD incident database bulletin 99 update: Statistical analysis of dam failures. Committee on Dam Safety. Retrieved from https://www.icold-cigb.org.

International Commission on Large Dams (ICOLD) (2024) World Register of Dams database presentation. Retrieved November 25, 2024, from http://icold-cigb.org/GB-world_register/database_presentation.asp.

Kemaloğlu, N. P., Koçyiğit, M. B., & Akay, H. (2019). Investigation of 1-D numerical simulations of dam-break flood wave propagation: Case of Rahmanlar Dam. Gazi University Journal of Science, Part C: Design and Technology, 7(1), 97–111. https://doi.org/10.29109/gujsc.459444.

Kanal 362. (2024, Kasım 25). Last Minute: Ondokuz Mayıs barajı çıldırdı. Retrieved from https://www.kanal362.com.tr/son-dakika-19-mayis-baraji-cildirdi/46384/.

Karakaya, K. (2005). *Numerical simulation of the Kirazlıköprü dam failure on the Gökırmak River* (Master's thesis). Middle East Technical University, Graduate School of Natural and Applied Sciences, Ankara, Turkey.

Kocaman, B. (2019). Comparison of two different hydrodynamic models for flood propagation areas after dam failure and investigation of the sensitivity of surface roughness to flood propagation [Master's thesis]. Gazi Üniversitesi, Graduate School of Natural and Applied Sciences, Ankara, Turkey.

Kumar, A., & Sharma, R. P. (1992). Third international conference on case histories in geotechnical engineering: June 1–4, 1993, Rolla, Missouri, U.S.A. Tunnelling and Underground Space Technology, 7(4), 464. https://doi.org/10.1016/0886-7798(92)90086-W.

Li, Y., Gong, J. H., Zhu, J., Ye, L., Song, Y. Q., & Yue, Y. J. (2012). Efficient dam break flood simulation methods for developing a preliminary evacuation plan after the Wenchuan Earthquake. Natural Hazards and Earth System Sciences, 12(1), 97–106. https://doi.org/10.5194/nhess-12-97-2012.

Li, Y., Zhang, H., Yuan, Y., Lan, L., & Su, Y. (2024). Research on Failure Modes and Causes of 100-m-High Core Wall Rockfill Dams. Water (Switzerland), 16(13). https://doi.org/10.3390/w16131809.

MacDonald, T. C., & Langridge-Monopolis, J. (1984). Breaching characteristics of dam failures. Journal of Hydraulic Engineering, 110(5), 576-586. ASCE.

Marangoz, H. O., & Anilan, T. (2022). Two-dimensional modeling of flood wave propagation in residential areas after a dam break with application of diffusive and dynamic wave approaches. *Natural Hazards*, *110*(1), 429–449. https://doi.org/10.1007/s11069-021-04953-w.

Marangoz, H. O., Anılan, T., & Karasu, S. (2024). Investigating the Non-Linear Effects of Breach Parameters on a Dam Break Study. Water Resources Management, 38(5), 1773–1790. https://doi.org/10.1007/s11269-024-03765-4.

Mattas, C., Karpouzos, D., & Georgiou, P. (2023). Two-dimensional modelling for dam break analysis and flood hazard mapping: A case study of Papadia Dam, Northern Greece. Water, 15(5), 994. https://doi.org/10.3390/w15050994.

Ministry of Forestry and Water Affairs, DSI (2014). TRCOLD Embankment Dam Design Guide (Guide No: 003, Rev. 01). General Directorate of State Hydraulic Works.

Mitsopoulos, G., Panagiotatou, E., Sant, V., Baltas, E., Diakakis, M., Lekkas, E., & Stamou, A. (2022). Optimizing the Performance of Coupled 1D/2D Hydrodynamic Models for Early Warning of Flash Floods. Water, 14(15), 2356. https://doi.org/10.3390/w14152356.

Morris, M. W. (2005). *IMPACT project: Final technical report*. IMPACT. Retrieved from http://www.impact-project.net.

Morris, M. W. (2013). Breaching of earth embankments and dams (Doctoral dissertation) , The Open University.

Moussa R, Bocquillon C (2009) On the use of the diffusive wave for modeling extreme flood events with overbank flow in the floodplain. J Hydrol 374:116–135.

Mustafa, A., & Szydłowski, M. (2021). Application of different building representation techniques in HEC-RAS 2-D for urban flood modeling using the Toce River experimental case. PeerJ, 9, e11667. https://doi.org/10.7717/peerj.11667.

Najar, M., & Gül, A. (2022). Investigating the influence of dam-breach parameters on dam-break connected flood hydrograph. Teknik Dergi, 692, 12501–12524. https://doi.org/10.18400/tekderg.796334.

Ramirez, J. A., Rajasekar, U., Patel, D. P., Coulthard, T. J., & Keiler, M. (2016). Flood modeling can make a difference: Disaster risk-reduction and resilience-building in urban areas. Hydrology and Earth System Sciences Discussions. https://doi.org/10.5194/hess-2016-544.

Schubert, J. E., & Sanders, B. F. (2012). Building treatments for urban flood inundation models and implications for predictive skill and modeling efficiency. Advances in Water Resources, 41, 49–64. https://doi.org/10.1016/j.advwatres.2012.02.012.

Soedibyo, W. (1993). Teknik Bendungan. Jakarta: Pradnya Paramita.

Spor, P. (2023). Derelerde İki Boyutlu Taşkın Modellemesi ve Taşkın Tehlike Risk Haritalarının Oluşturulması. Sakarya University.

Şahin, A. N. (2016). *Performance of FLO-2D software on flood inundation analysis* (Master's thesis). Middle East Technical University, Graduate School of Natural and Applied Sciences, Ankara, Turkey.

Terzaghi, K. and Peck, R.B. (1967) Soil Mechanics in Engineering Practice. John Wiley & Sons, New York.

Turkel, A.O., Zaifoglu, H. & Yanmaz, A.M. Probabilistic modeling of dam failure scenarios: a case study of Kanlikoy Dam in Cyprus. Nat Hazards 120, 10087–10117 (2024). https://doi.org/10.1007/s11069-024-06599-w.

Ünal, Ç. I. (2019). Two-dimensional dam break analyses of Berdan Dam (Master's thesis). Middle East Technical University, Graduate School of Natural and Applied Sciences, Ankara, Turkey.

U.S. Army Corps of Engineers. (1986). EM 1110-2-1901: Engineering and design: Seepage analysis and control for dams. Washington, DC: Department of the Army. Retrieved from. https://www.publications.usace.army.mil/Portals/76/Publications/EngineerManuals/EM_1110-2-1901.pdf.

U.S. Army Corps of Engineers. (2014). Using HEC-RAS for dam break studies. Hydrologic Engineering Center. Davis, CA: U.S. Army Corps of Engineers. Retrieved from https://www.hec.usace.army.mil/software/hec-ras/.

Von Thun, J. L., & Gillette, D. R. (1990). Guidance on breach parameters. [Internal Memorandum]. Denver, CO: U.S. Department of the Interior, Bureau of Reclamation.

Yeğin, M. (2015). Flood risk mapping using economic, environmental, and social dimensions (Master's thesis). Middle East Technical University, Graduate School of Natural and Applied Sciences, Ankara, Turkey.

Yılmaz, K., Darama, Y., Oruc, Y., & Melek, A. B. (2023). Assessment of flood hazards due to overtopping and piping in Dalaman Akköprü Dam, employing both shallow water flow and diffusive wave equations. Natural Hazards, 117(3), 979–1003. https://doi.org/10.1007/s11069-023-05891-5.

Yılmaz, K., Usul, N., & Akyürek, Z. (2004). Modeling the propagation of DEM uncertainty on flood inundation depths. Journal of Hydrology, 293(1-4), 1–9. https://doi.org/10.1016/j.jhydrol.2004.01.011.

Wahl, T. L. (1998). Prediction of embankment dam breach parameters: Literature review and needs assessment (DSO-98-004). Bureau of Reclamation, Dam Safety Office, U.S. Department of the Interior.

Wahl, T. L. (2004). Uncertainty of predictions of embankment dam breach parameters. Journal of Hydraulic Engineering, 130(5), 389–397. https://doi.org/10.1061/(ASCE)0733-9429(2004)130:5(389).

Zagonjolli, M. (2007). Dam break modeling, risk assessment, and uncertainty analysis for flood mitigation (Doctoral dissertation). Delft University of Technology & UNESCO-IHE Institute for Water Education, Delft, Netherlands.

Zhang, L., Peng, M., Chang, D., & Xu, Y. (2016). Dam failure mechanisms and risk assessment. Singapore: John Wiley & Sons. https://doi.org/10.1002/9781118558546.

APPENDICES

A. Model Grid Sizes Inundation Maps

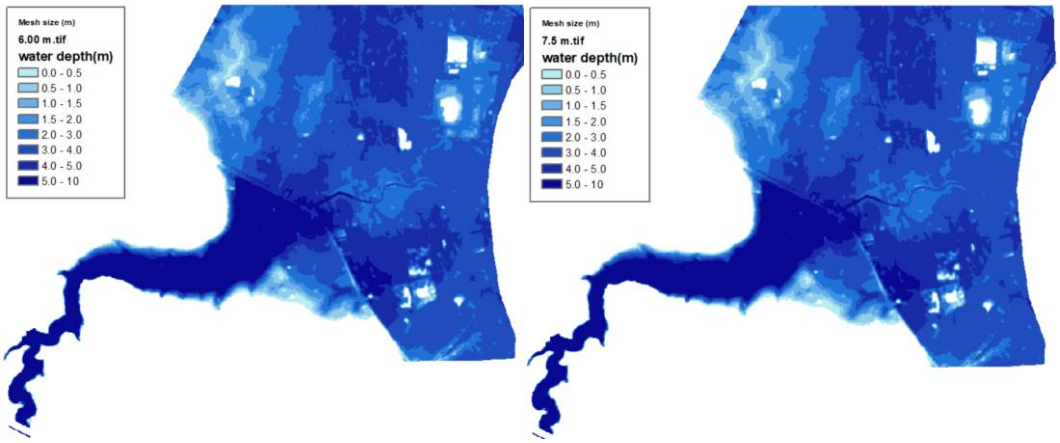

Figure A-1 Maximum water depth (a) 6.00 m grid size (b) 7.50 m grid size (Adjusted Scale/Enhanced Visibility)

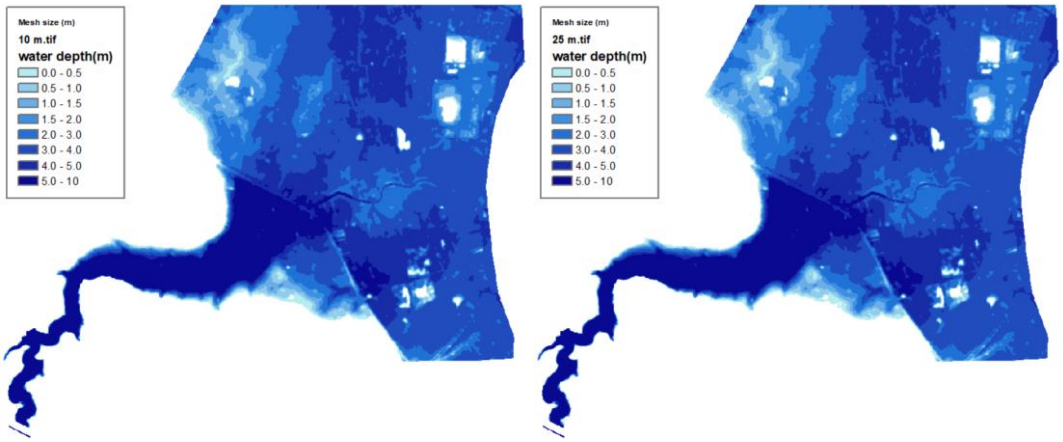

Figure A-2 Maximum water depth (a) 10.0 m grid size (b) 25.0 m grid size (Adjusted Scale/Enhanced Visibility)

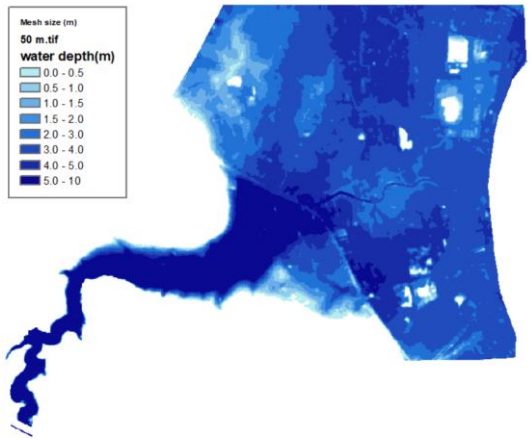

Figure A-3 Maximum water depth (a) 50.0 m grid size (Adjusted Scale/Enhanced Visibility)

B. Inundation Maps of the Worst-Case Scenario

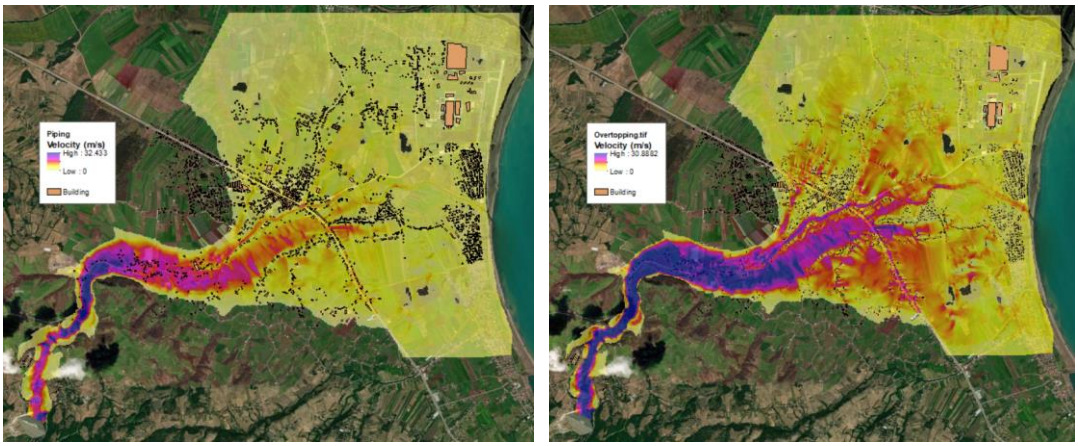

Figure B-1 Maximum velocity (a) piping scenario (b) overtopping scenario

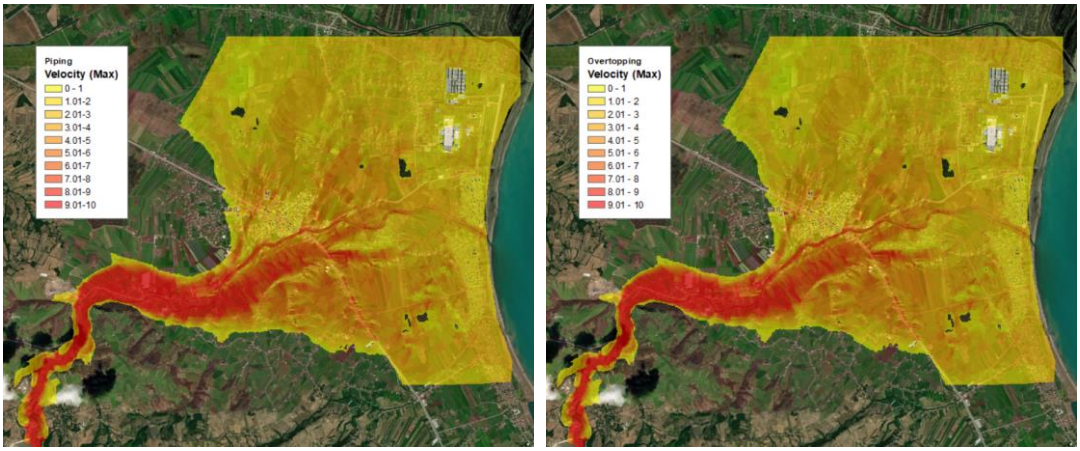

Figure B-2 Maximum velocity (a) piping scenario (b) overtopping scenario (adjusted scale/enhanced visibility)

C. Inundation Maps for Different Breach Parameter Prediction Equations

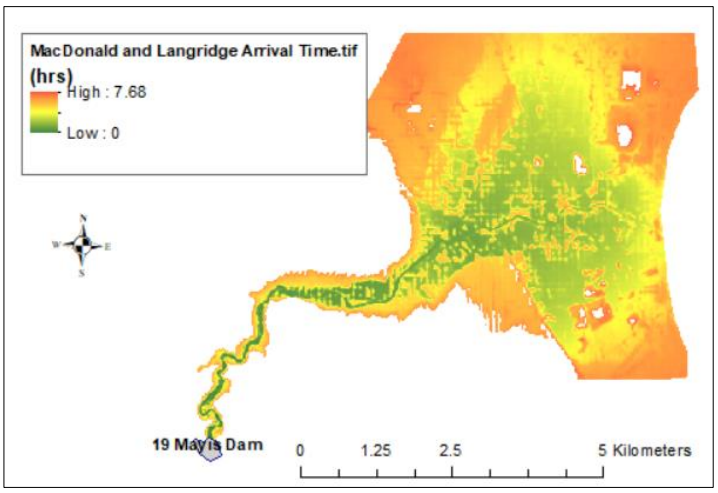

Figure C-1 Maximum arrival time (hrs) based on MacDonald & Langridge-Monopolis equation

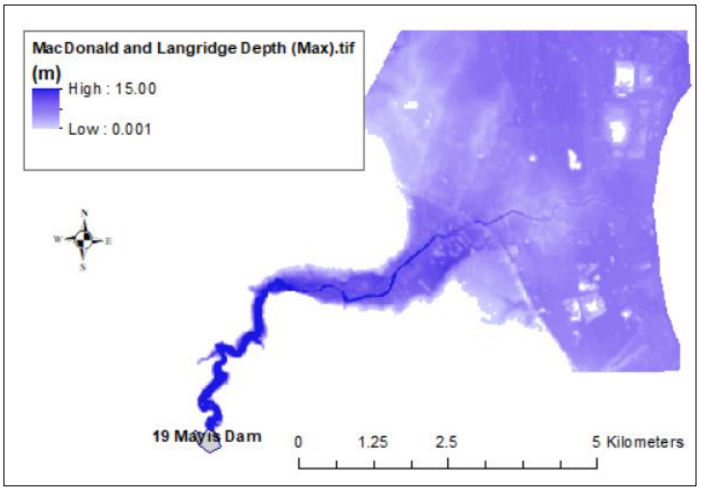

Figure C-2 Maximum water depth (m) based on MacDonald & Langridge-Monopolis equation

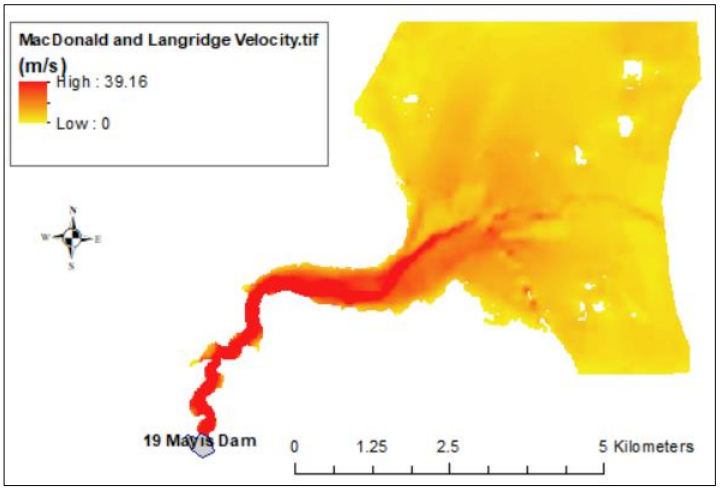

Figure C-3 Maximum velocity (m/s) based on MacDonald & Langridge-Monopolis equation

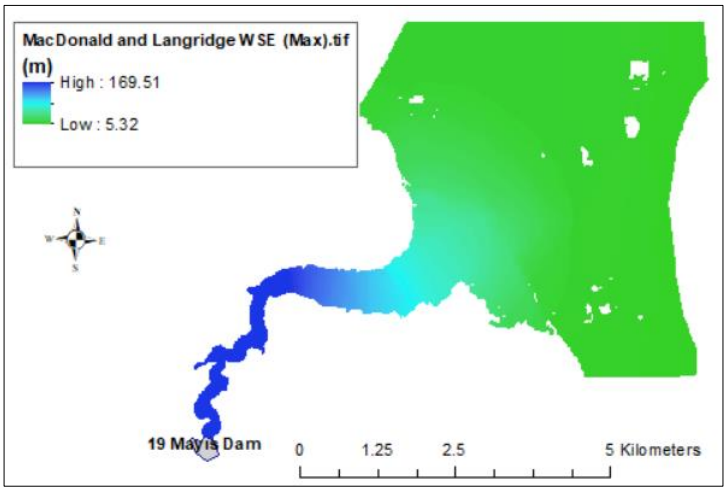

Figure C-4 Maximum water surface wlevation (m) based on MacDonald & Langridge-Monopolis equation

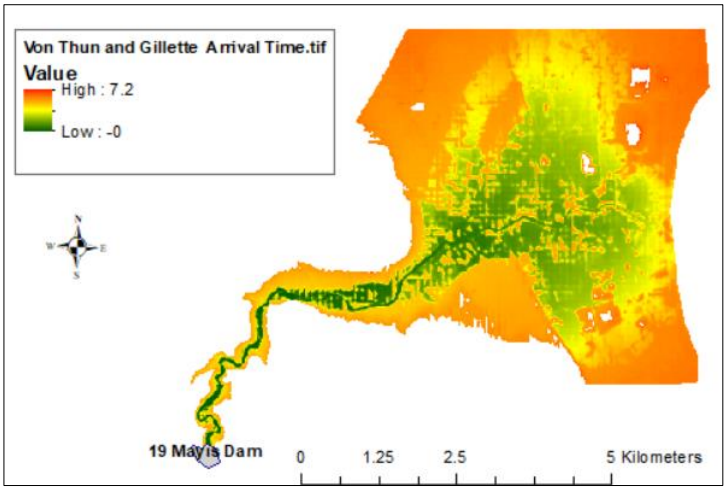

Figure C-5 Maximum arrival time (hrs) based on Von Thun and Gillette (1990) equation

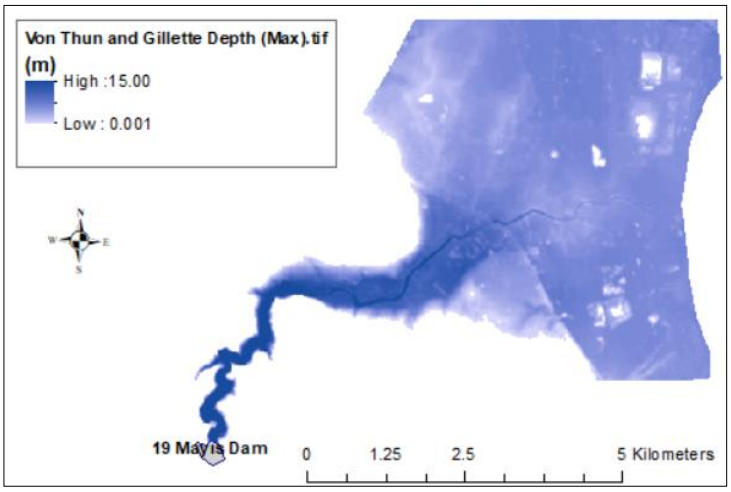

Figure C-6 Maximum water depth (m) based on Von Thun and Gillette (1990) equation

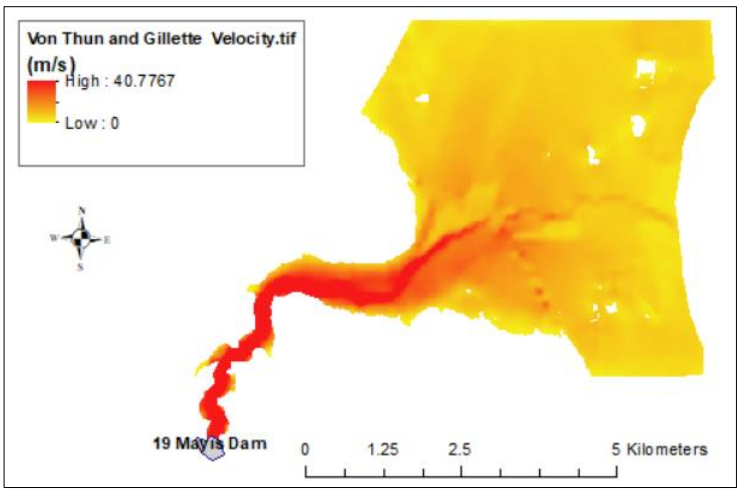

Figure C-7 Maximum velocity (m/s) based on Von Thun and Gillette (1990) equation

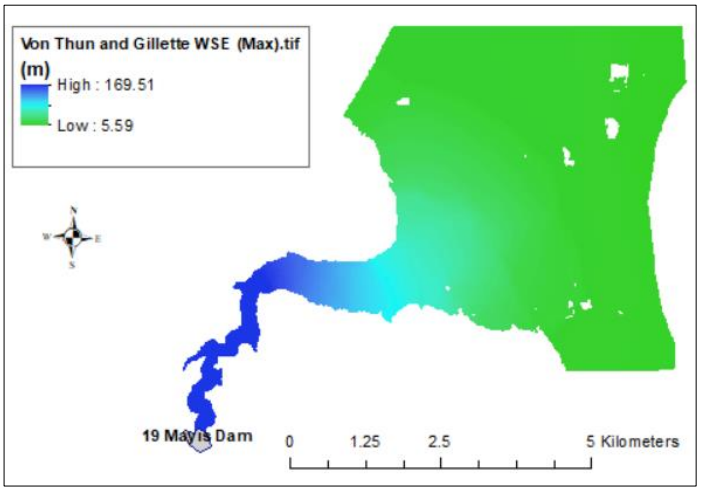

Figure C-8 Maximum water surface elevation (m) based on Von Thun and Gillette (1990) equation

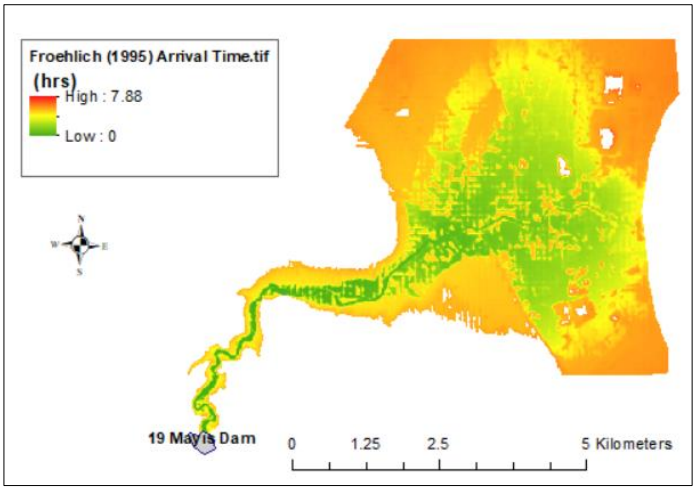

Figure C-9 Maximum arrival time (hrs) based on Froehlich (1995) equation

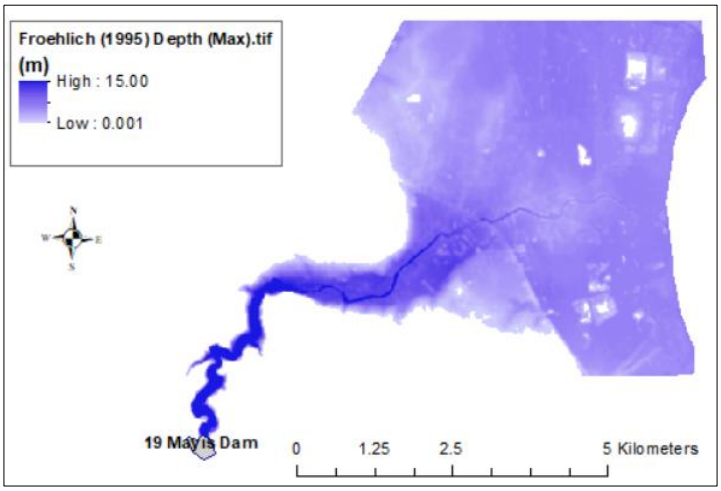

Figure C-10 Maximum water depth (m) based on Froehlich (1995) equation

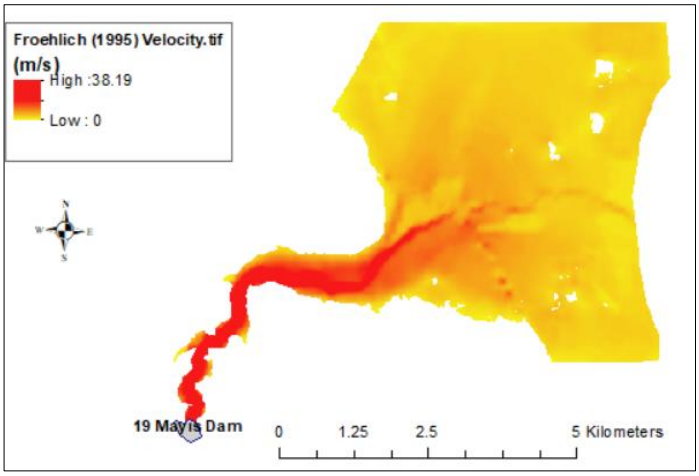

Figure C-11 Maximum velocity (m/s) based on Froehlich (1995) equation

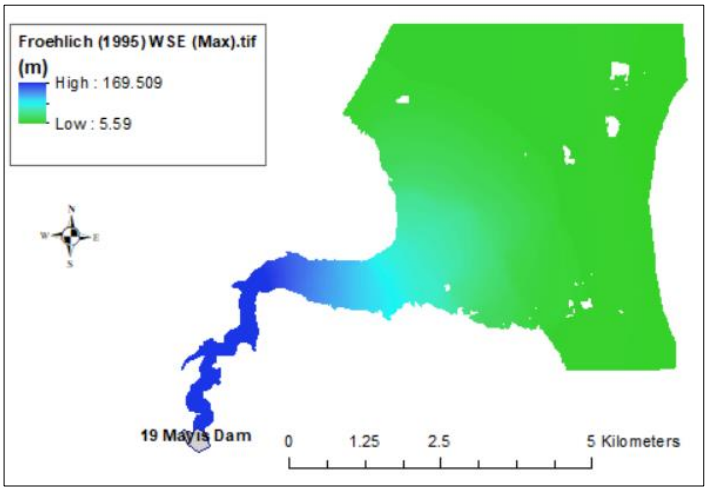

Figure C-12 Maximum water surface elevation (m) based on Froehlich (1995) equation

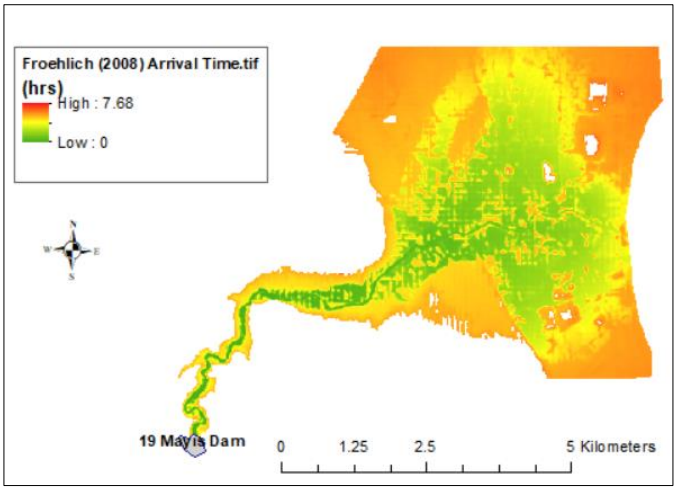

Figure C-13 Maximum arrival time (hrs) based on Froehlich (2008) equation

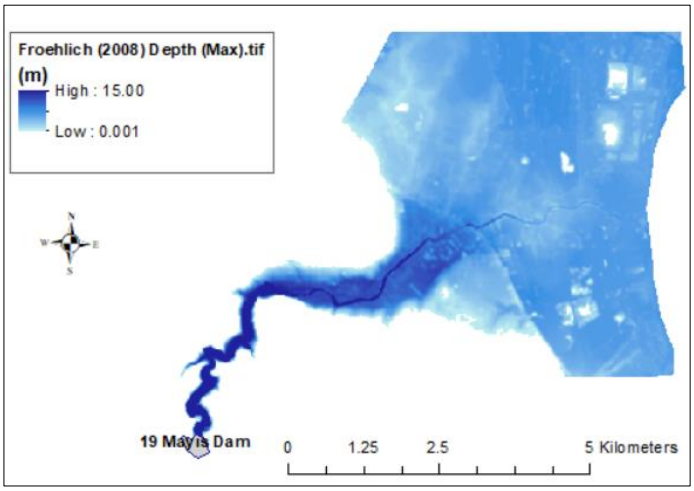

Figure C-14 Maximum water depth (m) based on Froehlich (2008) equation

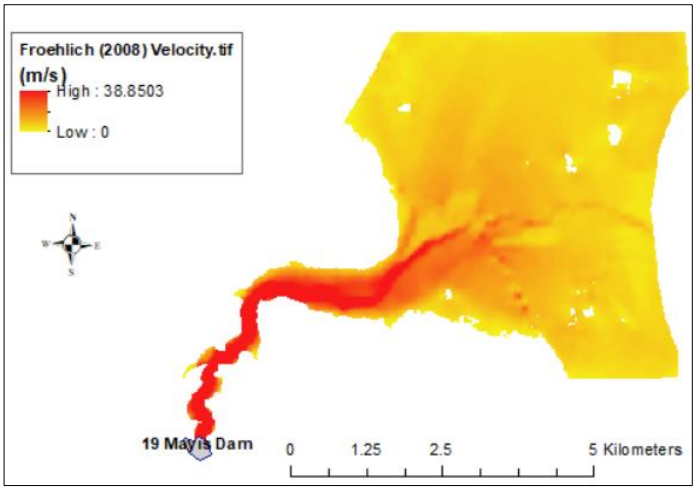

Figure C-15 Maximum velocity (m/s) based on Froehlich's (2008) Equation

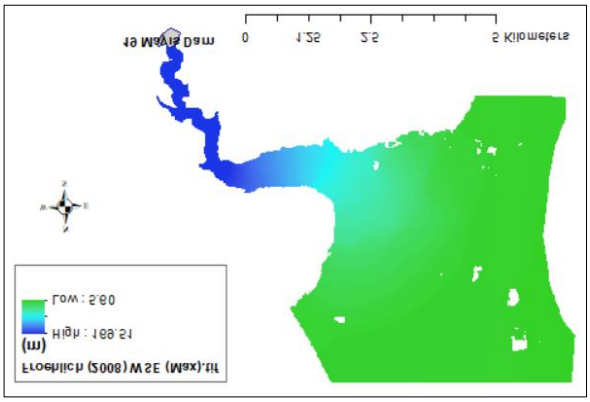

Figure C-16 Maximum water surface elevation (m) based on Froehlich (2008) equation

D. Inundation Maps for Different Governing Equations

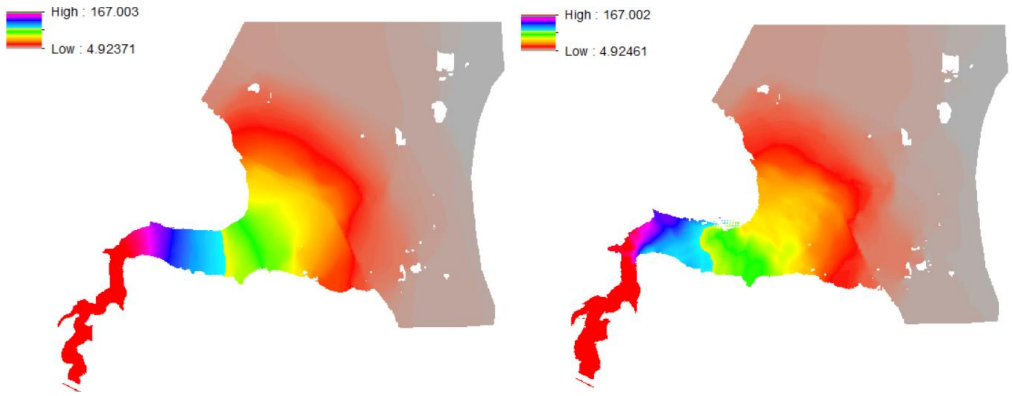

Figure D-1 Water surface elevation (m) (a) diffusion wave method (b) shallow water equation method

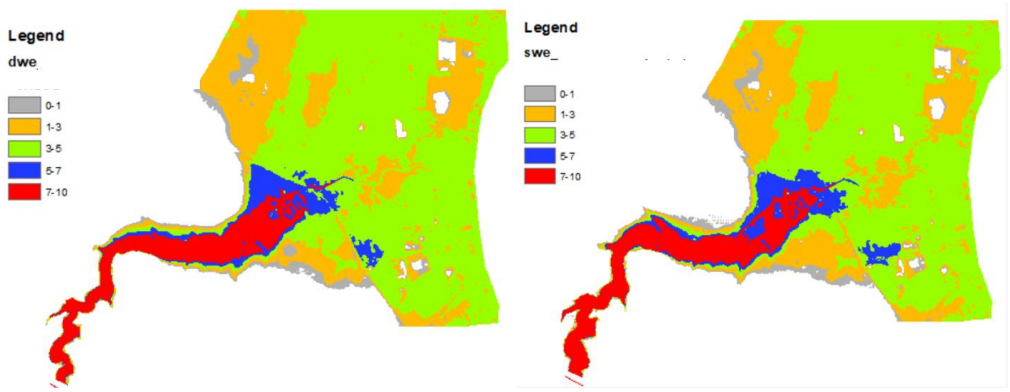

Figure D-2 Max. water depth (m) (a) diffusion wave method (b) shallow water equation method

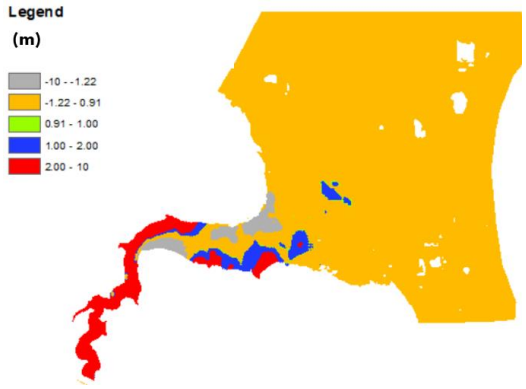

Figure D-3 Maximum depth difference (shallow water method - diffusion wave method)

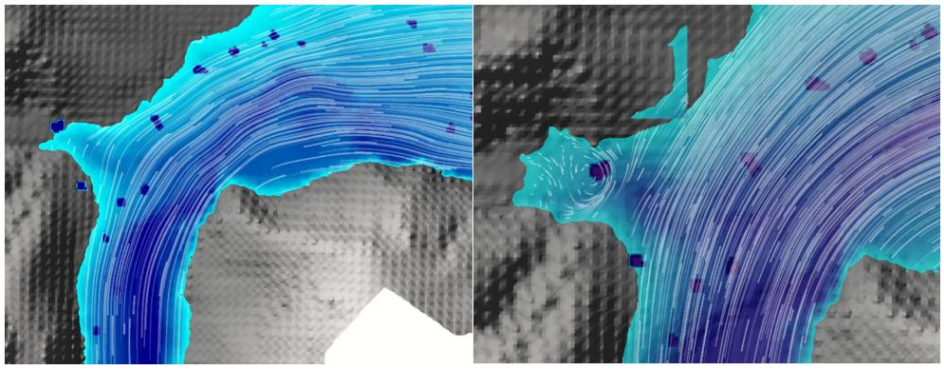

Figure D-4 Particle tracing in a zoomed-in view using the (a) diffusion wave method, (b) shallow water method

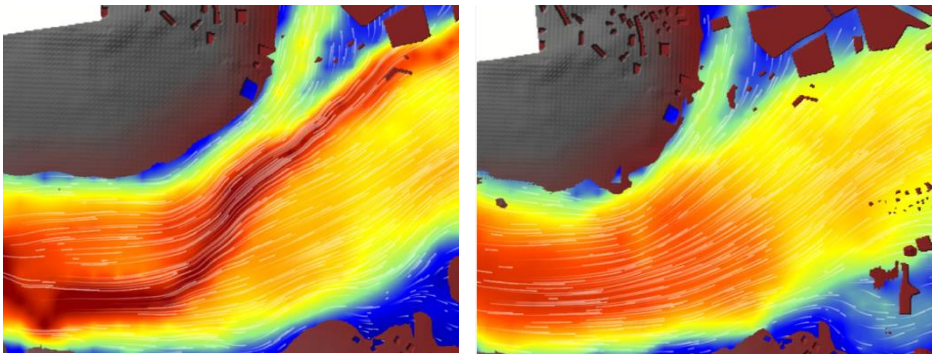

Figure D-5 Zoomed-in velocity distribution using the (a) diffusion wave method, (b) shallow water method

E. Different Governing Equations Inundation Maps

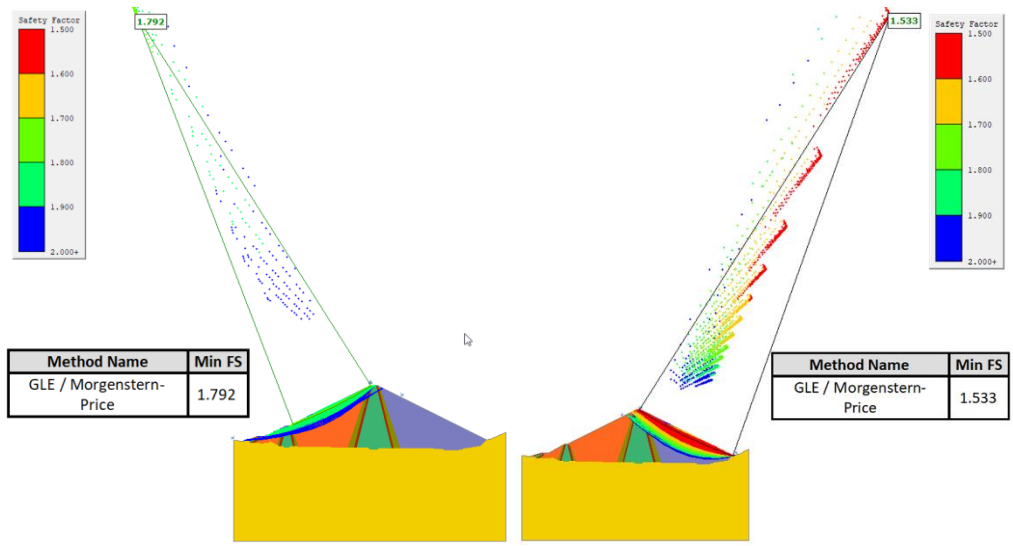

Figure E-1 Slope stability analysis results (a) end of construction case upstream side (b) end of construction case downstream side

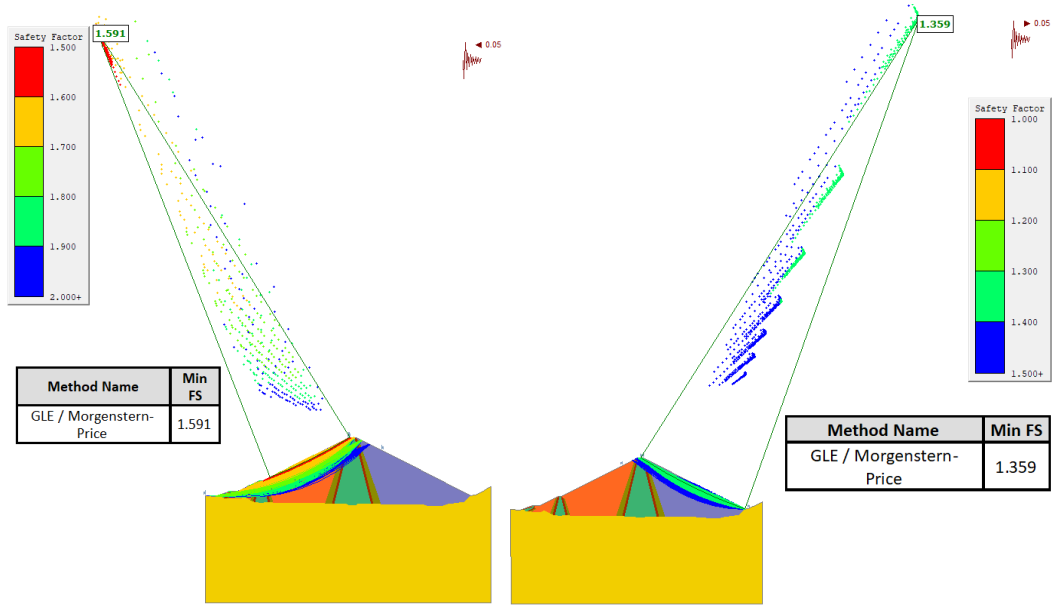

Figure E-2 Slope stability analysis results (a) end of construction+OBE case upstream side (b) end of construction +OBE case downstream side

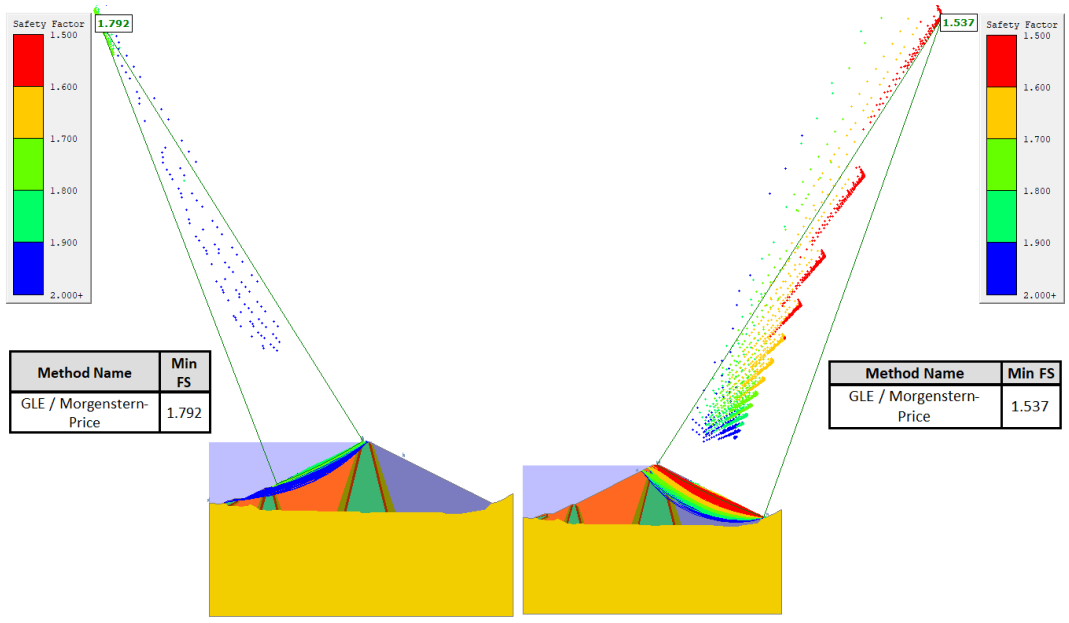

Figure E-3 Slope stability analysis results (a) operation case upstream side (b) operation case downstream side

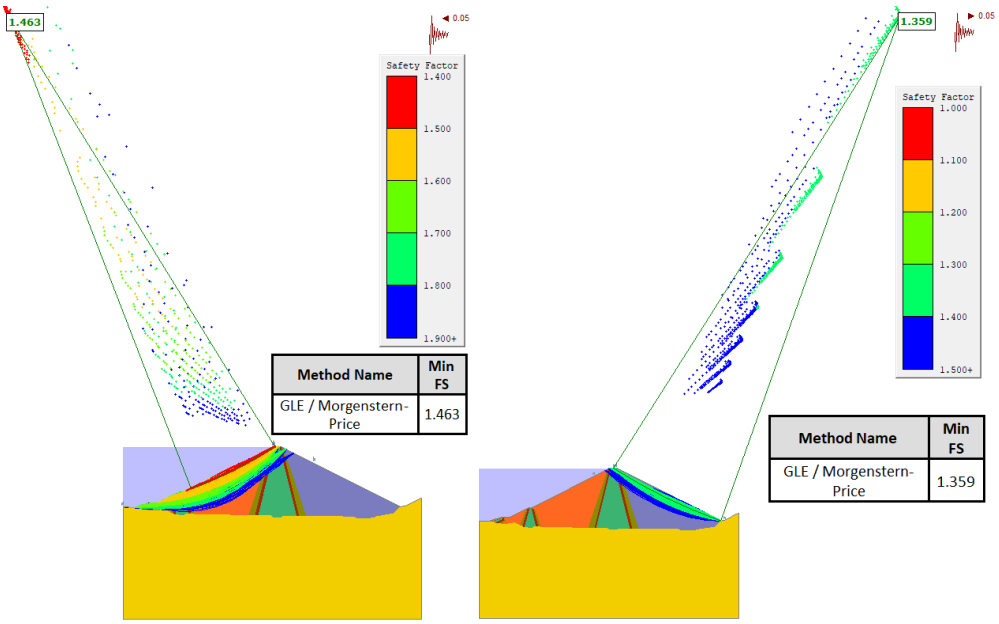

Figure E-4 Slope stability analysis results (a) operation+OBE case upstream side (b) operation+OBE case downstream side

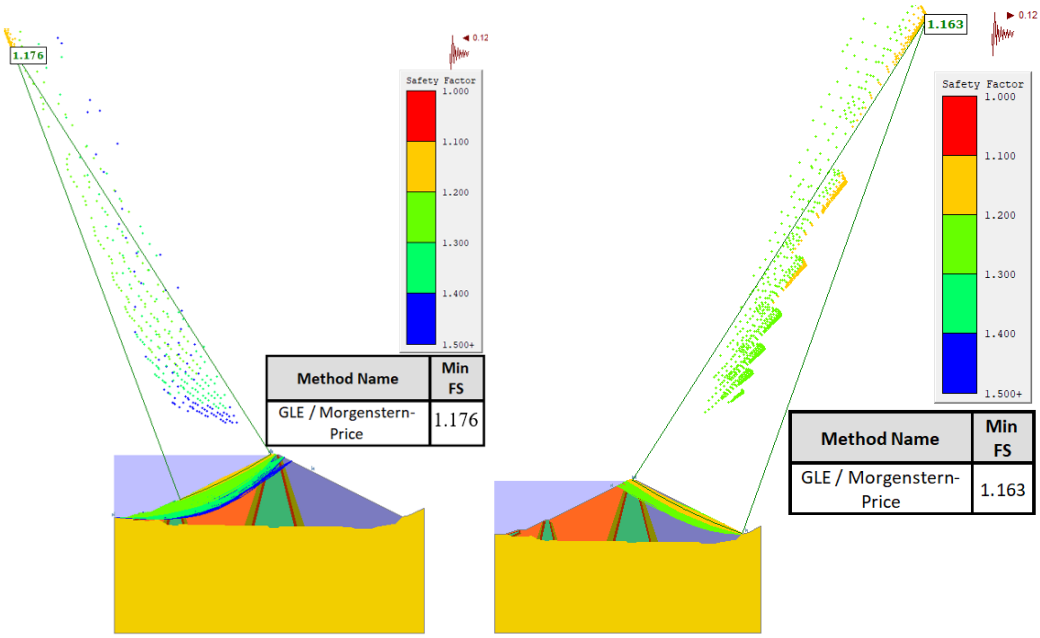

Figure E-5 Slope stability analysis results (a) operation+MCE case upstream side (b) operation+MCE case downstream side

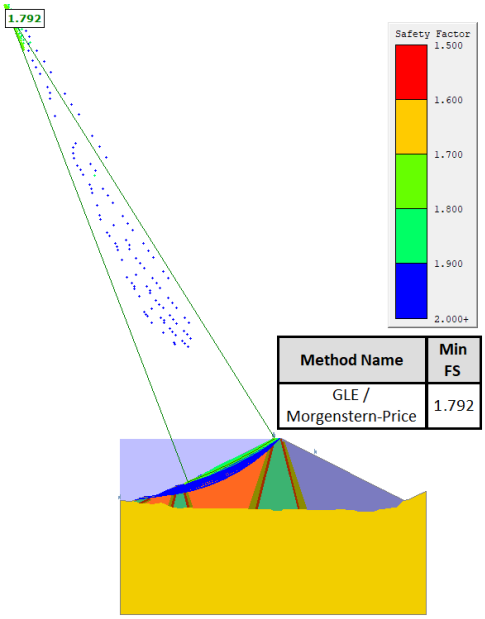

Figure E-6 Slope stability analysis results in a sudden drawdown in the upstream side.